

CORRELATING COMPUTER MODELED CONTACT STRESS TO  
SURFACE WEAR OF MULTI-COMPONENT IMPLANT  
AN ABSTRACT

SUBMITTED ON THE FOURTH DAY OF MAY 2022  
TO THE DEPARTMENT OF BIOMEDICAL ENGINEERING  
OF THE SCHOOL OF SCIENCE AND ENGINEERING  
OF TULANE UNIVERSITY  
IN PARTIAL FULFILLMENT OF THE REQUIREMENTS

FOR THE DEGREE OF  
MASTER OF SCIENCE

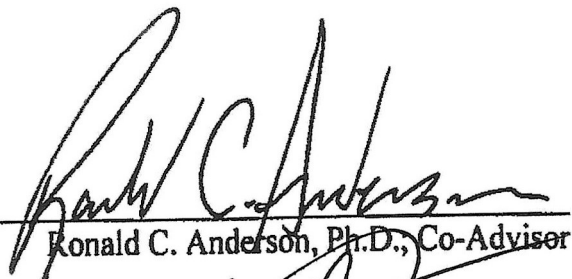
BY:



---

MADELINE G. TALLMAN

APPROVED:



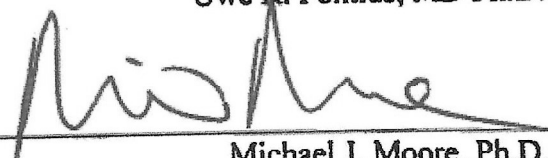
---

Ronald C. Anderson, Ph.D., Co-Advisor



---

Uwe R. Pontius, MD Ph.D.



---

Michael J. Moore, Ph.D.

## **ABSTRACT**

Osteoarthritis (OA) is the most common joint disorder in the United States. High tibial osteotomies (HTOs) can extend the life of the knee joint in young patients with OA before requiring total knee arthroplasty (TKA) by readjusting the weight bearing axis off the region with the most cartilage loss. HTO technology currently is not indicated for morbidly obese patients because the single plate design must support the patient's weight across a gap in the tibia.

A multicomponent wedge designed to fit into the osteotomy site could support the corrected knee geometry from the HTO as well as minimizing the incision size needed for the procedure. This would be ideal for patients who are morbidly obese by decreasing the risk of complications like osteotomy site collapse and infection. Existence of metallic interfaces in the multicomponent implant warrants studies on wear and corrosion occurring at the component interfaces to prevent metal particles leeching into the surrounding tissue.

This thesis study developed a testing procedure to subject this novel implant design to cyclic loading and evaluate corresponding wear. Wear was demonstrated by loss of mass in each component and increased mass in water collected under interfaces was measured. Wear scars on surfaces where the high stress regions in the computational model were observed. A computational model was also created to inform an understanding of the high stress regions, especially at component interfaces under the loading conditions of the test. The results from this study preliminarily demonstrated that high stress regions on interfacing surfaces of the implant in the computational model is correlated with physical wear of a stainless-steel implant prototype.

CORRELATING COMPUTER MODELED CONTACT STRESS TO

SURFACE WEAR OF MULTI-COMPONENT IMPLANT

A THESIS

SUBMITTED ON THE FOURTH DAY OF MAY 2022

TO THE DEPARTMENT OF BIOMEDICAL ENGINEERING

OF THE SCHOOL OF SCIENCE AND ENGINEERING

OF TULANE UNIVERSITY

IN PARTIAL FULFILLMENT OF THE REQUIREMENTS

FOR THE DEGREE OF

MASTER OF SCIENCE

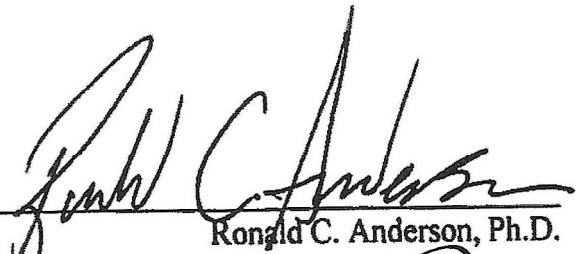
BY:



---

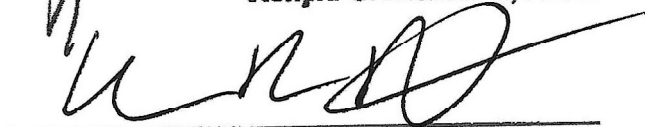
MADELINE G. TALLMAN

APPROVED:



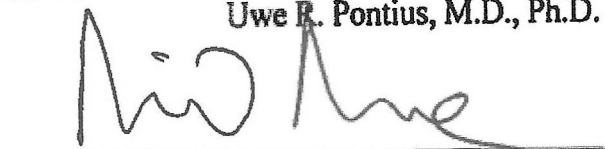
---

Ronald C. Anderson, Ph.D.



---

Uwe R. Pontius, M.D., Ph.D.



---

Michael J. Moore, Ph.D.





## ACKNOWLEDGEMENTS

I thank Dr. Ronald Anderson and his advisership to me over the last two years. Working on projects with his support transformed my engineering education from theoretical to tangible and experiential.

I thank Dr. Uwe Pontius for the opportunity to study the intersection of engineering and clinical medicine.

I thank Dr. Michael Moore, Chair of Biomedical Engineering at Tulane University, for saying “yes” to one more thing and being a valued member of my thesis committee.

I thank the Tulane University Department of Biomedical Engineering, specifically John Sullivan and Rebecca Derbes. Their dedication to the department and students is unparalleled and allowed me to succeed in my acquiring necessary materials for my thesis and all my projects at Tulane BME.

I thank the Coordinated Instrument Facility (CIF) at Tulane University, and specifically the aid of Dr. Jibao He who collected electron microscope images for this thesis.

I thank the Tulane Makerspace for the ability to prototype and fabricate the fixtures necessary for this project.

I thank my parents, Meg and Brian Tallman, for their enthusiasm for my education and engineering projects.

## TABLE OF CONTENTS

<b>ACKNOWLEDGEMENTS</b> .....	iii
<b>LIST OF TABLES</b> .....	vi
<b>LIST OF FIGURES</b> .....	vii
<b>CHAPTER 1: INTRODUCTION</b> .....	1
<b>CHAPTER 2: BACKGROUND</b> .....	5
<b>2.1 Anatomy</b> .....	5
<b>2.2 Purpose of High Tibial Osteotomy (HTO)</b> .....	8
<b>2.3 A Multi-Component Implant for Use in Tibial Osteotomy to Correct Varus Deformity in the Morbidly Obese</b> .....	11
<b>2.4 Fretting Corrosion, Tribology, and Inflammation</b> .....	13
<b>2.5 Wear in Orthopedic Implants</b> .....	18
<b>2.6 Mapping Fretting to Relate Wear to Contact Forces and Interfaces</b> .....	20
<b>2.7 Hypothesis</b> .....	21
<b>CHAPTER 3: MATERIALS &amp; METHODS</b> .....	22
<b>3.1 Implant Prototype Fabrication</b> .....	22
<b>3.2 Wear Assessment of Implant in Simulator Device</b> .....	22
<b>CHAPTER 4: RESULTS</b> .....	29
<b>4.1 Implant Interface Mapping Scheme</b> .....	29
<b>4.2 Component Weight Loss</b> .....	30
<b>4.3 Optical Wear Patterns</b> .....	30
<b>4.4 General Computational Results with Von Mises Stress</b> .....	33
<b>4.5 Wear Particles Collected Under Interfaces</b> .....	38
<b>4.6 Comparing Contact Pressure from Computational Model with Optical Wear Scar Patterns</b> .....	39
<b>CHAPTER 5: DISCUSSION &amp; CONCLUSION</b> .....	44
<b>5.1 Component Weight Loss</b> .....	44
<b>5.2 Optical Wear Patterns</b> .....	45
<b>5.3 General Computational Results with Von Mises Stress</b> .....	47
<b>5.4 Wear Particles Collected Under Interfaces</b> .....	48

<b>5.5 Comparing Contact Pressure from Computational Model with Optical Wear Scar Patterns.....</b>	<b>50</b>
<b>5.5 Critique of Methods .....</b>	<b>51</b>
<b>5.6 Conclusion.....</b>	<b>53</b>
<b>APPENDIX A: STANDARD GUIDE FOR GRAVIMETRIC WEAR ASSESSMENT OF PROSTHETIC HIP DESIGNS IN SIMULATOR DEVICES...54</b>	
<b>APPENDIX B: A MULTI-COMPONENT IMPLANT FOR USE IN TIBIAL OSTEOTOMY TO CORRECT VARUS DEFORMITY IN THE MORBIDLY OBESE .....</b>	<b>66</b>
<b>APPENDIX C: PHOTOS OF PLA IMPLANT SURFACES DURING FIXTURE DESIGN .....</b>	<b>71</b>
<b>APPENDIX D: PHOTOS OF STAINLESS-STEEL IMPLANT SURFACES .....</b>	<b>78</b>
<b>APPENDIX E: SEM IMAGES OF STAINLESS-STEEL IMPLANT SURFACES .....</b>	<b>96</b>
<b>APPENDIX F: RAW DATA FROM IMPLANT COMPONENT WEIGHTS AND WELL SAMPLE WEIGHTS IN GRAMS .....</b>	<b>102</b>
<b>APPENDIX G: COMPUTATIONAL MODEL CONVERGENCE TEST FOR MESH SIZE OF IMPLANT .....</b>	<b>104</b>
<b>APPENDIX H: LINK TO ABAQUS MODEL.....</b>	<b>105</b>
<b>LIST OF REFERENCES .....</b>	<b>106</b>

**LIST OF TABLES**

Table 1 Stainless steel implant component weights before and after 50,000 cycles of cyclic loading .....30

## LIST OF FIGURES

Figure 1 Graphic displaying the method for finding the mechanical and anatomical axis of the leg from radiographs (Liu 2019).....	8
Figure 2. Depiction of novel multicomponent implant (Spillane 2021).....	12
Figure 3 Mises stress distributions at mid-frontal plane (Spillane 2021).....	13
Figure 4 Endolab fixture for measuring wear according to ASTM F3047M - 15 .....	16
Figure 5 Graph of volumetric wear vs number of test cycles from ASTM F3047M-15 ...	17
Figure 6 Test fixture set up in ADMET axial torsion testing machine.....	24
Figure 7 Superior surface of bottom fixture with labeled wells .....	24
Figure 8 Map of implant and the surfaces of interest at stainless steel to stainless steel interfaces .....	29
Figure 9 Exploded view of implant .....	30
Figure 10 Digital microscope images from surface S (a) pre-test (b) after 10,000 loading cycles and (c) after 50,000 loading cycles .....	31
Figure 11 SEM images of surfaces E, F, and G (a) pre-test and (b) post 50,000 cycles ...	32
Figure 12 Color map of von Mises stress in MPa.....	33
Figure 13 Von Mises stress of all components.. .....	34
Figure 14 Von Mises stress of exterior of the medial component in two different views.	34
Figure 15 Von Mises stress of exterior of lateral component in two different views.....	35
Figure 16 Von Mises stress of exterior of anterior component in three different views. ...	36
Figure 17 Von Mises stress of exterior of posterior component in three different views .	37
Figure 18 Relative sample weights after 10,000 loading cycles on a stainless-steel implant .....	38
Figure 19 Relative sample weights after 50,000 loading cycles on a stainless-steel implant .....	39
Figure 20 Color map of contact stress in MPa.....	39
Figure 21 Contact stress of the exterior of the medial component in two different views and images of corresponding surfaces after 50,000 cycles.....	40
Figure 22 Contact stress of the exterior of the lateral component in two different views and images of corresponding surfaces after 50,000 cycles.....	41
Figure 23 Contact stress of the exterior of the anterior component in three different views and images of corresponding surfaces.....	42
Figure 24 Contact stress of the exterior of the posterior component in three different views and images of corresponding surfaces after 50,000 cycles. ....	43

## CHAPTER 1: INTRODUCTION

Osteoarthritis (OA) is a debilitating joint disease where cartilage and subchondral bones at joints degrade. OA affects a growing number of people and is most commonly associated with the knee (Spitaels 2020). Common symptoms of OA in the knee are described as aching and stiffness in the joint especially during weightbearing activities such as walking (Michael 2010). The loss of cartilage from OA can be evaluated radiologically, especially by the metric of joint space. Radiographic detection of OA in the knee increases with age: 19.2% - 27.8% of people over 45 and 37% of people over 65 (Lawrence 2008, Zhang 2010).

Treatment rigor ranges widely from nonsteroidal anti-inflammatory drugs (NSAIDs) and physical therapy to surgical interventions like total knee arthroplasty (TKA) and unicompartmental knee arthroplasty (UKA). Nearly 700,000 TKAs were performed in 2009 in the U.S. and that number is estimated to increase by over 400% to 2.8 million per year by 2040 (Wier 2009, Singh 2019). Primary TKAs have survivorship of 90-95% for the first 15 years. The survivorship of the implant corresponding to a revision rate of 4.8% after 10 years (Resnic 2012, Pabinger 2013). Revision TKAs have a shorter lifespan of 71-86% survivorship at 10 years (Resnic 2012, Pabinger 2013). This shows that TKA is not an ideal long-term solution for patients expected to use the joint for more than 25 years.

Obesity drastically increases the risk of developing osteoarthritis in hand, hip, and knee joints (King 2013). Physicians, especially orthopedic surgeons, face a unique

challenge when treating patients with obesity and osteoarthritis. These patients seek pain reduction and increased mobility, as any patient with OA. Patients with obesity and OA are more likely to require surgery and are on average undergoing TKAs at a younger age than non-obese TKA patients (Wendelboe 2003, Bliddal 2014, Boyce 2019). Outcomes, however, are noted to be negatively influenced by weight. Surgeons do not want to place these patients under additional risks of complications. A BMI of 40 was observed to be a threshold for infection and revision because rates of complication were drastically higher after rising above that BMI (OrthoCarolina Hip and Knee Center 2013, Roche 2019). A 22% complication rate from TKA procedures in morbidly obese patients is alarmingly high (McElroy 2013, Roche 2019). Complication types include superficial wound infection, prosthetic joint infection, wound healing problems or delay, aseptic/radiographic loosening, osteolysis, and wear (Boyce 2019). Another study found there was no significant relationship between increasing BMI and risk of revision based on a study that observed TKA outcomes for a year after surgery (Deshmukh 2002, Bliddal 2014). While that is a positive outcome, one year is not a long enough time to conclude that high BMI does not impact the long-term success of TKA. The mean revision rates of TKAs are 7% in the morbidly obese population and 2% in non-obese patients (Boyce 2019). Not only is the “life” of the implant at stake, but the life of the patient as well.

Additionally, the number of diseases patients with OA have has increased (Spitaels 2020). These comorbidities include diabetes, cardiovascular events, and obesity (Reeuwijk 2010). Standard surgical treatments such as TKA are riskier in these patients where comorbidities could increase rate and severity of complications. Greater costs are

tied directly to the higher incidence of superficial infections and reoperation in obese patients (Roche 2019, McElroy 2013, Ward 2015). Every five unit increase in BMI > 30kg/m<sup>2</sup> had an increase in \$250-\$300 for primary TKA and \$600-\$650 in revision TKA from increased operating room time and length of hospital stay (Roche 2019, Bradley 2014, Epstein 1987, OrthoCarolina Hip and Knee Center 2013, Kremers 2014).

Obese patients are often advised against surgical treatments of OA. Weight loss is commonly suggested to help obese patients naturally relieve the load on their knees. This would not help reverse any existing disease but would mitigate the progression of worsening symptoms. Weight loss is difficult to achieve and sustain, especially under painful conditions from OA (Bliddal 2014). Physicians and patients postulate that activity levels will increase after the surgical intervention, helping the patient maintain lost weight. A third of patients regained 5% of their baseline body weight after weight loss and OA surgical intervention (Riddle 2013). This demonstrates that although potentially beneficial, weight loss cannot be counted on as a reliable long-term treatment.

High tibial osteotomies (HTOs) are both the past and the future for treatment of OA. This surgical treatment realigns the angle of the knee joint, redistributing force more evenly across the tibial plateau correcting varus deformity associated with concentrated force in the medial compartment. This will help increase joint space and prevent the total degradation of cartilage and subchondral bone. It fell out of favor with surgeons as TKA and UKA technology significantly improved.

Current techniques for HTOs involve utilizing locking screws to secure a plate to the medial aspect of the tibia to hold open a wedge cut by the surgeon. In combination with bone graft, new bone fills the osteotomy site and weight bearing can resume with a



corrected joint angle. In situations where patients have high BMIs, the plate may not be strong enough to hold the osteotomy site open to maintain the new joint geometry before new bone is strong enough for weight bearing

A novel multicomponent wedge design will support the osteotomy site internally allowing for early weight bearing following the HTO procedure, even for patients with high BMI. The titanium alloy implant will fill the wedge-shaped space of the osteotomy site from a small incision. Each of the four pieces of the implant will fit together, jigsaw-like, to ensure the joint correction angle is maintained.

Contact between the interfaces of the implant components requires studies to understand the mechanism and rates of wear. Wear particles are not native to the body, triggering an inflammatory response from the immune system. The nature of the response is dependent on a variety of material and geometric properties of the debris at the interface of native tissue. “Particles ranging in size between 0.1  $\mu\text{m}$  and 10  $\mu\text{m}$  are considered the most biologically reactive. Particles with smaller sizes, particularly those with a mean size of  $<1 \mu\text{m}$ , are likely to induce a stronger inflammatory response than larger ones” (Zhang 2020, Vermes 2000). The immune response harshly impacts the native tissue, potentially causing noticeable bone resorption from osteoclasts. Rather than bony ingrowth stabilizing the implant, patients could face and implant non-union (Zhang 2020).

Interfaces of multicomponent implants is a crucial area for orthopedic implant developers to be aware of and study. One of the largest biomedical implants recalls of the current century came from metal poisoning from wear debris from metal-on-metal hip

implants. Designers must address the potential risks to patients, surgeons, and insurance companies to mitigate the harm an implant has on its recipient.

This thesis aims to map potential high contact stress regions using ABAQUS finite element modeling software and compare them to physical evidence of surface wear and wear particles from a prototype implant.

## CHAPTER 2: BACKGROUND

### 2.1 Anatomy

The knee is a diarthrodial joint comprised of three bones: the femur, tibia, and patella. The tibiofemoral joint transfers bodyweight to the tibial plateau (Flandry 2011). The distal end of the femur has two rounded convex condyles that articulate with the concave surfaces of the tibial plateau: one medial and one lateral. The medial compartment is more elongated and ovular than the lateral. Close to 60% of body weight is projected through the medial compartments of the knees and the remaining 40% is projected through the lateral compartment. There are several soft tissue structures that stabilize and move this joint including the quadriceps, hamstrings, iliotibial tract, gastrocnemius, posterior cruciate ligament, anterior cruciate ligament, medial collateral ligament, lateral collateral ligament, capsular ligaments, and meniscus. The combination of these muscular, fibrous, and bony tissues allows for many movement types of the knee: flexion, extension, medial rotation, and lateral rotation.

The loading of the knee is unique for each movement and activity. While standing, the knees are subjected to 107% body weight (BW). Many activities induce higher loading on the knees, such as “stair descending (346% BW), followed by stair ascending (316% BW), level walking (261% BW), one legged stance (259% BW), knee bending (253% BW), standing up (246% BW), sitting down (225% BW)” (Wright 2005). A high BW increases the likelihood of failure of the knee since loading is dependent of BW as described above.

Articular cartilage is key to the success of the knee joint. It covers the surface of the bone of the tibial plateau and femoral condyles. The smooth, low friction surface of the cartilage allows painless translation of the tibia with respect to the femur (Fox 2009). As articular cartilage degrades, the coefficient of friction in the joint increases. Friction resists movement between two surfaces relative to each other. Articular cartilage is anisotropic and supports a compressive load. It also has viscous properties under shear. The cartilage's porous ECM consists mostly of type II collagen, proteoglycans, water, and non-collagenous proteins (Ethier 2007). The material properties of cartilage, such as elastic modulus, are influenced by the ratios of these protein components (Woo 1988). The volume of articular cartilage of the knee was studied in healthy knees with no history of joint disease was measured as,  $7.6 \pm 1.6 \text{ cm}^3$  ( $8.3 \pm 1.6 \text{ cm}^3$  in men,  $6.7 \pm 0.9 \text{ cm}^3$  in women) with thickness of 1.5-3 mm (Nishimura 2005). The takeaway from this study was that physical size had more influence on cartilage volume rather than sex, described by the linear relationship: cartilage volume =  $0.113 \times \text{height} - 11.053$  (Nishimura 2005).

Unfortunately, articular cartilage lacks blood vessels so nutrients, immune cells, and other biochemical signals cannot be easily transferred between the cartilage and the rest of the body. Without the transport of the nutrients to the articular surface, cartilage has a very low capacity for healing and regeneration. Degradation of the cartilage becomes permanent and leads to OA.

The knee is the most common site of OA (Felson 1988). As the volume of cartilage decreases, the coefficient of friction between the articulating surfaces increases. A higher coefficient of friction requires larger forces to move the joint. Articular cartilage also has very few nerve endings which provides pain free movement. As it is worn down,

the nerves in bone become exposed to forces transmitted through the knee. This means patients with OA experience both joint stiffness and pain.

Varus deformity of the knee is related to the higher loading in the medial compartment compared to the lateral compartment. The unbalanced loading is compounded with loss in cartilage in the medial compartment so the joint space narrows (Theinpont 2016). The cycle of higher loading from varus deformity continues to degrade the joint.

Joint space narrowing can be measured radiographically as the distance between the medial condyle and medial tibial plateau. Varus deformity can also be observed from the relationship between the weight bearing and anatomical axes depicted in **Figure 1**. A varus knee will have a weight bearing axis that crosses the tibial plateau in the medial compartment. Substantial varus deformity was defined as a greater than 10-degree angle between the vertical line passing through the center of the knee and the theoretical loading line (Moreland 1987).

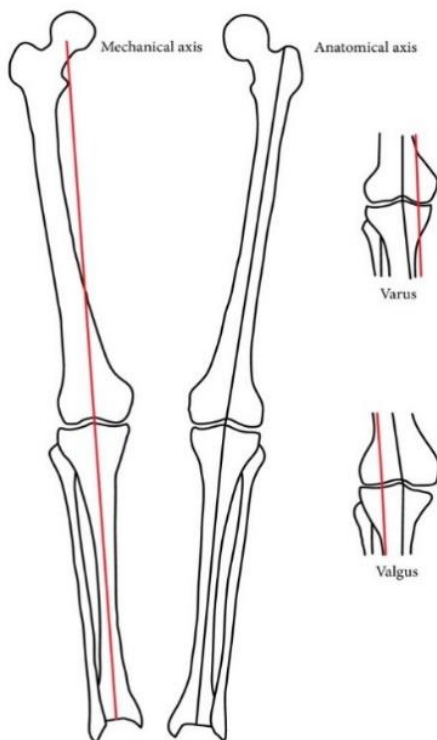


Figure 1 Graphic displaying the method for finding the mechanical and anatomical axis of the leg from radiographs. The mechanical axis or weight bearing line (red line) is drawn from the center of the femoral head to the center of the ankle. (Liu 2019)

## 2.2 Purpose of High Tibial Osteotomy (HTO)

OA is commonly treated with TKAs (Theinpont 2016). After cartilage is damaged, pain is experienced, and stance is varus, patients seek an intervention to relieve their immobilizing symptoms. TKAs involve removing the rough, bony interface of the joint, and replacing it with metallic and polymeric components. The varus angle is not corrected in this procedure. Rather, emphasis is placed on the alignment of the TKA components relative to each other to prevent implant failure (Ritter 2011).

The HTO procedure, to correct varus deformity, involves forming an open wedge in the tibia in the transverse plane in a medial to lateral direction. The wedge space is typically stabilized by a plate with locking screws until new bone tissue can grow in the open wedge. Bone graft is also commonly added to promote healing of the osteotomy site

(Woodacre 2016). Although the plate and locking screws typically hold the tibia in the new corrected angle, the osteotomy destabilizes the tibia to axial and torsional loads (Luo 2013, Spillane 2021). There are many plate designs to help combat this problem and encourage union of the neo-osseous tissue (Luo 2013).

Osteotomies are indicated for active patients, whose activity might be hindered by a TKA as well as younger patients with high BMI (Boyce 2019, Chen 2020, Preston 2014, Spillane 2021). There was no statistically significant difference in UKA and HTO outcomes (Liu 2019). Despite those results, HTOs correct the mechanical loading axis of the leg, and postpone the need for UKA and TKA (Jeon 2017, Santoso 2017, Sun 2017). This helps preserve the cartilage of the knee joint (particularly in the medial compartment), These factors have clinical and economic benefits to the patient and physician.

Surgical indications classify candidates for surgery who are likely to have successful outcomes. The ideal patient for an HTO is less than 60 years of age, has no severe articular destruction, isolated medial osteoarthritis, good range of motion, and no ligamentous instability (Aglietti 1983). Patient weight has not been found to influence the rate of complication of the HTO, however due to the current plate and screw technology, the destabilization of the tibia is not without risk of failure of hardware (Elson 2015, Liu 2019, Osti 2015, Woodacre 2016). Patients with high BMI that meet all other indications for HTO could be considered candidates for alignment of their lower leg mechanical axis if improved stabilization technology was developed.

Nearly 32% of HTO performed from 2010-2019 were performed on obese patients. UKAs are performed annually at a rate 2000 times higher than HTO (Cotton-

Betteridge 2022). Some potential failures of HTO include nonunion, tibial plateau fracture, lateral cartilage degradation and plate breakage (Liu 2019). Implant failure and osteotomy site damage are of concern when operating on patients with high BMI because the large defect at the osteotomy site that needs to fill with new bone. To ensure the osteotomy site fills with new bone to support the patient's BW, patients with high BMI will require a longer period of non-weight bearing time compared to lower BMI patients (Wolcott 2016, Woodacre 2016). Additionally, the size of the osteotomy is directly correlated to time to union, affecting the obese population who may be larger boned (Nemecek 2019, Stoffel 2004, Woodacre 2016). To address this problem, autologous bone graft or bone substitute can be used to fill the defect and catalyze bone ingrowth pathways. If the HTO fails or does not provide pain relief, most surgeons will revise to TKA (Jones 2019).

HTO has been shown to be a successful alternative to performing TKA or unicompartmental knee arthroplasty (UKA) on younger patients who want to remain active. This is because systematic review studies have found that patients who had HTOs had better range of motion than UKA patients (Santoso 2017). Published data about complication rates of HTO with respect to BMI is limited, but surgeons observe a correlation between HTO failure and high BMI from their clinical experience (Woodacre 2016). Improving the HTO procedure could make it more inclusive and minimize its complications.

The typical hardware used to stabilize the osteotomy, maintain the corrected angle, and allow for bone ingrowth at the osteotomy site are fixed angle devices and plates like the Tomofix (DePuy Synthes) or Puddu (Arthrex) plate. HTO complications



that arise from hardware are often due to plate interference with surrounding soft tissue structures, screw breakage, and collapse of the osteotomy site. Literature in general reports implant failure in the range of 2.2%-22.9% (Woodacre 2016). Broken screws were specifically reported in 4.2% of implants of 138 patients (Chae 2011), and one implant of 186 patients (Brinkman 2008). It was proposed that high BMI patients would be at a higher risk for all complications, but in the case where an open wedge must be maintained by a single plate, implant failure is of concern especially if early weight bearing is sought.

### **2.3 A Multi-Component Implant for Use in Tibial Osteotomy to Correct Varus Deformity in the Morbidly Obese**

HTO offers the advantage of postponing the need for TKA by correcting varus deformity to preserve articular cartilage in the medial compartment of the tibia. Surgeons are eager to expand the use of HTO to treat patients with high BMI, who suffers OA at higher rates and younger ages (King 2013).

A novel design for placement in the osteotomy site during the HTO procedure will support early weight bearing shown in **Figure 2**. It does not require the entire osteotomy defect to be filled with osseous tissue in order for the varus deformity to be corrected. A 4-component titanium alloy implant will support the restored mechanical axis. Bone ingrowth into the porous coating of the implant superior and inferior surfaces will secure the implant to the osteotomy site to prevent displacement from the osteotomy site into soft tissue structures. The most unique aspect of this implant design is the implant's multicomponent interlocking design to occupy the volume of the entire osteotomy site. This implant was designed with incision size in mind because incision

size is correlated to infection risk. If the implant was a singular piece, it would require a large incision, larger for an obese patient, which is considered a primary factor leading to failed treatment.

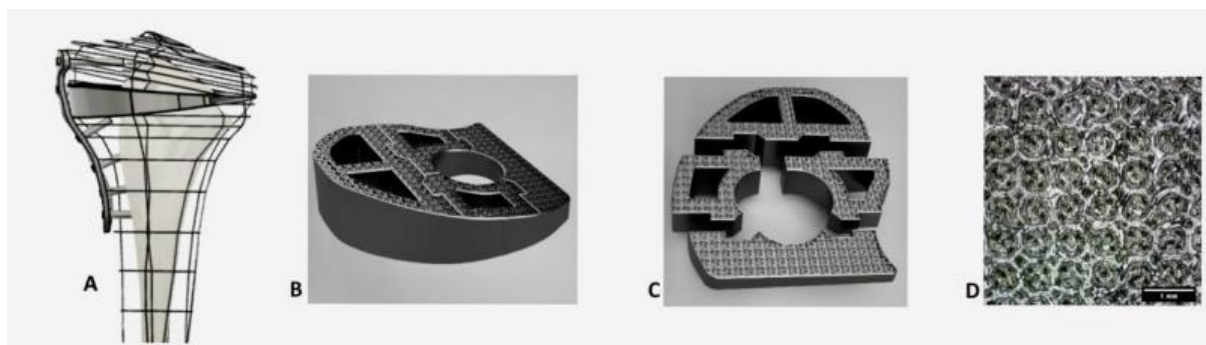


Figure 2. Depiction of novel multicomponent implant. (a) Implant and plate placed at osteotomy site (b) multi-component implant geometry with lattice surface rendering (c) disassembled view of implant (d) micrograph of the lattice with 550  $\mu\text{m}$  pore size (Spillane 2021)

Finite element analysis of the current HTO method with a plate and of the novel method of an osteotomy wedge in addition to the plate demonstrated that the combination of a plate and novel titanium alloy wedge decreased the stress in the plate by two orders of magnitude shown in **Figure 3**. The plate is designed to support the osteotomy site during healing but is not recommended to support body weight alone. Coupling the loading support of an implant in the wedge of the osteotomy with restricting movement of the osteotomy site with a plate is hypothesized to improve the biomechanics of the procedure and decrease the unstable nature of the procedure. The factor of safety of the plate increases as the loading decreases by as much as two orders of magnitude. The plate's role shifts from load bearing to stabilizing. It prevents the wedge from sliding out of the defect and improves the chance of osseointegration into the implant's porous coating.

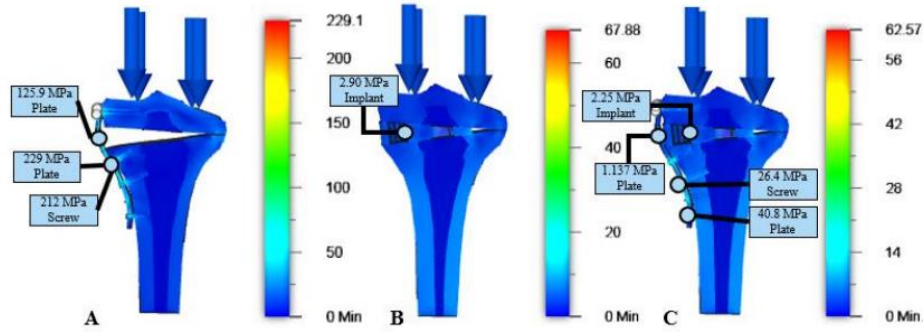


Figure 3 Von Mises stress distributions at mid-frontal plane for models: A) Plate-only; B) Implant-only; C) Plate and Implant (Spillane 2021)

Given the interlocking, multicomponent design of the novel implant, friction between the titanium alloy surfaces is important to consider. This is especially of concern after “metal on metal” in hip implants caused metal poisoning in patients. Although, this implant does not have the same level of risk because the parts will not be moving significant distances across each other with every step like the femoral head and acetabular cups do in hip implants. Rather, the components of this osteotomy will remain stable and be subjected only to micromotion and wear is hypothesized to be less severe.

#### 2.4 Fretting Corrosion, Tribology, and Inflammation

Practical surfaces are not as smooth as they appear to macroscopic senses of sight and touch. The small scale of roughness of a surface, commonly known as asperities, are depicted as steep peaks and valleys. When two solids appear in contact macroscopically, the regions of contact are limited to the pattern of interfacing microscopic asperities. Applied loads subject these interfacing surfaces to wear based on the material properties of the interfacing solids and the type of load. As contact load increases, the load distribution area increases since more asperities deform and surface roughness decreases.

Friction force is based on the relationship of the surface roughness of the two interacting surfaces and presence of lubrication. The friction force is relevant to the wear

of the implant because a higher coefficient of friction of the surfaces would mean less relative movement between the interfacing surfaces.

Wear rates are impacted by factors such as particle hardness, shape, and size, where harder, angular, and larger particles cause more wear. Lubrication is another important factor that impacts wear rate. Clean surfaces have tighter interface junctions making them less likely to experience relative motion from an applied load. If the junction is fractured, however, adhesive wear will occur as shown in **Figure 4**. Abrasive wear occurs when a harder surface shears off the surface of a softer interfacing material shown in **Figure 5**.

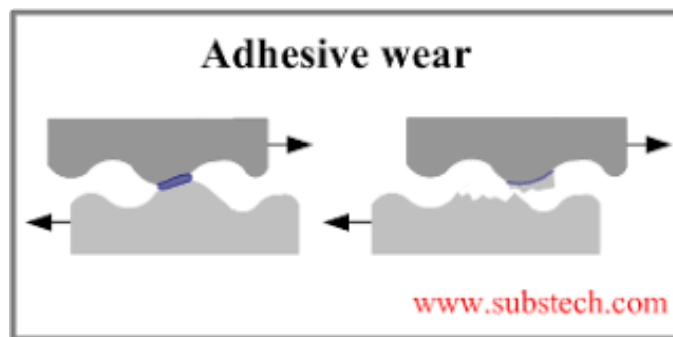


Figure 4 Adhesive wear diagram

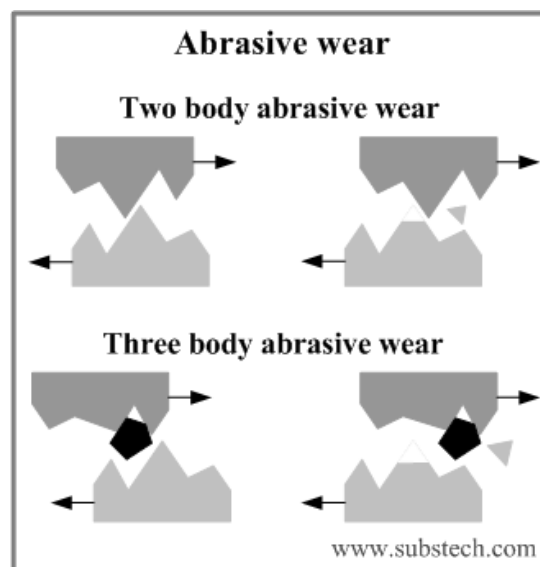


Figure 5 Two and three body abrasive wear diagrams

Fretting wear and corrosion are accelerated by acidic conditions where oxide debris can accumulate between interfaces and weaken the surfaces. After a high number of small amplitude oscillatory displacements from cyclic loading, fatigue cracks begin to form shown in **Figure 6**. Fatigue cracks can occur at lower levels of loading than the fatigue limit. Fretting damage can be minimized with rougher surfaces, decreased load, increased lubrication, and surface hardening. Surface hardening with surface rolling, shot peening, or case hardening subjects the material to compressive stress that preloads the material that reduces crack propagation. This means that manufacturing and other surface treatments are of great consideration when fretting corrosion is suspected.

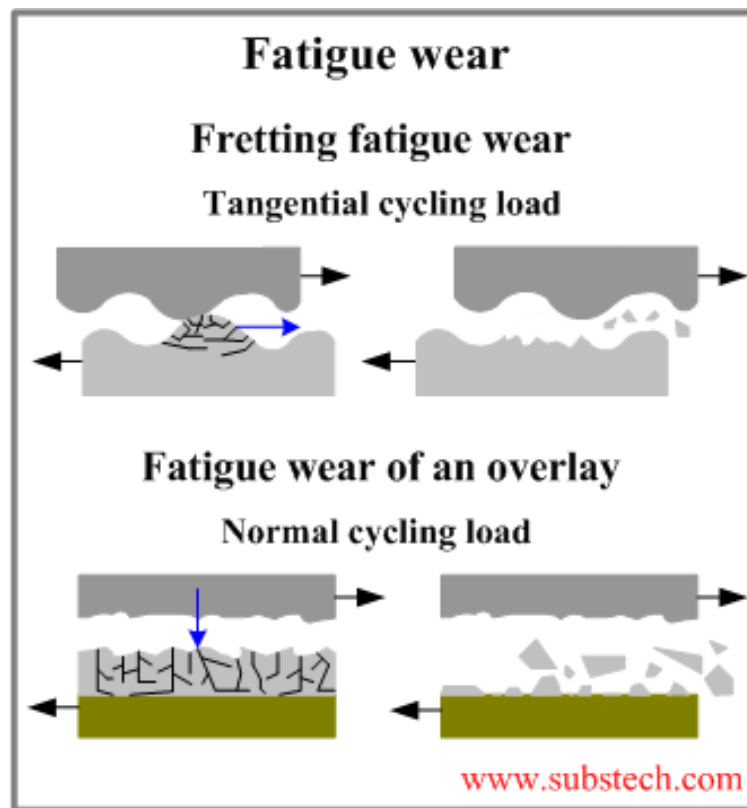


Figure 6 Fretting and fatigue wear diagram

Fretting can be measured by following the ASTM guide for gravimetric wear assessment (ASTM F1714-96) by measuring weight loss of implants or volumetric wear

over a set number of wear cycles. Inspection is also conducted via visual, profilometric and replication measurements. Extreme care must be taken to avoid contamination because the small amounts of wear particles cannot be confounded with substances. Wear testing on hard-on-hard Total Hip Replacement systems usually follows ASTM F3047-M Standard Guide for High Demand Hip Simulator Wear Testing of Hard-on-hard Articulations. An example for a fretting wear fixture that meets ASTM F3047M specification is demonstrated in **Figure 7**. This fixture encases the regions of interest in a closed container. The acetabular cup of the hip implant is connected to a machine that can cyclically load the implant to imitate walking and other hip activities. Wear particles are collected in the container during the test and are analyzed after the test is complete. Different phases of wear classified by the amount of wear vs. number of load cycles are depicted in **Figure 8**.

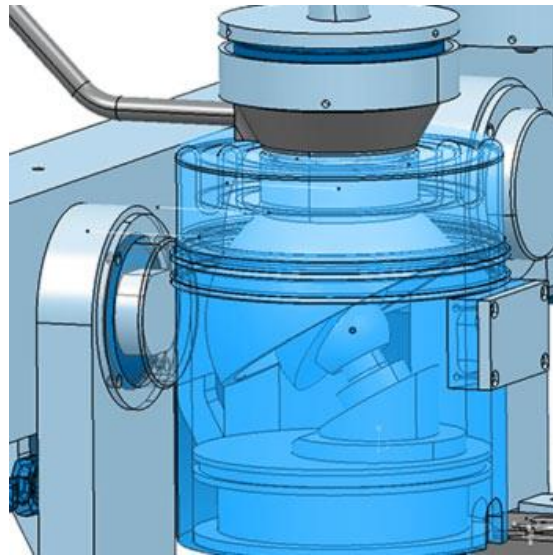


Figure 7 Endolab fixture for measuring wear according to ASTM F3047M-15

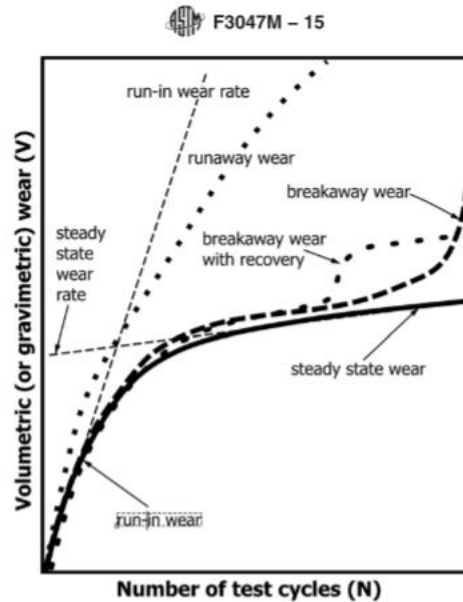


FIG. 2 Different Modes/Phases of Wear Illustrated Schematically

Figure 6 Graph of volumetric wear vs number of test cycles from ASTM F3047M-15

Worn surfaces can be observed from a broad range of magnification levels. At the macroscopic level, discoloration and reflective surfaces created from wear can be observed with the naked eye. At higher magnifications, the surface microstructure including asperities can be visualized. Digital cameras and light microscopes are critical instruments for examining and imaging surfaces at magnifications from 1x to 100x. Some imaging techniques to record the vertical aspects of the asperities involve altering the angle of light so it can be refracted by the surface irregularities. Scanning electron microscopy (SEM) technology magnifies the surface up to 100000x to the. A beam of electrons is sent across the sample and the backscattered electrons are collected to produce the image. Individual asperities can be visualized at this level and information about the shape of asperities is collected. Additionally, SEM has additional capabilities like energy dispersive x-ray spectroscopy (EDS) that measure the types and mass percent of individual elements. This technology can provide insights to the types of particles

involved in fretting and adhesive corrosion, especially when the interfacing surfaces are made of two different materials.

Profilometry is a technique to study surface topography. There are two main types of profilometers: optical and stylus. The optical profilometers are non-contact and stylus profilometers contact the surface. Profilometers measure height, depth and spacing of individual asperities. Images can also be recorded. In tribology, quantifying the unique surface characteristics is challenging yet important for design and manufacture to match an intended use. Optical profilometers provide the best results when used on reflective surfaces. Stylus profilometers are limited by the size of the stylus tip; there are a variety of sizes, shapes, and materials to match the needed specifications.

## **2.5 Wear in Orthopedic Implants**

Orthopedic implants are typically made from metallic (titanium alloy and cobalt chromium) and polymeric (polyetheretherketone (PEEK) and ultra-high molecular weight polyethylene (UHMWPE)) components. These foreign materials, despite exposure to synovial fluid and other biological lubricating fluids, are subject to wear. Wear particles accelerate the wear rate as described in the previous section, but also elicit a foreign body response from the immune system and can cause osteolysis, a degradation and weakening of bone tissue).

The chief concerns of orthopedic implant designs in relation to wear are both the foreign body response to non-native materials and prosthetic loosening. Prosthetic loosening, especially of screws or hip sockets can impact the stability of the procedure and increase the chance of non-union. Another consideration of the interaction between the biological environment and the non-biologic materials is the relationship between



acidity and corrosion. Designers must be especially aware when creating an implant with multiple interfacing components, especially when two different types of metals are used, and galvanic corrosion occurs from their electrical contact. The pH of marrow where the implant will be placed is 7.38 (Miettinen 2012). The pH of synovial fluid is 7.78 in native joints, 7.60 at revision aseptic operations, and 7.55 at revision septic operations (Milosev 2017).

The foreign body response to a new implant involves many stages, cells, and biological factors. The immune response begins at the beginning of the procedure with upregulation of inflammatory factors, mast cells, neutrophils, and monocytes (Anderson 2008). Eventually, fibroblasts and osteoblasts will migrate and mature to form a fibrous capsule surrounding the implant. Inflammation is a normal part of the healing process. A prolonged immune response and inflammation can lead to long term problems because of the cytotoxicity to attempt to expel the foreign substance. This can lead to degradation of the bone tissue, rejection of the implant, and infection. Wear particles also elicit an immune response because the particles are perceived as biological invaders the cells want to expel to maintain homeostasis.

Engineers designed hip implants with improved wear rates that included a metal acetabular cup and metal femoral head component that would interface. Metal has higher fatigue and yield strengths than polymeric components and could last longer. The hip joint has a large range of motion and has a large area of high contact regions. The relative motion between the acetabular cup and femoral head causes wear at the high contact regions of the components. Wear releases wear particles, loosens the components' fit, and decreases the stability of the joint.

Unfortunately, an unforeseen issue rose where cobalt chrome femoral heads and acetabular cups that led to metallosis from entrance of toxic metallic wear particles into the bloodstream (Oliveira 2014). The experience of this product reaching the market makes the orthopedic industry especially concerned about any type of metal wear. The allowable concentration of titanium alloy in the human blood is unknown, but the concentration of cobalt and chromium of 7 ug/L is indicative of a failed implant (Swiatkowska 2019). Other orthopedic devices that involve metal on metal interfaces like plates and screws are not subject to motion the way the hip prosthesis is. The motion in this diarthrodial joint is the reason for so much wear. Wear is not prevalent at those rates when the two components fit snugly together. In the novel implant proposed above, there is no design for a secure fit and the pieces will be held together by compression of the osteotomy with a plate.

## **2.6 Mapping Fretting to Relate Wear to Contact Forces and Interfaces**

Performing physical tests to measure wear are generally required by the FDA 510k process to show safety and efficacy at the same or higher level of a similar existing device. These are best shown by performing tests with specified standard procedures created by the International Organization for Standardization (ISO) and ASTM International.

Finite element models can solve complex mechanical problems. It is useful for determining stress a stress map of an object which cannot be directly physically measured. In the metal-on-metal hip implants described above, contact stress was determined to range between 10 and 30 MPa based on finite element analysis calculations (Yew 2003). Contact stress is what causes the wear of the surfaces, even though it can

typically not be measured experimentally. Stress at interfaces works by creating subsurface stresses which cause particles to break off. The regions with the highest contact pressure in a finite element analysis represent the regions that experience the highest magnitude of contact.

A previous student of Dr. Anderson's, Dr. Villarraga, created a finite element model in ABAQUS to evaluate the contact pressure between screws, plates, and bones of cervical spine plates. This was done by loading canine CT scans and converting them into 3D geometries to modify and assign properties to. A hexahedral mesh of varying element densities was assigned. The first step in the analysis involved the defining an initial overlap of the plate tightening to the bone by screw pretension. This model is unique in its definition of contact interfaces by "overclosure". Contact pressure was maximum in the bone under the plate. A hexahedral element mesh across the model was used. The average contact pressure in the model spans from 53 MPa to 281 MPa. The first step in the analysis involved the defining an initial overlap of the plate tightening to the bone by screw pretension. This model was used to analyze the von Mises stress on the plate under physiological loading and validated by a 3-point bending bench test.

## **2.7 Hypothesis**

It is hypothesized that there will be a correlation between theoretical contact stresses mapped with finite element analysis software and wear distribution measured physically from presence of wear particles in lubricating fluid and changes in surface finish on the implant interfaces.

## CHAPTER 3: MATERIALS & METHODS

### 3.1 Implant Prototype Fabrication

Stainless steel and polylactic acid (PLA) implant prototypes were subject to physical testing. The stainless-steel implant prototype was printed at Scale Workspace (New Orleans, LA) using a Markforged Metal X machine (Markforged, Watertown, MA). 17-4 PH Stainless Steel filament was used, and composition and mechanical property information is included in the appendix. The machine extruded a metal powder, wax, and polymer slurry resulting in solid infill parts. They were washed with opteon for 12-36 hours to remove the wax. After air drying, the parts are sintered in a 98% Argon 2% hydrogen chamber. Post processing was then done by the machinists to ensure that the components fit together as intended. The layers have post sintering resolution of 50 um to 125 um.

PLA implant prototypes were fabricated at the Scot Akerman MakerSpace at Tulane University using Ultimaker 3 (Ultimaker, Utrecht, Netherlands) extrusion printers using fused filament fabrication (FFF) with 2.85 mm diameter PLA filament (Gizmo Dorks LLC, Temple City, CA). The implant prototypes were printed with 99% infill. After printing, the surface AF whose location is shown in **Figure 8** was filed until the components could fit together properly.

### 3.2 Wear Assessment of Implant in Simulator Device

The procedure used was modeled off the ASTM guide for a weight-loss method of wear determination for the polymeric components used with hip joint prostheses. One

major difference between the guide and the procedure followed for this study was in the use of serum for lubrication. The potential impact of this change is included in the discussion. Otherwise, the method used is like the guide following a dynamic load profile representative of the human knee-joint forces during walking rather than the hip-joint. “The basis for this weight-loss method for wear measurement was originally developed (3) for pin-on-disk wear studies (see Practice F732) and has been extended to total hip replacements (4,5) femoral-tibial knee prostheses (6), and to femoropatellar knee prostheses (6,7).” Weight loss methods of testing for wear are standard because wear is a unique form of deformation where mass is not conserved. A measurement of change in geometry alone could confound wear with the effects of creep and plastic deformation. Although the model guide was designed for measuring wear of a polymeric face against a metal face, the simulation in this study measures the wear of a metal-on-metal interface. It was suggested that metal on metal combinations be “monitored using a linear, variable displacement transducer or other profilometric techniques.” In this thesis, a combination of optical surface observations and weight loss techniques were used and are described below in the measurements section. Based on the results of this study, the techniques suggested in the guide may be chosen to be pursued later.

### **3.2.1 Simulator Device Design**

In this study the simulator was a combination of an ADMET eXpert 8600 axial torsion testing machine (ADMET, Inc., Norwood, MA) and a custom fixture designed and fabricated by the investigators shown in **Figure 9**. The top and bottom fixture were custom designed to the shape of the implant. The top fixture has the inverse angle of the

implant. The bottom implant is flat and has 36 cylindrical wells that are 7.5 mm diameter and 10 mm high shown in **Figure 10**.

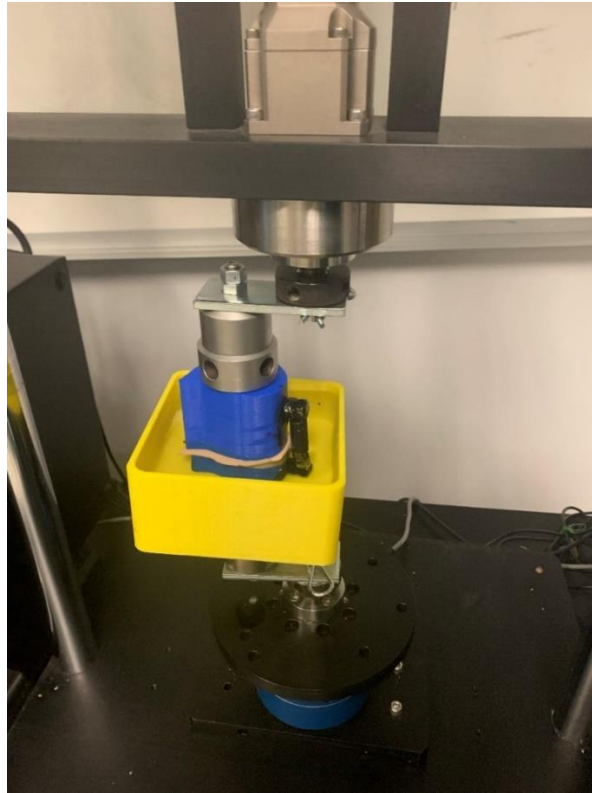


Figure 7 Test fixture set up in ADMET axial torsion testing machine

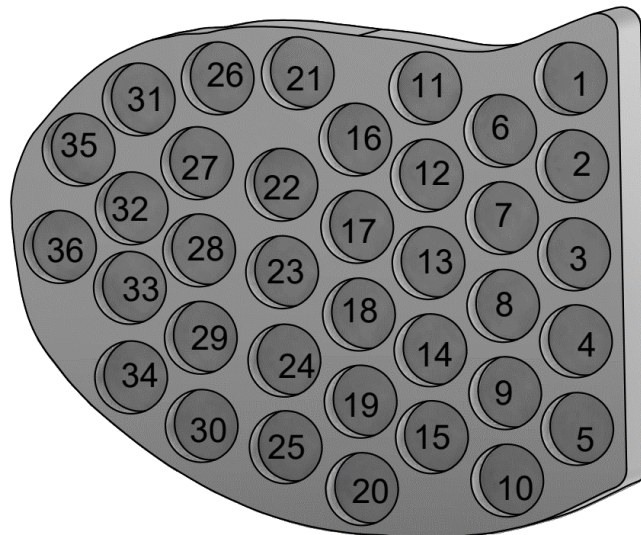


Figure 8 Surface upon which the test sample was set

The chamber of the simulator was designed with the ASTM guide in mind; made of non-corrosive materials, able to be cleaned between tests, and hold lubricant in which the test specimen can be submerged. The fixture included a basin to be used as a water bath. Additionally, the fixture clamped the implant prototype within the open wedge space via springs covered in rubber. The implant components were allowed to move relative to each other in motion that mimics its placement in the osteotomy site. Friction forces between the interfacing components of the fixture and implant were assumed constant. Due to resource limitations, deionized water was used instead of bovine blood serum. The volume of the lubricant was monitored and kept constant throughout the test duration by replacing evaporated fluid mixture with deionized water.

### **3.2.2 Sample Preparation**

The standard recommends sterilizing components in a manner typical of clinical use as it may affect the wear properties. This may mean autoclaving. The forgoing of serum use means that the potential impact of reaction to bacteria or other biological contaminants will not impact the wear due to reaction with the serum. Additionally, stainless steel is inert and will not be affected by the potential contaminants for the relatively short length of the trial. This study however pays close attention to the cleaning of the test specimen both prior to and after the tests. Nonbiological contaminants could affect the wear as well as potentially compound the measurements of mass used to quantify wear. The relevant ASTM standard is contained in **Appendix A**. It is performed on each implant component. At the conclusion of the cleaning process, each clean, dry implant components was weighed three times using a microbalance.

### 3.2.3 Loading Conditions

After the implant was cleaned and initial measurements were recorded, the multicomponent implant with 4 components. The tests were conducted at room temperature. The ADMET machine was lowered to a preload compression between 3 and 5 kg. At a rate of 1 Hz, the machine lowered 1mm and raised 1 mm.

The standard suggests that in high-wear low-sorption materials, the wear rate can be established in roughly 50,000 cycles. Measurements occurred pre-test, after 10,000 cycles and after 50,000 cycles. While replicate tests would be needed to report an accurate value of the wear and its relationship to contact stress, this study aims only to show that a relationship of wear exists with contact stress shown in computer simulations.

### 3.2.4 Measurements

Each component of the implant was weighed again three times at the conclusion of 50,000 machine cycles and a cleaning process. After 10,000 and 50,000 cycles, a sample of 50 uL of the lubricant was collected from each well of the bottom fixture and weighed. This was done three times for each well. Before reloading the test or control implant and resuming the test, images of the implant-implant interfaces were inspected with a digital microscope (AVEN Tools, Ann Arbor, MI). Any macroscopic wear defect was imaged with a camera and measured.

In addition, scanning electron microscope images (SEM) were taken of select interfaces before and after the complete wear test of the stainless-steel implant with a variable pressure Hitachi 3400 electron microscope.



### 3.3 Characterization of Contact Stress by Finite Element Model

Abaqus FEA (Dassault Systèmes, Vélizy-Villacoublay, France) was utilized to understand the regions of highest von Mises stress and contact pressure that cannot be physically probed during a physical study. Contact pressure was assumed to be a hard contact with the following constraints. The materials in the study involved PLA and stainless steel, the material properties derived from matweb.com and listed in the table below. The surface conditions were defined by penalty interactions of 0.3 between the stainless steel and PLA surfaces and 0.15 between the stainless steel and stainless-steel surface.

A mesh was assigned to independent instances. The mesh on the implant had global seed size of 1 of freely assigned hexahedral elements. The mesh of the fixtures on the top and bottom had a finer mesh towards the implant in the z (vertical) direction from 0.5 to 3 seed size. This mesh region extended 13 mm from the superior surface of the bottom fixture and up 25 mm from the lateral and inferior aspect of the top fixture. That seed was also oriented to be smaller size towards the interfaces of the stainless-steel interfaces and larger as the distance from the interfaces in the xy plane increased. This mesh produced hexahedral elements. Tetrahedral elements were created by a seed size from 3 to 5 from the edge of the hexahedral mesh to the extent of the knobs of the fixture.

The load assigned to the finite element model was added 47 mm to the medial side of the top fixture knob using a tie constraint to a reference point. The load was assigned to the reference point using a boundary condition definition that moved the top fixture towards the bottom fixture 1 mm, as performed in the physical test. A tie constraint to 47 mm to the medial side of the bottom knob was also placed which

connected the fixture to a boundary condition that restricted movement and rotation in all directions.

### **3.4 Statistical Analysis**

A two tailed student's t-test with significance of  $p < 0.05$  was used to calculate statistical significance between the differences in weights of each component before and after the cyclic loading as well as the differences in weights of 50  $\mu\text{l}$  of water from each well after 10,000 and 50,000 total cycles.

## CHAPTER 4: RESULTS

### 4.1 Implant Interface Mapping Scheme

The results of this thesis rely on an organized system of reference to each surface of the implant. Each interfacing surface was assigned a unique name that it is referred to from this point forward. There are a total of 37 interfacing surfaces: 9 medial, 10 anterior, 10 posterior, and 8 lateral. The interfaces are not visible in the 2D scheme in **Figure 11**; however, the black lines represent the surfaces visible in the 3D exploded view of the implant in **Figure 12**. For example, the letter A refers to the anterior most surface on the lateral component that interfaces with the anterior component.

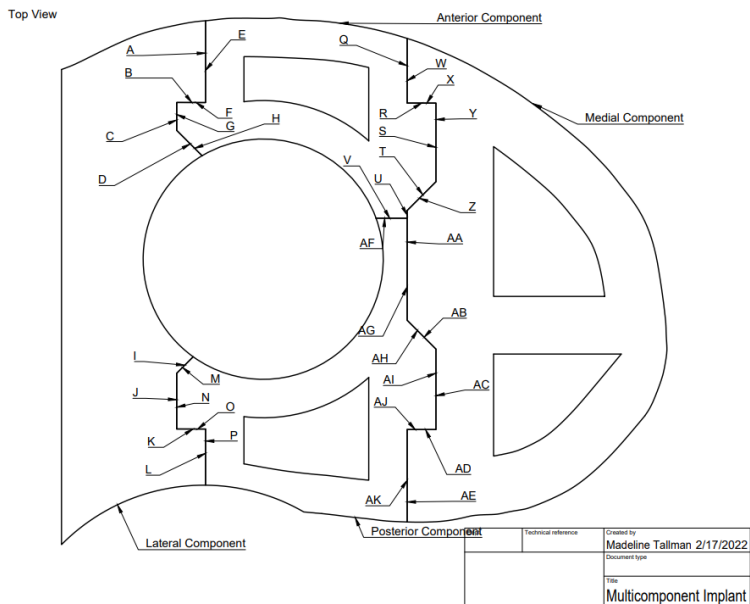


Figure 9 Map of implant and the surfaces of interest at stainless steel to stainless steel interfaces

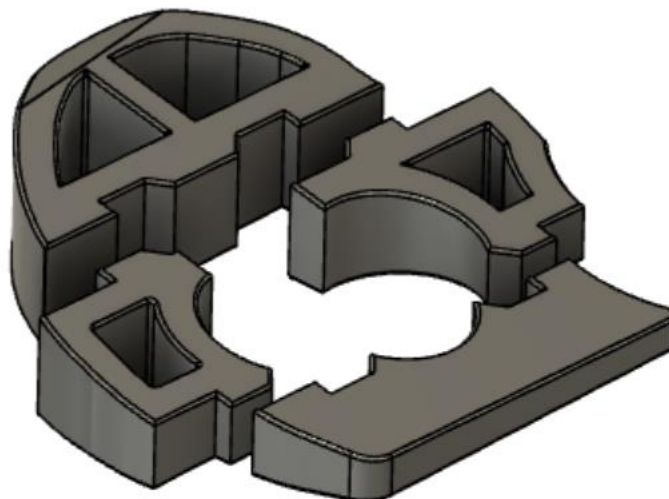


Figure 10 Exploded view of implant. Medial component is closest to the top left corner. Posterior component is closest to the top right corner. Anterior component is closest to the bottom left corner and the lateral component is closest to the bottom right corner

## 4.2 Component Weight Loss

There was a decrease in each component's mass between pre and post-test weighing. The largest decrease occurred in the medial component by 0.21 g. The smallest decrease occurred in the anterior component, by 0.5 mg. The average decrease in mass across all components was 2 mg. Both the medial and lateral components had a statistically significant decrease in mass. **Table 1** describes the change in mass of each component.

Table 1 Stainless steel implant component weights before and after 50,000 cycles of cyclic loading

	Pre-Test Mass (g)	Post-50,000 Cycles Mass (g)	P-Value
Medial	77.76	77.75	<0.01
Lateral	25.80	25.80	0.048
Anterior	22.61	22.61	0.939
Posterior	22.24	22.23	0.314

## 4.3 Optical Wear Patterns

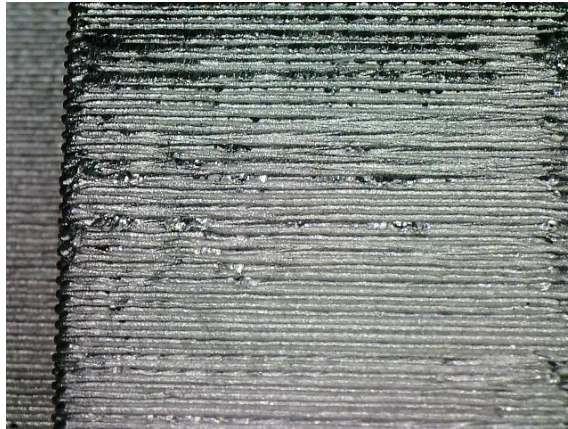
Visual inspection of each surface at different points of the testing process demonstrated physical evidence of wear. The three images of **Figure 13** are from before

testing, after 10,000 cycles of loading, and after 50,000 cycles. Noticeable areas where wear scarring expands and intensifies are in the top quarter and middle third of each image.

(a)



(b)



(c)

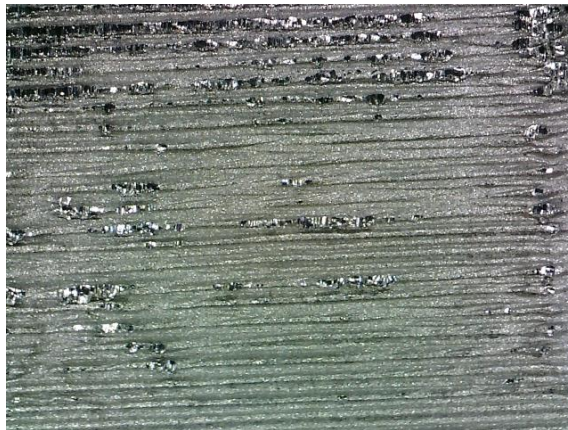
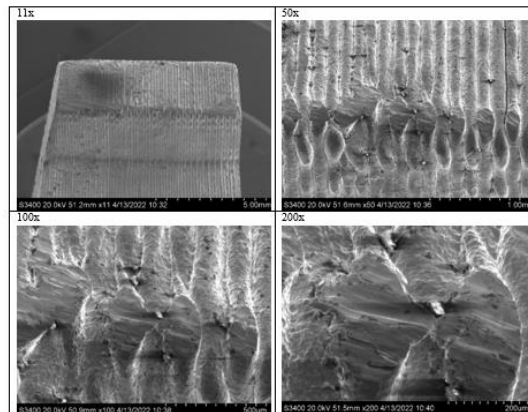


Figure 11 Digital microscope images from surface S at intervals (a) pre-test (b) after 10,000 loading cycles and (c) after 50,000 loading cycles

Visual inspection of surfaces was also performed at higher powers with SEM. Images were taken before testing and after 50,000 loading cycles. The images taken at the corner between surfaces F and G are shown below in **Figure 14**. This corner has more noticeable scratches after 50,000 loading cycles especially under 100x and 200x magnification. Under 200x magnification in the image taken after 50,000 loading cycles, there also appears to be a more granulated surface as opposed to a smoother surface before testing. Finally, the small protrusions that appear as white specks in the 50x, 100x, and 200x images taken before testing are not present in the images taken after 50,000 loading cycles.

(a)



(b)

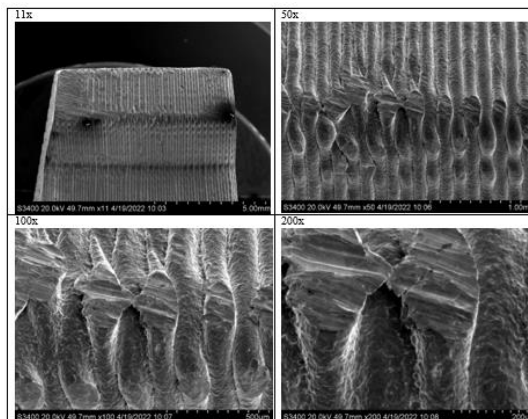


Figure 12 SEM images of surfaces E, F, and G (a) pre-test and (b) post 50,000 cycles

#### 4.4 General Computational Results with Von Mises Stress

The maximum von Mises stress measured in the computational model was 10.87 Pa at the posteromedial interface of the medial component. A uniform colormap described in **Figure 15** qualitatively describes the stress distribution and provides a key from interpreting results for each component. It spans from 0 to 10.87 Pa.

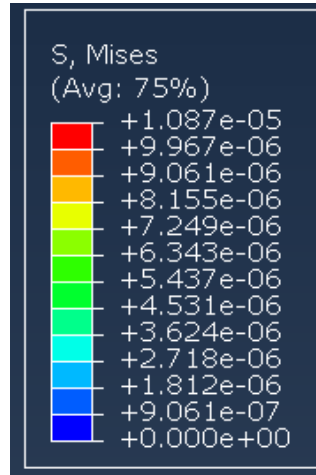


Figure 13 Color map of von Mises stress in MPa

**Figure 16** displays the implant with high von Mises stress concentrations around the central cylindrical extruded cut. There is also a high stress region at the posteromedial component interface. To a lesser extent, there is stress indicated by lighter blue on the superior surface of the implant at each component interface location.

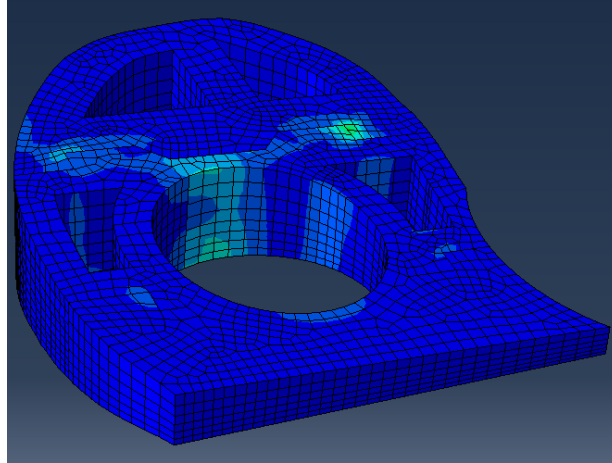


Figure 14 Von Mises stress of all components. The maximum mises stress in the implant is 10.87 Pa.

**Figure 17** shows the component interfacing surfaces of the medial implant. The highest von Mises stress in the implant is on the medial component where it interacts with the posterior component. It is depicted in the red on the corner of the AD and AE surfaces. There is also a high stress region where the W, X, and Y surfaces of the medial component interact with the anterior component.

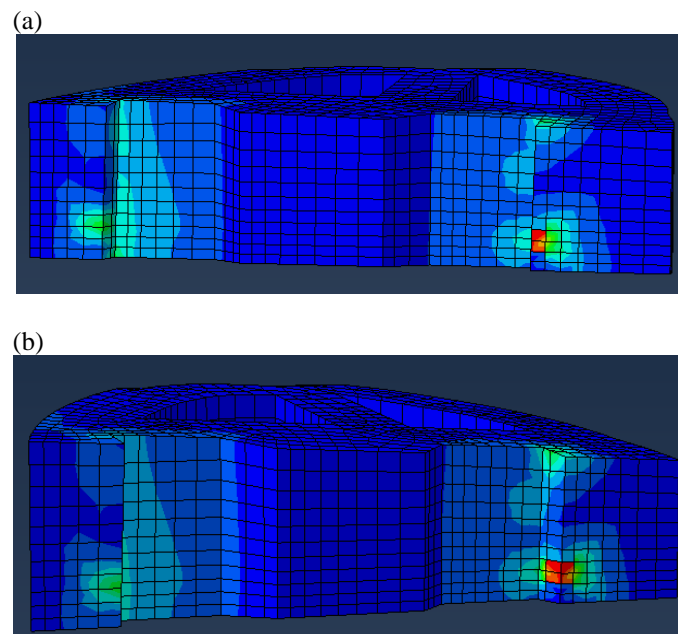


Figure 15 Von Mises stress of exterior of the medial component in two different views: (a) surfaces W, X, Y, Z, AA, AB, AC, AE, (b) and surfaces W, Y, Z, AA, AB, AC, AD, AE. The maximum Mises stress in the medial component is 10.87 Pa.



The lateral component shown in **Figure 18** has the smallest amount of von Mises stress. This is concluded because the surfaces lack a brightly colored stress map with green, yellow, and red regions. There are still high stress regions, most notably along the extruded cylindrical cut, the corner of the A and B surfaces and the corner of the J and K surface.

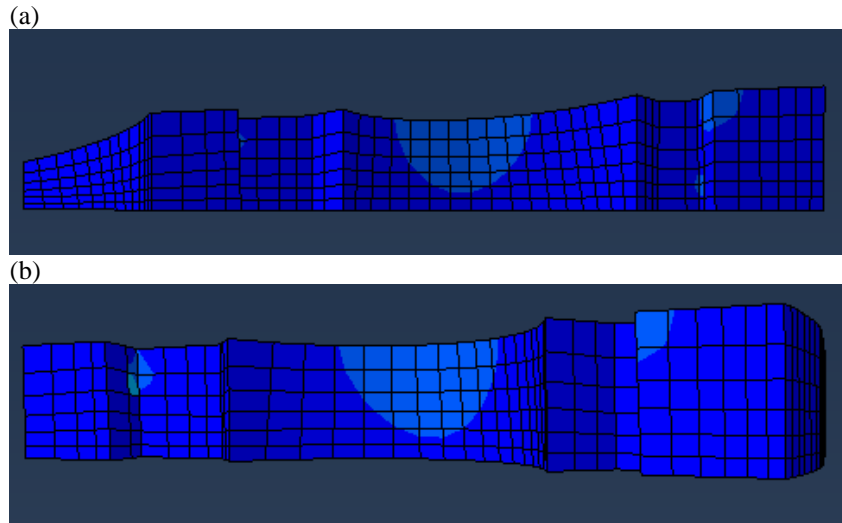


Figure 16 Von Mises stress of exterior of lateral component in two different views: (a) surfaces A, B, C, D, I, J, L (b) and surfaces A, C, D, E, J, K, L. The maximum Mises stress in the lateral component is 2.19 Pa.

The anterior component in **Figure 19** has its highest stress regions located on surfaces where they interface with the surfaces of the medial and lateral component.

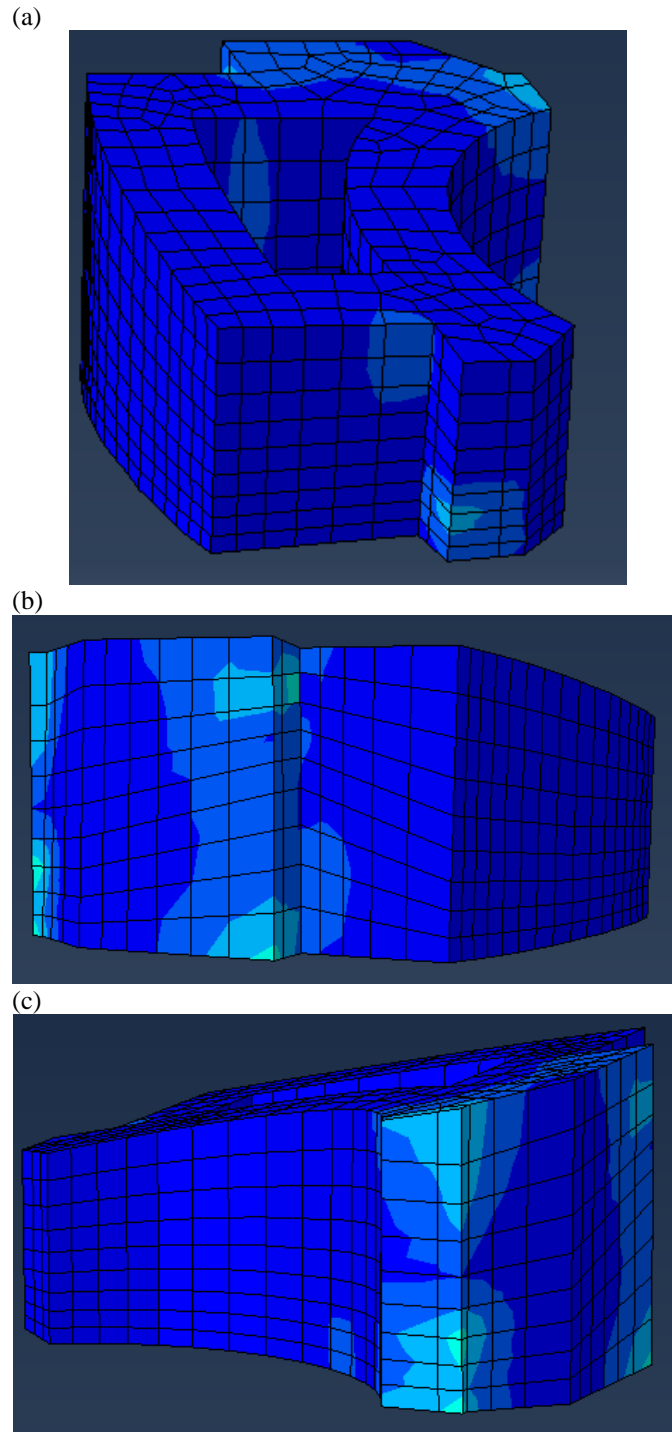


Figure 17 Von Mises stress of exterior of anterior component in three different views: (b) surfaces E, F, G, and H, (c) surfaces Q, R, S, V and U, and (d) surfaces S, V, U, and T. The maximum Mises stress in anterior component is 3.93 Pa.

The posterior component in **Figure 20** has the highest stress at the corner of AI and AJ. It also has high stress in the cylindrical extruded cut region.

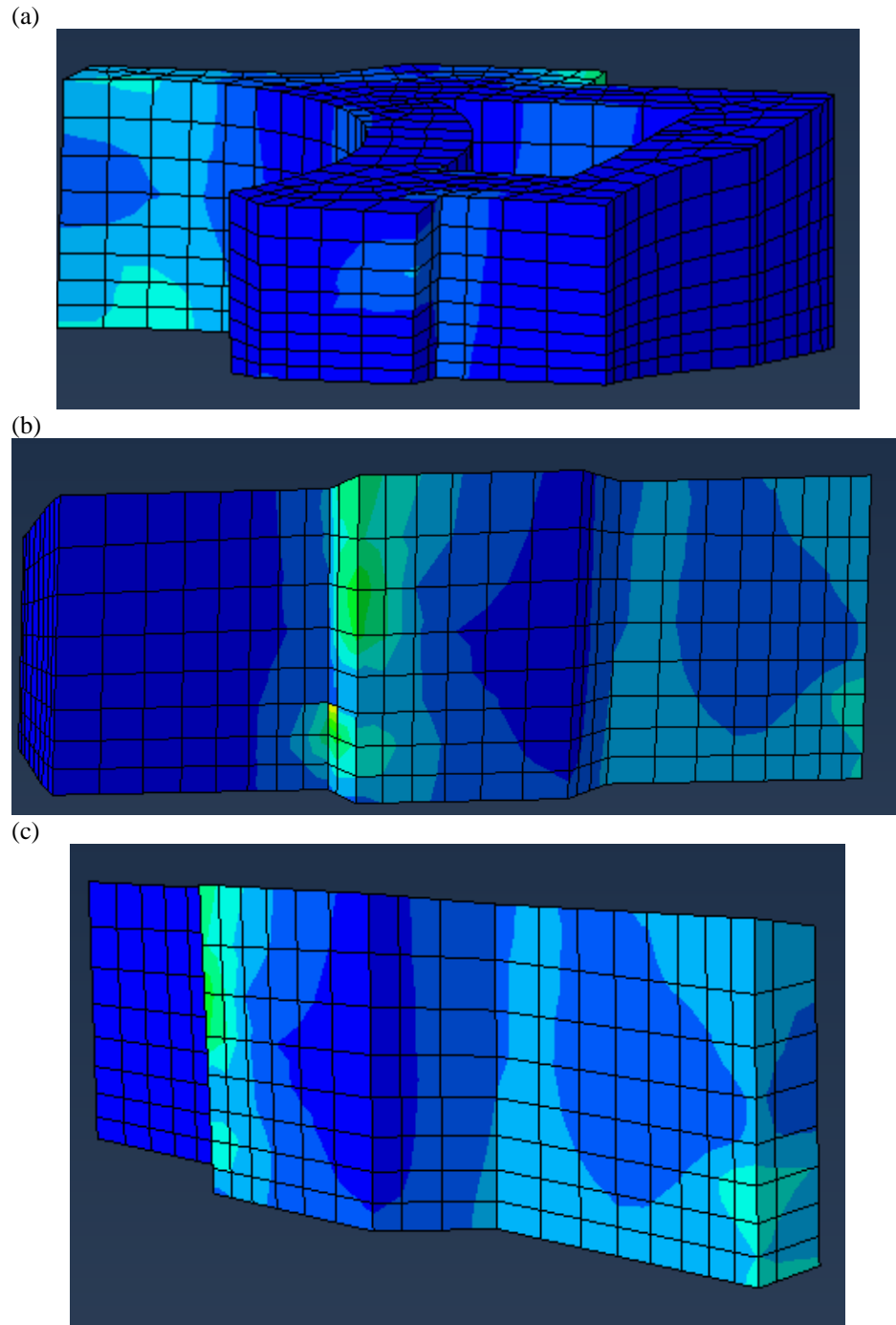


Figure 18 Von Mises stress of exterior of posterior component in three different views: (a) surfaces M, N, O, P, (b) surfaces AG, AH, AI, AJ, AK, and (c) AF, AG, AH, AI, AK. The maximum Mises stress in the posterior component is 8.20 Pa.

#### 4.5 Wear Particles Collected Under Interfaces

After the stainless-steel implant prototype was loaded for 10,000 cycles, 13 out of 36 wells were filled with water and the relative densities were measured. The maximum relative density was 1.05 at the well below the interface of the medial and anterior components. There was a statistically significant difference with  $p=0.026$  between the density of the water in the well and deionized water shown in **Figure 21**.

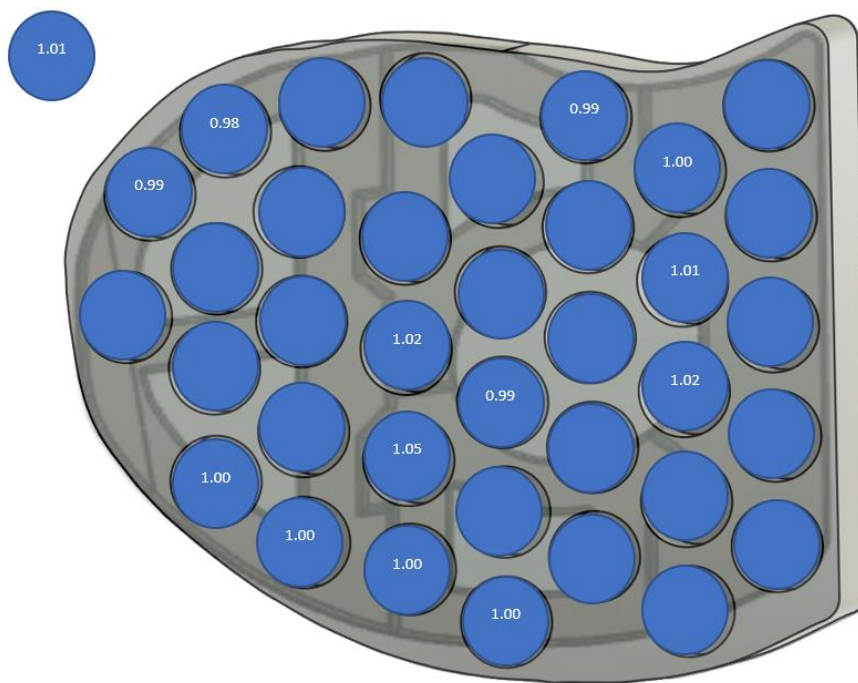


Figure 19 Relative sample weights after 10,000 loading cycles on a stainless-steel implant

After 50,000 loading cycles were applied to the stainless-steel implant prototype, 33 of the 36 wells were filled with water and had their relative densities measured. The maximum relative density was measured to be 1.06 found in two wells below the medial component and its interface with the anterior and posterior components. There was no statistical significance found between the density of the water in any wells and the deionized water. These results are shown in **Figure 22**.

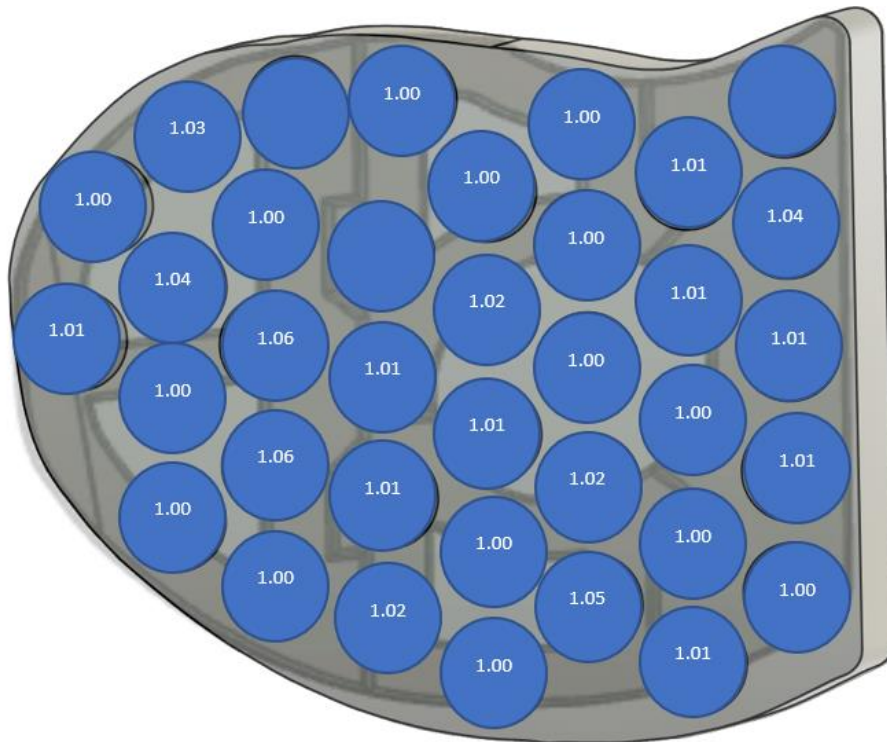


Figure 20 Relative sample weights after 50,000 loading cycles on a stainless-steel implant

#### 4.6 Comparing Contact Pressure from Computational Model with Optical Wear

##### Scar Patterns

The contact pressure is the stress on the surface of the implant due to contact with interfacing components. A uniform color map in **Figure 23**, which ranges from 0 to 9.34 Pa is a key for qualitatively evaluating each surface of the component.

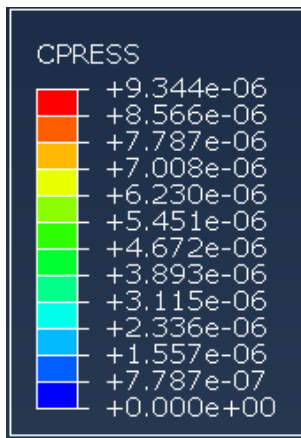


Figure 21 Color map of contact stress in MPa.

**Figure 24** shows the medial component of the implant which has the highest contact stress of the entire implant, with a maximum contact stress of 9.34 Pa. Its highest stress concentration regions are on the X and AD surfaces, which directly interface the R surface of the anterior component and the AJ surface of the posterior component. In the images of the implant after 50,000 loading cycles, wear scars are noticeable in the top fifth of surface X. There are not any noticeable wear scars on the surface AJ.

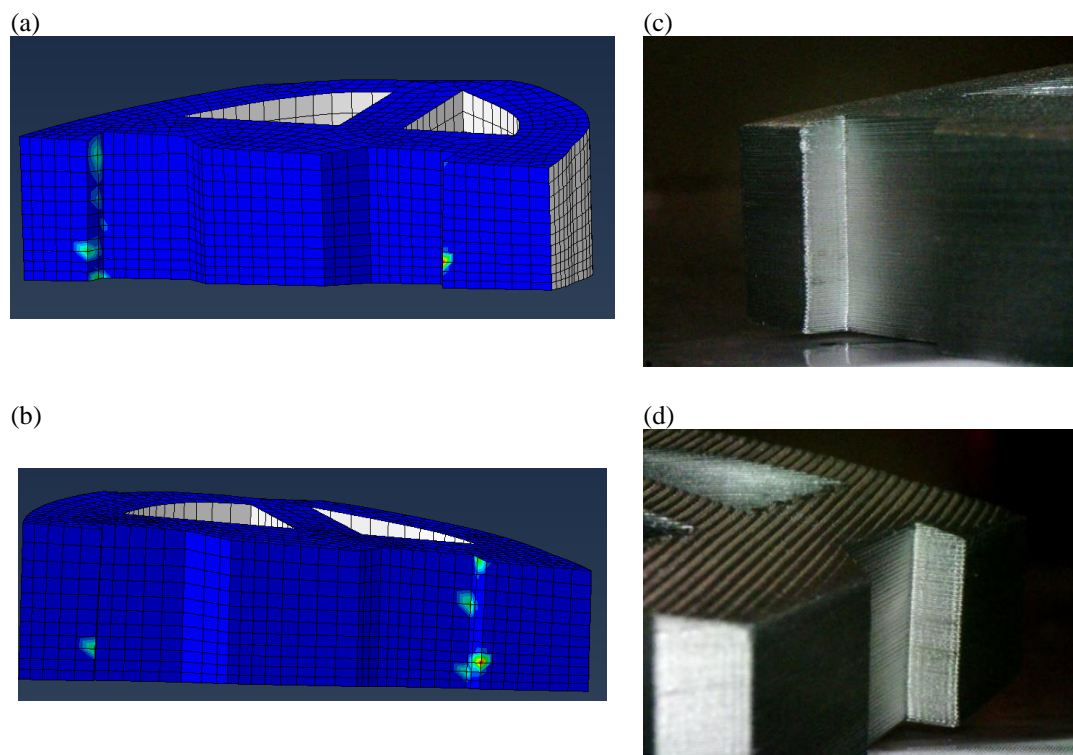


Figure 22 Contact stress of the exterior of the medial component in two different views including: (a) surfaces W, X, Y, Z, AA, AB, AC, AE, (c) and surfaces W, Y, Z, AA, AB, AC, AD, AE. The maximum contact stress in the medial component is 9.34 Pa. Images of surfaces (c) W, X, and Y and (d) Z, AA, AC, AD capture the regions where the highest contact stress points were found in the finite element model after 50,000 cycles.

**Figure 25** shows the lateral component of the implant which has the lowest contact stress of the entire implant, with a maximum contact stress of 2.00 Pa. Its highest stress concentration regions are on the B, C and K surfaces, which directly interface the F and G surfaces of the anterior component and the O surface of the posterior component. In the images of the implant after 50,000 loading cycles, wear scars are noticeable a third

of the way up from the bottom on surface B and at the horizontal and vertical midpoint of surface K.

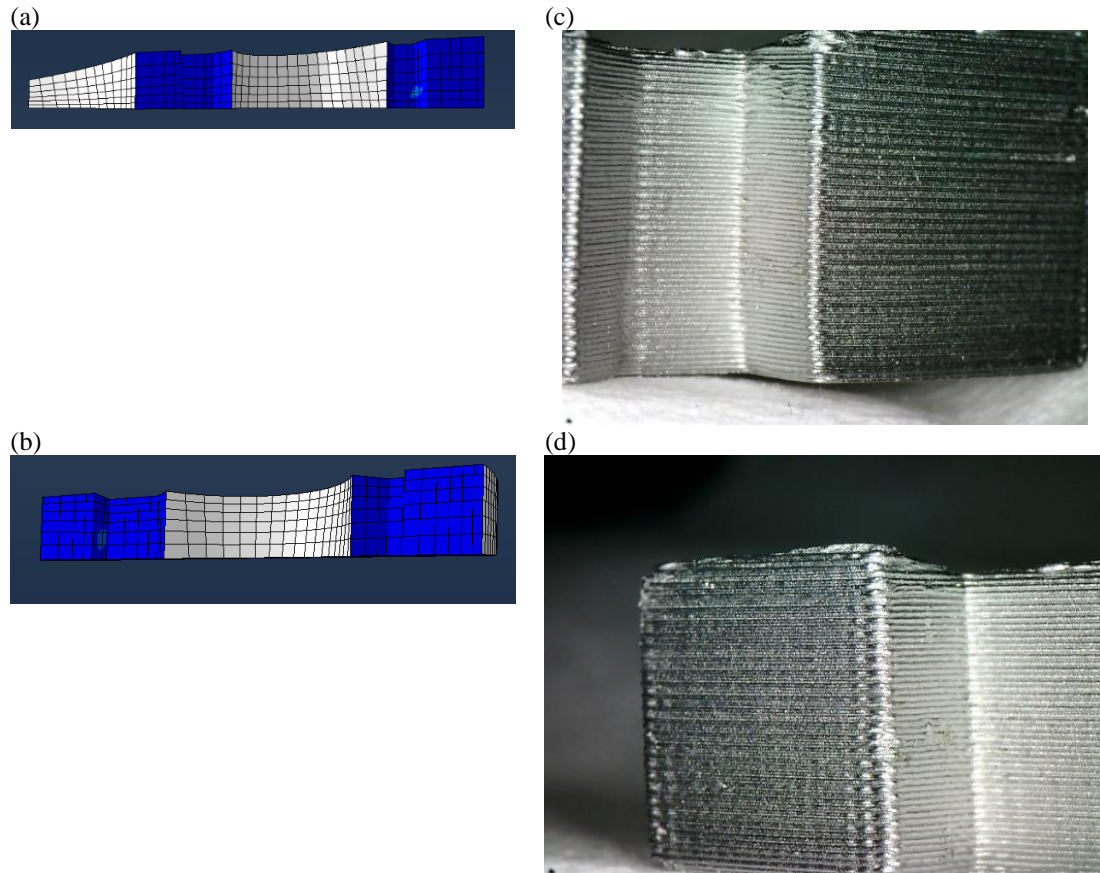


Figure 23 Contact stress of the exterior of the lateral component in two different views: (a) surfaces A, B, C, D, I, J, L (b) and surfaces A, C, D, E, J, K, L. The maximum contact stress in the lateral component is 2.00 Pa. Images of surfaces (c) A, B, C, and D and (d) J, K and L capture the regions where the highest contact stress points were found in the finite element model after 50,000 cycles.

**Figure 26** shows the contact stress patterns of the anterior component. The maximum contact stress in the anterior component was 3.96 Pa. Its highest stress concentration regions are on the F, G, R, and V surfaces, which directly interface the B and C surfaces of the lateral component, the X surface of the medial component and the AF surface of the posterior component. In the images of the implant after 50,000 loading cycles, wear scars are noticeable along the corner of the F and G surfaces, the top half of the R surface towards the Q surface, and in the top and bottom thirds of surface V.



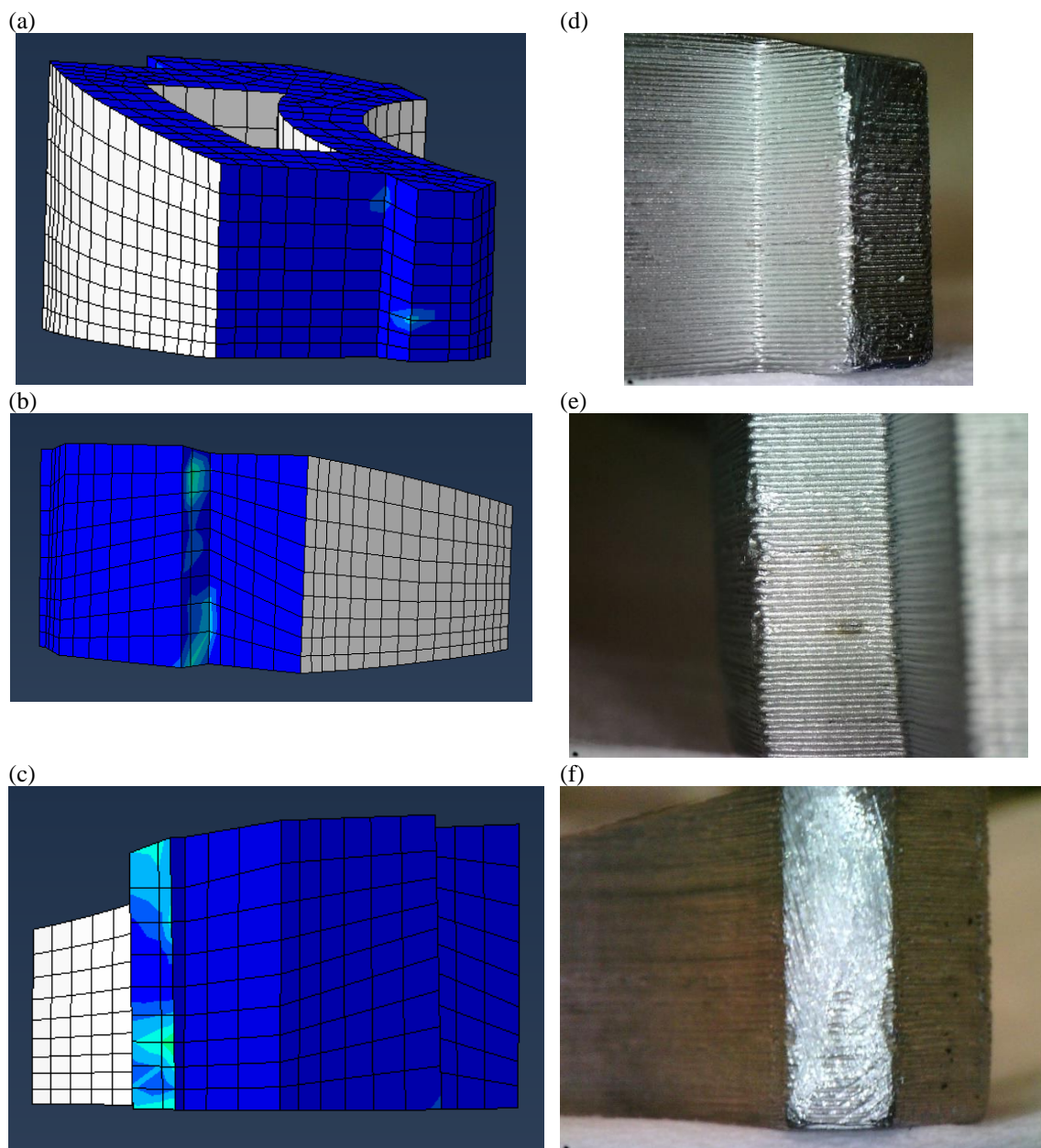


Figure 24 Contact stress of the exterior of the anterior component in three different views: (b) surfaces E, F, G, and H, (c) surfaces Q, R, S, V and U, and (d) surfaces S, V, U, and T. The maximum contact stress is anterior component is 3.96 Pa. Images of surfaces (d) E, F, and G, (e) Q, R, and S, and (f) T, U and V capture the regions where the highest contact stress points were found in the finite element model after 50,000 cycles.

**Figure 27** shows the posterior component of the implant. The maximum contact stress was found to be 7.41 Pa. Its highest stress concentration regions are on the N, O, AF and AJ surfaces, which directly interface the J and K surfaces of the lateral component, the V surface of the anterior component, and the AD surface of the medial



component. In the images of the implant after 50,000 loading cycles, wear scars are noticeable a third of the way up from the bottom on surface O toward surface N, the top left and bottom right quadrants of AF, and at the border of surface AJ closest to AI.

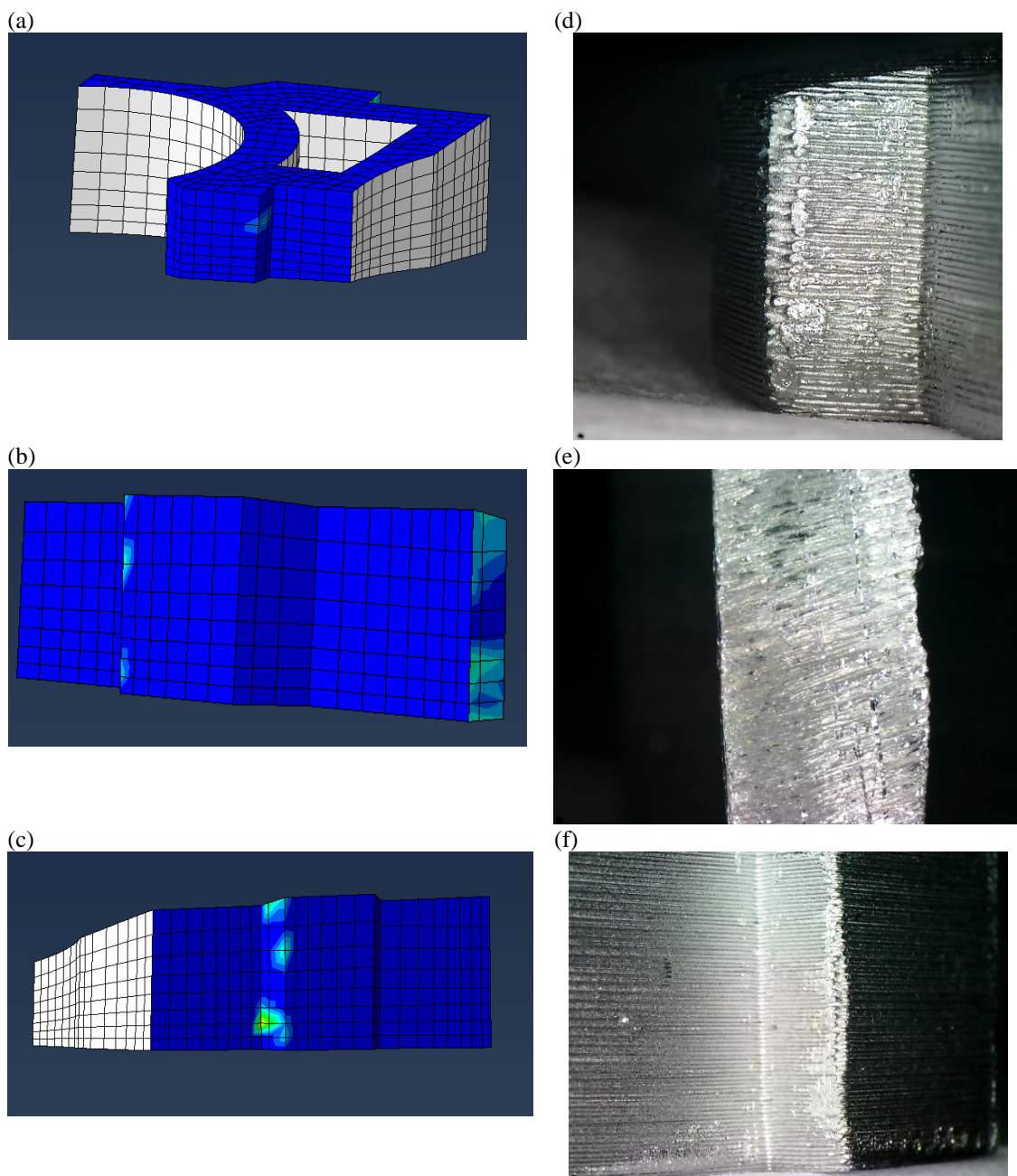


Figure 25 Contact stress of the exterior of the posterior component in three different views: (a) surfaces M, N, O, P, (b) AF, AG, AH, AI, AK, and (c) surfaces AG, AH, AI, AJ, AK. The maximum contact stress in the posterior component is 7.41 Pa. Images of surfaces (d) N, O, and P, (e) AF, and (f) AK, AJ, and AI capture the regions where the highest contact stress points were found in the finite element model after 50,000 cycles.

## CHAPTER 5: DISCUSSION & CONCLUSION

### 5.1 Component Weight Loss

Weighing components on an analytical balance before and after cyclic testing is a standardized technique, included in ASTM F1714-96 for measuring wear of polymeric components of prosthetic hip designs. In this study, this technique was used to confirm that the test fixture and test set up was valid for this stainless-steel multicomponent implant. The decreased mass observed in each component between pre- and post-test weighing indicates that the test fixture effectively subjected the implant components to wear. While this result was expected because the interfacing surfaces were observed during the test to be contacting each other, this quantitatively validates the test fixtures design for future studies based on a uniform standard.

This was initially confirmed by tests with a solid infill PLA implant, where particles were visible on a flat surface that lay beneath the implant in the test fixture. The masses of PLA implants before and after cyclic loading testing were not measured due to the concern that the PLA components would absorb water confounding any test related results.

The statistically significant decrease in mass between pre- and post-test measurements in the medial and lateral components signifies that the loss in mass is not likely to be caused by variation in a measuring device or technique. The medial component had the largest decrease in mass, but this was 210 mg, and was considered the minimum amount not to be necessary to be attributable to experimental variation. This

small-scale change in a high-density material like stainless steel material demonstrates that a more precise scale may be necessary for using gravimetric data to derive a wear rate for a less dense material like titanium alloy.

## **5.2 Optical Wear Patterns**

Observing wear scar patterns developing over a span of 50,000 loading cycles provided qualitative evidence of wear occurring at interfacing surfaces. The images of surface S of the anterior component show the progression of wear scars, which both expand and intensify over the progression of the test. Cycle dependent wear is evident, where the more cycles the implant is subjected to the more wear scars are evident.

The wear scars demonstrate the regions where there was the most sliding with an interfacing component and were caused by the loss of material. It can then be speculated from these images that the regions where the surface appears more reflective with lost definition of surface features was where material was lost due to wear mechanisms. In combination with measured weight loss, it is justified to claim that wear occurred between the components of this implant prototype at this location, which further supports the consideration of computational results in this region.

Observations of weight loss and macroscopic wear scars cannot provide information about the mechanisms of wear that are occurring. While the high magnification images from SEM before and after the cyclic loading testing could be taken of slightly different areas, they allow for comparison of microscopic changes to the surface. At 200x, there was more scratching on the corner between the F and G surfaces. This is characteristic of abrasive wear where one surface shears off particles from a weaker surface.

The 200x magnification image of the implant after 50,000 cycles also shows regions that appear to be more granular. This is indicative of a different kind of wear: adhesive wear or loss of sintered powder. This suggests that the two surfaces were under contact compression and that failure occurred within a weaker layer of the surface. Loss of sintered powder may be a type of poorly understood “wear” associated with the additive manufacturing process of sintered metal powder. Conceptually, incomplete, or poor sintering could prove a microstructure significantly more susceptible to loosening of particles from repetitive surface contact from cyclic loading. Again, the loss of sintered powder from surfaces of 3D printed sintered widgets is not yet well understood.

The potential wear caused by the loss of sintered powder puts the manufacturing process of the implant into question. 3D printing manufacturing of the implant could allow for patient customized implants, but it could impact the surface strength and wear rate. This means that not only is the geometry of the implant design important to study, but the manufacturing method is also important. A continuation of this study, perhaps pin-on-disk tests, could compare the results from a 3D printed implant prototype to an identical implant that was milled or pressed the way most commercially available implants are.

The SEM images do show some contamination from dirt or oils where there are darker regions on the implant surface. This is because the electron beam does not reflect and refract off dirt and oil as effectively as the stainless steel. These dark, dirt covered regions did not affect the qualitative observations made from the images about the wear patterns.

### 5.3 General Computational Results with Von Mises Stress

Von Mises stress accounts for the absolute value of all stresses. For example, typically compression is negative, and tension is positive, but a Mises stress description would show 5 MPa compression and 5 MPa tension as the same stress. This makes Mises stress helpful to understand the general magnitudes of stress. In the implant, the Mises stresses accounts yielding under complex loading mechanisms since its value comes from a combination of compression, tension, and shear stress. Generating these results was valuable because wear can occur under many mechanisms. The maps from the computational model indicated regions of interest at the highest stress regions, where type of stress was not a concern.

Stress corrosion and wear occurs when a crack forms due to tension or bending loads are applied to a material that is in a corrosive environment. This is an unlikely mechanism of wear in this test because the cracks would have been extremely small, and the environment was relatively inert because the implant was submerged in deionized water. Stress corrosion could happen at the microscopic level because the Mises map does indicate some regions that appear to be in bending. We expected this bending because the physical and computational models were loaded eccentrically to put the medial component into compression. The lateral component, opposite of the medial component would be in tension or offloaded since the bottom fixture was fixed. If small cracks formed due to the bending load, water could fill the crack and it would not flow in or out of the crack creating an ion gradient from oxygen depletion between the water inside and out of the crack. This could induce stress corrosion, but considering the testing

only took place over the span of several hours, it seems extremely unlikely that this would be a principal mechanism of wear in this model.

Stress corrosion could impact the implant in the long term when it is subjected to higher forces for a longer period. This would need to be evaluated in more physiologically relevant physical and computational models. It is assumed that by increasing the load and number of cycles, the resulting wear would increase linearly. If other types of wear, such as stress corrosion, account for more wear at higher loads and number of cycles, the relationship may not be as linear.

A deeper insight of the mechanics of the implant from the testing set up could be achieved by examining principal stresses and maximum shear stress in addition to von Mises stress because these stresses are more directly associated with the physical mechanisms of wear. Those could be compared to the physical evidence of wear to evaluate any potential connections. After this single study, there is not enough evidence to conclude what mechanisms were responsible for the wear. More iterations of testing would be required to be able to separate what forces are responsible for what wear.

#### **5.4 Wear Particles Collected Under Interfaces**

Measuring the weight of the samples collected in wells underneath the implant not only confirmed that wear processes were present, but showed evidence of particles coming off specific, identifiable interfaces of the implant. These particles could generate an immune response and disrupt the environment surrounding the implant.

An increase in weight of the water sampled indicated that there were wear particles present in the sample. The highest sample weight after 50,000 loading cycles were found around the medial component's interface with the anterior component. This

was also a region of high von Mises stress. Unfortunately, due to the order in which the implant was placed relative to the water added, not every well was able to be sampled. This meant the wells underneath highest region of stress at the interface of the medial and posterior components did not fill with water and were not sampled. It would be expected that the samples measured there would also be heavier than the DI water measured as a control and indicate a high number of wear particles.

In only one instance were sample weights found to be statistically significant from deionized water, which suggests the need to improve the sensitivity of this test procedure. Data saw that deionized water samples alone are likely to have an uncertainty of  $\pm 0.03$  g, so samples with concentration ratios of 1.05 and above were considered to correspond to real wear deposits.

This sensitivity of these measurements would be increasingly important if the implant prototype was made from titanium alloy, which is about half as dense as stainless steel. The same number or volume of wear particles would be even more difficult to measure. Using a denser metal for the proof of concept for this measurement regime was crucial in being able to detect wear particles and loss of mass in the components.

The shape and size of the wear particles collected in the wells underneath the implant could inform the knowledge of wear mechanisms as well. Techniques such as drying samples from the wells and observing under a high-power microscope or passing through a series of sieves could provide data necessary to characterize the geometry of the wear particles. The shape and size of a wear particle can play a large role in the immune response, not just the mass amount of foreign material.

## **5.5 Comparing Contact Pressure from Computational Model with Optical Wear Scar Patterns**

The regions of the highest contact pressure from the computational model are very small. Also, the interfacing surface pairs have mirrored contact pressure. For example, the surface X on the medial component has high contact stress regions and the surface R on the anterior component that interfaces with surface X also have high contact stress regions in a similar geometry.

There was some variation of where the wear scars were compared to where the high contact stress regions were. This could be because the fit of the implant is not as precise as the in the computational model. In that case, the difference in location indicates that the locations of where wear occurs is associated with the alignment of the interfacing features.

The highest contact stress regions were in the medial component on the same surfaces where the highest Mises stress regions were. This could indicate that a large proportion of the Mises stress is from contact stress at the high contact stress regions. The maximum magnitude of Mises stress in the medial component was 10.87 Pa at the corner of surfaces AD and AE and the maximum magnitude of contact stress in the medial component was 9.34 Pa at the same corner. This result, along with the physical evidence of wear at the high contact stress regions provides evidence that the wear in the implant is highly associated with contact stress. This observation suggests that modeling details, such as fillets or corners with radii may not be as important to include in computation wear studies as might first be conjectured.



## 5.5 Critique of Methods

A convergence test was performed for the mesh size of the implant on a computational model without eccentric loading or wells that were included in the modeling of the results and is included in **Appendix G**. The convergence test showed that a mesh with a global seed size of 1 would provide generally accurate results for the loading it was subjected to. This is satisfactory for a preliminary study. A very fine mesh would be required to evaluate the actual mechanisms of wear occurring.

The interactions at the interfaces were assigned as “penalty” with a coefficient of friction of 0.15 between stainless steel components and 0.3 between the stainless steel and PLA components. A more complete model would explore other types of interactions, such as overclosure, to simulate the bone ingrowth process into the superior and inferior surfaces of the implant.

Additionally, the computational model was only generated for one loading condition where the medial component was put in compression, where physiologically there are many relevant loading conditions to consider in the tibia. Future models could include torsion and tension.

The computational model was also run at a load that is a small fraction of a physiologic load. As mentioned in section 5.3, the effect load has on contact stress is nearly linear, but it would be necessary to generate a model with higher loads that more accurately approximate physiologic conditions before being able to make claims about the relationship between amounts of contact stress and physical wear measured.

The computational model did not account for the physiologically relevant materials such as cancellous and cortical bone as well as a titanium implant. These

improvements should be made to the model to increase its rigor in ability to correlate to physical wear.

The physical model and fixture were loaded in a single condition at a fraction of physiologic loading. Increasing the force and modeling different loading conditions would help to quantify and understand wear more accurately. The 1 mm displacement applied to the top of the fixture did not directly correspond to a 1 mm displacement of the implant. Factors including the fit of the fixture within the testing machine and a layer of artificial skin used to keep the implant from sliding out of the fixtures prevented the axial loading machine from loading the specimen identically to the computational model.

Physiologically relevant materials would increase the accuracy of the physically modeled results as well. Ideally this study could be performed with a titanium implant and cadaver tibia.

A closed chamber instead of an open basin would reduce potential contamination, especially when measuring sample weight from wells beneath the implant. That measurement could also be improved if the lubricating solution, such as bovine serum, was added before the implant so each well could be measured after the allotted number of cycles.

The lubricating fluid used in this study was DI water. The ASTM Standard Guide for measuring gravimetric wear testing of hip replacements used bovine serum with EDTA. That was shown in this study as not necessary to generate wear. A more biologically relevant lubricating fluid like saline or bovine serum would increase the sophistication of this model.

The test fixture was initially validated with solid infill PLA implant prototypes. This provided initial confirmation that the fixture produced the correct type of motion to hold the implant stable and collect wear particles. This was demonstrated by the appearance of blue PLA particles from the implant on a flat surface underneath the interfaces as well as wear scars on the interfacing surfaces of the PLA implant. Results from these preliminary tests are included in the appendix.

## **5.6 Conclusion**

The results from this preliminary study show promise for future work to understand orthopedic implant tribology and generate a relationship between computer modeled contact stress and physical wear. This is a topic that is infrequently studied because multicomponent implants are dismissed immediately due to the risk of corrosion and wear particles. An improved understanding of factors that affect wear would open new doors for orthopedic device development. If wear is shown to be minimal, the possibility for a multicomponent osteotomy wedge that would minimize the incision size needed. From an engineering perspective, this study demonstrates the need to have multiple methods to quantify wear experimentally. Developing a model that relates wear to contact pressure or von Mises stress based on experimental results will require broader and more rigorous studies. This thesis demonstrated that wear should be considered and that it can be related to computational models of stress.

## APPENDIX A: STANDARD GUIDE FOR GRAVIMETRIC WEAR ASSESSMENT OF PROSTHETIC HIP DESIGNS IN SIMULATOR DEVICES



Designation: F1714 - 96 (Reapproved 2018)

### Standard Guide for Gravimetric Wear Assessment of Prosthetic Hip Designs in Simulator Devices

This standard is issued under the fixed designation F 1714; the number immediately following the designation indicates the year of original adoption or, in the case of revision, the year of last revision. A number in parentheses indicates the year of last reapproval. A superscript epsilon ( $\epsilon$ ) indicates an editorial change since the last revision or reapproval.

#### 1. Scope

1.1 This guide describes a laboratory method using a weight-loss technique for evaluating the wear properties of materials or devices, or both, which are being considered for use as bearing surfaces of human-hip-joint replacement prostheses. The hip prostheses are evaluated in a device intended to simulate the tribological conditions encountered in the human hip joint, for example, use of a fluid such as bovine serum, or equivalent pseudosynovial fluid shown to simulate similar wear mechanisms and debris generation as found in vivo, and test frequencies of 1 Hz or less.

1.2 Since the hip simulator method permits the use of actual implant designs, materials, and physiological load/motion combinations, it can represent a more physiological simulation than basic wear-screening tests, such as pin-on-disk (see Practice F732) or ring-on-disk (see ISO 6474).

1.3 It is the intent of this guide to rank the combination of implant designs and materials with regard to material wear rates, under simulated physiological conditions. It must be recognized, however, that there are many possible variations in the in vivo conditions, a single laboratory simulation with a fixed set of parameters may not be universally representative.

1.4 The reference materials for the comparative evaluation of candidate materials, new devices, or components, or a combination thereof, shall be the wear rate of extruded or compression-molded, ultra-high molecular weight (UHMW) polyethylene (see Specification F648) bearing against standard counter faces [stainless steel (see Specification F 138); cobaltchromium-molybdenum alloy (see Specification F75); thermomechanically processed cobalt chrome (see Specification F799); alumina ceramic (see Specification F603)], having typical prosthetic quality, surface finish, and geometry similar to those with established clinical history. These reference materials will be tested under the same wear conditions as the candidate materials.

<sup>1</sup>This guide is under the jurisdiction of ASTM Committee F04 on Medical and Surgical Materials and Devices and is the direct responsibility of Subcommittee F04.22 on Arthroplasty.

Current edition approved April 1, 2018. Published May 2018. Originally approved in 1996. Last previous edition approved in 2013 as F1714 — 96 (2013). DOI: 10.1520/F1714-96R18.

1.5 The values stated in SI units are to be regarded as standard. No other units of measurement are included in this standard.

1.6 This international standard was developed in accordance with internationally recognized principles on standardization established in the Decision on Principles for the Development of International Standards, Guides and Recommendations issued by the World

Copyright © ASTM International, 100 Barr Harbor Drive, PO Box C700, West Conshohocken, PA 19428-2959, United States

Trade Organization Technical Barriers to Trade (TBT) Committee.

## 2. Referenced Documents

### 2.1 ASTM Standards..2

D883 Terminology Relating to Plastics  
F75 Specification for Cobalt-28 Chromium-6 Molybdenum Alloy Castings and Casting Alloy for Surgical Implants (UNS R30075)

F86 Practice for Surface Preparation and Marking of Metallic Surgical Implants

F136 Specification for Wrought Titanium-6Aluminum4Vanadium ELI (Extra Low Interstitial) Alloy for Surgical Implant Applications (UNS R564(0))

F138 Specification for Wrought 18Chromium-14Nickel2.5Molybdenum Stainless Steel Bar and Wire for Surgical Implants (UNS S31673)

F370 Specification for Proximal Femoral Endoprosthesis (Withdrawn 2005) <sup>3</sup>

F565 Practice for Care and Handling of Orthopedic Implants and Instruments

F603 Specification for High-Purity Dense Aluminum Oxide for Medical Application

F648 Specification for Ultra-High-Molecular-Weight Polyethylene Powder and Fabricated Form for Surgical Implants

F732 Test Method for Wear Testing of Polymeric Materials

Used in Total Joint Prostheses

For referenced ASTM standards, visit the ASTM website, [www.astm.org](http://www.astm.org), or contact

ASTM Customer Service at [service@astm.org](mailto:service@astm.org). For Annual Book of ASTM Standards volume information, refer to the standard's Document Summary page on the ASTM website.

The last approved version of this historical standard is referenced on [www.astm.org](http://www.astm.org).

F799 Specification for Cobalt-28Chromium-6Molybdenum Alloy Forgings for Surgical Implants (UNS R31537, R31538, R31539)

G40 Terminology Relating to Wear and Erosion

### 2.2 ISO Standard:

ISO 6474 Implants for Surgery—Ceramic Materials Based on Alumina<sup>1</sup>

#### Significance and Use

This guide uses a weight-loss method of wear determination for the polymeric components used with hip joint prostheses, using serum or demonstrated equivalent fluid for lubrication, and running under a dynamic load profile representative of the human hip-joint forces during walking (1,2). <sup>2</sup>The basis for this weight-loss method for wear measurement was originally developed (3) for pin-on-disk wear studies (see Practice F732) and has been extended to total hip replacements (4,5) femoral-tibial knee prostheses (6), and to femoropatellar knee prostheses (6,7).

While wear results in a change in the physical dimensions of the specimen, it is distinct from dimensional changes due to creep or plastic deformation, in that wear generally results in the removal of material in the form of polymeric debris particles, causing a loss in weight of the specimen.

<sup>1</sup> Available from American National Standards Institute (ANSI), 25 W. 43rd St., 4th Floor, New York, NY 10036, <http://www.ansi.org>.

<sup>2</sup> The boldface numbers in parentheses refer to the list of references at the end of this standard.

This guide for measuring wear of the polymeric component is suitable for various simulator devices. These techniques can be used with metal, ceramic, carbon, polymeric, and composite counter faces bearing against a polymeric material (for example, polyethylene, polyacetal, and so forth). This weight-loss method, therefore, has universal application for wear studies of total hip replacements that feature polymeric bearings. This weight-loss method has not been validated for high-density material bearing systems, such as metal-metal, carbon-carbon, or ceramic-ceramic. Progressive wear of such rigid bearing combinations generally has been monitored using a linear, variable-displacement transducers or by other profilometric techniques.

#### 4. Apparatus and Materials

4.1 Hip Prosthesis Components—The hip-joint prosthesis comprises a ball-and-socket configuration in which materials such as polymers, composites, metal alloys, ceramics, and carbon have been used in various combinations and designs.

4.2 Component Configurations—The diameter of the prosthetic ball may vary from 22 to 54 mm or larger. The design may include ball-socket, trunnion, bipolar, or other configurations.

#### 4.3 Hip Simulator:

4.3.1 Test Chambers—In the case of a multi-specimen machine, contain the components in individual, isolated chambers to prevent contamination of one set of components with debris from another test. Ensure that the chamber is made entirely of noncorrosive materials, such as acrylic plastic or stainless steel, and is easily removable from the machine for thorough cleaning between tests. Design the wear chambers such that the test bearing surfaces are immersed in the lubricant throughout the test (3,7).

4.3.2 Component Clamping Fixtures—Since wear is to be determined from the weight-loss of the components, the method for mounting the components in the test chamber should not compromise the accuracy of assessment of the weight-loss due to wear.

4.3.3 Load—Ensure that the test load profile is representative of that which occurs during the patient's walking cycle, with peak hip-loads 22 kN (2). The loading apparatus shall be free to follow the specimen as wear occurs, so that the applied load is constant to within  $\pm 3\%$  for the duration of the test. Never allow the applied load to be below that required to keep the chambers seated (for example, 50 N) (4).

4.3.4 Motion—Ensure that relative motion between the hip components oscillates and simulates the flexion-extension arc of walking. Addition of internal-external or abduction-adduction arcs is at the investigator's discretion. It is recommended that the orientations of the cup and ball relative to each other and to the load-axis be maintained by suitable specimenholder keying.

4.3.5 Oscillating Frequency—Oscillate the hip prostheses at a rate of one cycle per second (1 Hz).

4.3.6 Cycle Counter—Include a counter with the hipsimulator to record the total number of wear cycles.

4.3.7 Friction—It is recommended that the machine include sensors capable of monitoring the friction forces transmitted across the bearing surfaces during the wear test.

#### 4.4 Lubricant:

4.4.1 It is recommended that the specimen be lubricated with bovine blood serum; however, another suitable lubrication medium may be used if validated.

4.4.2 If serum is used, use filtered-sterilized serum rather than pooled serum

since the former is less likely to contain hemolyzed blood material, which has been shown to adversely affect the lubricating properties of the serum (3). Diluted solutions of serum have also been used for this purpose (8). Filtration may remove hard, abrasive, particulate contaminants that might otherwise affect the wear properties of the specimens being tested.

4.4.3 Maintain the volume and concentration of the lubricant nearly constant throughout the test. This may be accomplished by sealing the chambers so that water does not evaporate, or periodically or continuously replacing evaporated water with distilled water.

4.4.4 To retard bacterial degradation, freeze and store the serum until needed for the test. In addition, ensure that the fluid medium in the test contains 0.2 % sodium azide (or other suitable antibiotic) to minimize bacterial degradation. Other lubricants should be evaluated to determine appropriate storage conditions.

4.4.5 It is recommended that ethylenediaminetetraacetic acid (EDTA) be added to the serum at a concentration of 20 mM to bind calcium in solution and minimize precipitation of calcium phosphate onto the bearing surfaces. The latter event has been shown to strongly affect the friction and wear properties, particularly of polyethylene/ceramic combinations. The addition of EDTA to other lubricant mediums should be evaluated.

4.4.6 A lubricant other than bovine serum may be used if it can be shown that its lubricating properties and, therefore, material wear properties are reasonably physiological (8). In such a case, specify the lubricant in the test report.

4.5 Hold the bulk temperature of the lubricant at  $37 \pm 3$  °C or as specified, if different.

## 5. Specimen Preparation

5.1 The governing rule for preparation of component counter faces is that the fabrication process parallels that used or intended for use in the production of actual prostheses, in order to produce a specimen with comparable bulk material properties and surface characteristics (see Practice F86).

### 5.2 Polymers and Composites:

5.2.1 Obtain a fabrication history for each polymeric or composite component, including information such as grade, batch number, and processing variables, including method of forming (extruding, molding, and so forth), temperature, pressure, and forming time used, and any post-forming treatments, including sterilization.

5.2.2 Pretest characterization may include measurement of bulk material properties, such as molecular-weight range and distribution, percent crystallinity, density, or other. The surface finish of specimens may be characterized by profilometry, photomicrography, replication by various plastics, or other techniques.

5.2.3 Sterilization—Sterilize the components in a manner typical of that in clinical use for such devices, including total dose and dose rate, as these may affect the wear properties of the materials. Report these processing parameters with the aging time prior to each test when known. Sterilization of all test and control components within a specific test group should be done simultaneously (in a single container), when possible, to minimize variation among the specimens. This wearsimulation procedure makes no attempt to maintain the sterility of specimens during the wear test.

5.2.4 Cleaning of Polymer Prostheses—Prior to wear testing, careful cleaning of the polymer specimens is important to remove any contaminants that would not normally be present on the actual

prosthesis. During the wear run, the components must be re-cleaned and dried before each weighing to remove any extraneous material that might affect the accuracy of the weighing. A suggested procedure for cleaning and drying of polymeric components is given in Annex A4. With some combinations of materials, wear may result in the transfer of particulate debris which may then become reembedded or otherwise attached to polymeric, metal, or composite surfaces. Such an occurrence will render the weight-loss assessment of wear less reliable.

#### 5.2.5 Weighing of Polymeric

Components—Weigh the polymeric components on an analytical balance having an accuracy on the order of  $\pm 10$   $\mu$ g. This degree of sensitivity is necessary to detect the slight loss in weight of polymers, such as UHMW polyethylene, which may wear 30 mg or less per million cycles (3,5). Always weigh specimens in the clean, dry condition (see Annex A1). Keep the components in a dust-free container and handle with clean tools to prevent contamination that might affect the weight measurement. Weigh each wear and control component three times in rotation to detect random errors in the weighing process.

#### 5.3 Soaking of Polymeric and Composite Prostheses:

5.3.1 Polymeric and composite components should be presoaked in the lubricant to minimize fluid sorption during the wear run. Without presoaking, components of very low-wear polymers such as polyethylene may show a net increase in weight during the initial wear intervals, due to fluid sorption (3,4). The error due to fluid sorption can be reduced through presoaking and the use of control soak specimens. The number of specimens required and the length of presoaking

depends on the variability and magnitude of fluid sorption encountered (4).

5.3.2 After fabrication and characterization, clean and dry the wear components and three soak-control components of each test material in accordance with Annex A4, and then weigh by precisely controlled and repeatable methods. Place the wear components and soak controls in a container of serum for a specified time interval. Then, remove, clean, dry, and reweigh the components, and calculate the weight-loss (see Annex A4). Repeat the specimens until a steady rate of fluid-sorption has been established. The number of weighings will depend on the amount of fluid sorption exhibited by the specimens.

5.3.3 In general, the weight of the components will stabilize at an asymptotic value in a reasonable time period. With UHMW polyethylene, a presoak period of 30 days has been found adequate (4,7). In any case, use the weight-gain of the soak controls to correct for ongoing fluid sorption by the wear components during the wear test.

#### 5.4 Counterfaces of Metal Alloys, Ceramic, or Other Materials:

5.4.1 Characterization—Include with the pretest characterization of metal, ceramic, or other materials, recording of fabrication variables, such as composition, forming method (forging, casting, and so forth) and any postforming processing, such as annealing. Obtain data on material properties relevant to wear (for example, grain structure, hardness, and percentage of contaminants).

5.4.2 Surface Finish—In tests that are intended to evaluate an alternate counter face material bearing against the standard UHMWPE, ensure that the counter face finish is appropriate for components intended for clinical use. In tests of alternate materials where a reference metal



or ceramic is used, polish the counter face to the prosthesis quality.

5.4.3 Clean, degrease, and passivate components of referenced prosthetic metals or ceramics in accordance with Practice F86. This practice may require modification for components of other materials. Ensure that cleaning of components produces a surface free of any particles, oils, greases, or other contaminants that might influence the wear process.

## 6. Measurement Procedure

6.1 At the completion of the presoak period, the wear components and soak controls should be removed from the soak bath, cleaned, dried, and weighed by precisely controlled and repeatable methods. Record these weights as the initial weights of the specimens for purposes of calculating the progressive weight-loss during the wear test. Place the three soak control specimens in holders in a soak chamber of test lubricant, such that the total surface area exposed to the lubricant is equal to that of the wear components when mounted in the hip simulator. Maintain the soak chamber temperature at  $37 \pm 3$  °C, or specify if different. It is recommended that the soak chamber be attached to the simulator or otherwise agitated in the same manner as the actual wear chambers. In addition, it may be advantageous to apply a cyclic load to the soak control specimens (without tangential motion) comparable to that applied to the wear specimens, since this can also affect the rate of fluid sorption.

6.2 Frictional torque should be recorded for each specimen combination. This may be done in a preliminary test under a constant (static) load, or during the wear test under the cyclic, physiological load. These measurements may be repeated at various intervals during the wear test to

determine changes in frictional properties with progressive wear.

6.3 Place the wear test components in the hip simulator, add the lubricant, apply the load, and commence the cyclic motion.

Record the frictional force simultaneously with the wear cycling, where applicable.

6.4 Matching of components in each test set may be desirable to ensure optimum consistency of wear performance during these tests.

6.5 As testing is commenced, monitor the components for signs of erratic behavior that might require an early termination of the test.

6.6 Remove the wear and soak components at specified intervals, then wash, rinse, and dry, in accordance with the procedure in Annex A4. It is important that both the wear and soak components be treated identically to ensure that they have the same exposure to the wash, rinse, and drying fluids. This will provide the most accurate correction for fluid sorption by the wear specimens.

6.7 After rinsing and drying, weigh the wear components and soak controls on the analytical balance as described in 5.2.5.

6.8 Thoroughly rinse the wear chambers and component surfaces with distilled water.

6.9 Inspect the bearing surfaces of the hip components and note the characteristics of the wear process. Visual, microscopic, profilometric, replication, or other inspection techniques can be used. Care must be taken, however, that the surfaces do not become contaminated or damaged by any substance or technique that might affect the subsequent wear properties. If contamination occurs, thoroughly reclean the specimens prior to restarting the wear test.

6.10 Replace the wear components, soak controls in fresh lubricant, and continue wear cycling.

## 7. Determining Wear Rates

7.1 Test Length—The accuracy of the test method depends on the relative magnitudes of wear and fluid sorption.

This is especially true when the fluctuations in the weight due to variation in the amount of surface drying are large in comparison to the incremental weight-loss due to wear. For high-wear low-sorption materials, the wear rate may be established clearly in as few as 50 000 wear cycles. With comparatively low-wearing materials, such as UHMWPE, several million cycles or more may be required to clearly establish the long-term wear properties.

7.2 Number of Replicate Tests—Perform tests intended to determine the relative wear rates of two materials with at least three sets of specimens for each material to provide an indication of the repeatability of the results. As for any such experimental comparison, the total number of specimens eventually needed will depend on the magnitude of the difference to be established, the repeatability of the results (standard deviation), and the level of statistical significance desired.

7.3 Correcting for Fluid Sorption—Add to or subtract from the average weight-gain (or loss) of the three soak control components the measured weight-loss of each wear component (see Annex A6).

This procedure corrects both for systematic sorption, as well as random differences in the amount of surface drying (of the entire set of test and control specimens) at each interval of weighing.

7.4 Conversion to Volumetric Wear—In tests where the wear rates of materials with different densities are evaluated, it may be preferable to compare these on the basis of volumetric wear, rather than weight-loss. It is preferable that comparisons of the wear properties between components of polymeric

materials having different densities be done on the basis of volumetric wear. The volumetric wear rate may be obtained by dividing the weight-loss data by the density of the material, in appropriate units. The accuracy of this calculation depends on the material being reasonably homogeneous, that is, having a constant density with wear depth. Report the density value used in this conversion.

## 8. Report

### 8.1 Materials:

8.1.1 Provide material traceability information from a raw material and fabrication or manufacturing standpoint for each material counter face. Examples of such information include material grade, batch number, and processing variables.

8.1.2 Pretest characterization for a plastic counter face may include measurement of bulk material properties, such as molecular-weight average, range and distribution, percent crystallinity, density, degree of oxidation, or others. The surface finish of both counter faces may be characterized by profilometry, photomicrography, replication, or other applicable techniques.

8.1.3 Report the method of sterilization, the sterilization and test dates, and the means of storage post-sterilization and pretest.

8.2 Loading Conditions—Describe the loading conditions used on the specimens. Report load curves and motions and timing relationships.

### 8.3 Wear Rates:

8.3.1 Graphically plot the weight-loss of each specimen as a function of wear cycles. Wear may be reported as the weightloss of the bearing component as a function of the number of wear cycles, but it also may be converted to volumetric wear if the density of the material is known.

8.3.2 In tests where the wear rate is nearly constant over the test run, calculate the volumetric wear rate by the method of least squares in each regression.

8.3.3 If the wear rate changes during the test, as with a decrease due to wearing-in of the specimens or an increase due to the onset of fatigue wear, linear regression may be applied to separate intervals of the test to indicate the change in wear rate.

8.3.4 At the discretion of the investigator, more complex, nonlinear models may be fitted to the wear-test data.

8.3.5 Report the test duration in cycles.

8.4 Accuracy and Repeatability:

8.4.1 In multiple tests where the wear rate is determined from the slope of the graph comparing wear versus test duration (cycles) for each specimen, report the individual rates, mean wear rate, and the 95 % confidence intervals for each rate.

## ANNEXES

(Mandatory Information)

### A1. CHOICE OF WEAR-TEST LUBRICANT

8.4.2 In cases where the mean wear rate for two materials is different, evaluate and report the level of statistical significance of this difference.

8.5 Since the accumulation of wear debris in the lubricant may influence the wear

A1.1 Comparative experiments have shown that distilled water or saline solutions do not duplicate the lubricating properties of fluids such as serum or synovial fluid that contain physiological concentrations of proteins (1,3). In particular, the heavy transfer of polyethylene to the surface of metal or

rate, report any filtering of the lubricant during operation (continuously or periodically).

8.6 Record and report the room temperature and humidity during each weighing session.

8.7 Report the loading conditions on the soak control specimens. Load soaking, which is defined as a pulsing load profile equivalent to the wear profile without the tangential movement, has been shown to increase the fluid sorption rate.

8.8 In order that the simulator wear data be reproducible and comparable among laboratories, it is essential that uniform procedures be established. Sufficient data have not yet been produced using identical materials in different laboratories to permit determination of the precision and bias of this recommended procedure. This guide is intended, in part, to facilitate uniform

testing and reporting of data from hip joint simulator wear studies. It is anticipated that the references provided will permit validation of this methodology.

typical of serum-lubricated specimens and is not typical of retrieved components after extended in vivo use. Care must be taken in the choice of lubricant to ensure that when used in simulated hip wear tests, it approximates the wear found clinically. Therefore, the choice of lubricant along with the validation for its use should be

A2. IMPLANT MATCHING FOR CONSISTENT WEAR PERFORMANCE  
ceramic implant that is typically observed with water or saline lubrication, is not

A2.1 The optimal clearance between the ball and socket of total hip prostheses is a matter of controversy with regard to its affect on the friction and wear properties,

reported.

and this will vary for different combinations of materials and different designs of prostheses (5,7,9). It may be desirable to calculate the effects of design

and installation procedures on frictional forces across the material components prior to performing an extended wear study.

A4.7 Dry in a vacuum jar at a minimum vacuum of 10-3torr for 30 min.

A4.8 Weigh on a microbalance.

A4.9 To minimize weighing errors, weigh

### A3. PRECAUTIONS IN PREPARING SPECIMEN SURFACES

A3.1 Do not polish or otherwise attempt to improve the polymer surfaces with abrasives, for example, aluminum oxide. Particles of the polishing compound may remain embedded in the polymeric material and could strongly affect the wear performance of the bearing materials.

### A4. METHOD FOR CLEANING OF SPECIMENS

A4.1 Gently scrub cups with a nonabrasive material to remove all serum particles.

Verify under a magnifying glass.

A4.2 Rinse under a stream of deionized water.

A4.3 Clean in an ultrasonic cleaner:

A4.3.1 Five minutes in deionized, particle-free water.

A4.3.2 Rinse in deionized water.

A4.3.3 Ten minutes in 10 mL of liquid ultrasonic cleaning detergent plus 500 mL of water.

A4.3.4 Rinse in deionized water.

A4.3.5 Ten minutes in deionized water.

A4.3.6 Rinse in deionized water.

A4.3.7 Three minutes in deionized water.

A4.3.8 Rinse in deionized water.

### A5. COMPONENT CLAMPING FIXTURES

A4.4 Dry with a jet of nitrogen or other suitable clean, dry gas.

A4.5 Soak in 95 % methyl alcohol for 5 min.

A4.6 Dry with a jet of nitrogen or other suitable gas.

A5.1 One technique that has proven practical has been to clamp each component in a mold (for example, polyurethane) that replicates the outer shape of the test component. The mounting mold is then press-fit into the stainless steel base of each chamber (7). The mounting method should permit the

the entire set of specimens three times, in rotation, keeping the same specimen sequence each time. Polymeric cups typically gain or lose weight slightly between each weighing due to additional sorption or evaporation of fluid. The average of the three weights may be used for the wear calculations.

NOTE A4. I—This is a suggested cleaning procedure suitable for metals, ceramics, carbon, and UHMW polyethylene (3). Use methyl alcohol only for polymers that are essentially insoluble in this liquid. For polymers that dissolve or degrade in methyl alcohol, substitute a more appropriate volatile solvent. The purpose of this step is to remove the water that

otherwise tends to evaporate from the surface layer of the specimen during the weighing process. Other aspects of this procedure might require modification for the particular polymer being tested.

test components to be removed periodically for cleaning and weighing without damaging the test components or causing a separate loss of weight of the test components. If there is doubt, it is recommended that several specimens be mounted and removed from the machine several times each and weighted each time

to detect any weight change caused by the mounting procedure.

#### A6. CALCULATION OF SPECIMEN WEAR

A6.1 The amount of fluid sorption over a wear interval is determined from the three soak controls, whereby the average weight-gain,  $S_n$ , is calculated as follows:

$$s_n = 1/3 (S_a + S_b + S_c) \quad (A6.1)$$

A6.2 Since fluid sorption by the wear specimens tends to mask the actual weight loss due to wear, increase the magnitude of the measured weight loss by the wear specimens by the magnitude of the weight-gain of the soak specimens; where,  $S_1$  equals initial average weight of the three soak specimens and  $S_2$  equals the final average weight of the three soak specimens. A6.3 The actual net wear, then, is given as follows:

$$W_2 = W_1 - W_3 \quad (A6.2)$$

A6.3.1 However,  $W_3$  is unknown. On the other hand, the apparent wear is given as follows:

(A6.3)

where:

$W_1$

= initial weight of the wear specimen,  
 $W_2$  = final weight of the wear specimen (including a gain due to fluid sorption),  
 and

X 1.1 The hip simulator wear studies of materials may involve three types of evaluation:

X1.1.1 Comparing the wear rate of a candidate polymeric material to that of polyethylene, both bearing against one of the reference metal or ceramic counter faces.

X1.1.2 Comparing the polyethylene wear on the candidate counter face material to that of polyethylene wear on the reference metal or ceramic component.

$W_3$  = the actual final weight of the wear specimen if fluid sorption is subtracted

out.

A6.3.2 The actual net wear ( $W_n$ ) can be obtained by increasing the apparent wear ( $W_a$ ) by an amount equal to the net soak gain.

$$W_n = W_a + S_n; \text{ Where } S_n = S_2 - S_1 \quad (A 6.4)$$

$$\text{Thus } w_n = (W_1 - \quad - S_0) \quad (A6.5)$$

A6.4 Note that the four weights  $W_1$ ,  $W_2$ ,  $S_1$ , and  $S_2$  are actual measured values. The sign convention in this equation for  $W_n$  takes into account occurrences, such as an apparent weight-gain by the wear specimen (giving a negative value for  $W_a$ ) or a net weight-loss by the soak specimens (a negative value of  $S_n$ ). In most cases the net wear,  $W_n$ , will be zero or positive.

A6.5 The net volumetric wear is then given as follows:

$$V_n = w_n/p \quad (A6.6) \text{ where:}$$

$P$  = density of the polymer, expressed in

#### APPENDIX

(Nonmandatory Information) XI.

#### RATIONALE

appropriate units.

X 1. 1.3 Comparing the wear rate of a new combination of candidate materials to the reference combinations.

X 1.2 For the purpose of this guide, wear is defined as the progressive loss of material from a prosthetic component as a result of tangential motion against its mating component under load. For current designs of total hip prostheses, used since 1971 in the United States, the polymeric component bearing against metal, ceramic, composite, or carbon balls will be the sacrificial member, that is, the polymer

will be the predominant source of wear debris. The metallic or other non-polymeric components, however, also may contribute either ionic or particulate debris. Depending on circumstances, therefore, wear may be generated by adhesion, two or three body abrasion, surface or subsurface fatigue, or some other process. Depending on the candidate materials and design combinations selected, it may be desirable in some instances to add additional techniques to identify the nature and magnitude of the wear process.

X 1.3 While wear results in a change in the physical dimensions of the specimen, it is distinct from dimensional changes due to creep or plastic deformation in that wear generally results in the removal of material in the form of debris particles, causing a loss in weight of the specimen (3, 7).

X 1.4 Wear rate is the gravimetric or volumetric wear per million cycles of test.

X1.5 During wear testing in serum, calcium phosphate may precipitate on the surface of the test balls, particularly those of ceramic, and strongly affect the friction and wear properties. The addition of 20 mM EDTA in the lubricant may eliminate such precipitation.

#### REFERENCES

Davy, D. T., Kotzar, G. M., Brown, R. H., Heiple, K. G., Goldberg, V.

M., et al, "Telemetric Force Measurement Across the Hip After Total vol 70A(1), No. 45, 1988.

Paul, J. P., "Forces Transmitted by Joints in the Human Body.

Lubrication and Wear in Living and Artificial Human Joints," Proc. Instn. Mech. Engrs. Vol 181 (3J), No. 8, London 1966/67.

McKellop, H. A., Clarke, I. C., Markolf, K., and Amstutz, H. C., "Wear Characteristics of UHMW Polyethylene:

A Method for Accurately Measuring Extremely Low Wear Rates," J. Biomed. Mat. Res., Vol 12, No. 895, 1978.

Clarke, I. C., Starkebaum, W., Hosseinian, A., McGuire, P., Okuda, R., Salovey, R., and Young, R. "Fluid-Sorption Phenomena in Sterilized Polyethylene Acetabular Prostheses," J. Biomat., Vol 6, No 184, 1985.

McKellop, H. A., Lu, B., and Benya, P., "Friction, Lubrication and Wear of Cobalt-Chromium, Alumina and Zirconia Hip Prostheses Compared on a Joint Simulator," Trans. Orthop. Res. Soc., 1992, p. 401.

Trehan, R. W., Young, R. W., and Young, S. R., "Wear of Artificial Joint Materials III: Simulation of the Knee Joint Using a Computer Controlled System," Engineering in Medicine, Vol 10, No. 3, 1981, pp. 137-142.

McKellop, H. A., and Clarke, I. C., "Degradation and Wear of Ultra-High-Molecular-Weight Polyethylene," ASTM Special Technical Publication 859, ASTM, 1985 .

Streicher, R. M., "Ceramic Surfaces as Wear Partners for Polyethylene." Bioceramics, Vol 4, p. 9, W. Bonfield, G. W. Hastings, K. E.

Tanner, eds., Butterworth-Heinemann Ltd., London, 1991.

Rae, T., "Comparative Laboratory Studies on the Production of Soluble and Particulate Metal by Total Joint Prostheses," Arch. Orthop. Traumat. surg., Vol 95, No. 71, 1979.

ASTM International takes no position respecting the validity of any patent rights asserted in connection with any item mentioned in this standard. Users of this standard are expressly advised that determination of the validity of any such patent rights, and the risk of infringement of such rights, are entirely their own responsibility.

This standard is subject to revision at any time by the responsible technical committee and must be reviewed every five years and if not revised, either reapproved or withdrawn. Your comments are invited either for revision of this standard or for additional standards and should be addressed to ASTM International Headquarters. Your comments will receive careful consideration at a meeting of the responsible technical committee, which you may attend. If you feel that your

comments have not received a fair hearing you should make your views known to the ASTM Committee on Standards, at the address shown below. This standard is copyrighted by ASTM International, 100 Barr Harbor Drive, PO Box C700, West Conshohocken, PA 19428-2959, United States. Individual reprints (single or multiple copies) of this standard may be obtained by contacting ASTM at the above address or at 610-832-9585 (phone), 610-832-9555 (fax), or [service@astm.org](mailto:service@astm.org) (e-mail); or through the ASTM website ([www.astm.org](http://www.astm.org)). Permission rights to photocopy the standard may also be secured from the Copyright Clearance Center, 222 Rosewood Drive, Danvers, MA 01923, Tel. • (978) 646-2600; <http://www.copyright.com/>

## **APPENDIX B: A MULTI-COMPONENT IMPLANT FOR USE IN TIBIAL OSTEOTOMY TO CORRECT VARUS DEFORMITY IN THE MORBIDLY OBESE**

### **A MULTI-COMPONENT IMPLANT FOR USE IN TIBIAL OSTEOTOMY TO CORRECT VARUS DEFORMITY IN THE MORBIDLY OBESE**

Derek M. Spillane, Chandler S. Harris, Maeve C. Junker, Ana E. Figel, Madeline G. Tallman, Sarah R.

Kinney, Ronald C. Anderson, Uwe R. Pontius

Tulane University, Department of Biomedical Engineering, New Orleans, LA

#### **ABSTRACT**

Valgus tibial osteotomy (VTO) offers an alternative to total knee arthroplasty (TKA) for patients with varus knee deformity. This report describes a novel, modular implant intended to occupy the wedge osteotomy space via a small medial incision to reduce surgical complications associated with patients having a BMI of 40 or greater (morbidly obese). The wedged-shaped, 3-D laser-sintered titanium alloy implant consists of interlocked components to be assembled *in situ*. Components were fabricated with a continuous laser-sintered surface lattice structure for bone ingrowth. The sliding resistance of a range of geometrically scaled lattices was assessed to determine the optimal lattice structure for initial implantation. The lattice structure had a 550  $\mu$ m surface opening (150  $\mu$ m internal pore size). Finite element models were created to evaluate three VTO scenarios including a medial restraining T-plate and implant combination, a T-plate alone as commonly seen clinically, and a model of only the implant within the osteotomy. Axially loaded models revealed implant stresses to be well below titanium fatigue strength, but the model of the T-plate alone indicated large plate and screw stresses comparable to the fatigue strength. Investigations are ongoing to assess multifunctional loading and experimental strain measurement. These results suggest this modular implant design may provide BMI > 40 patients an effective treatment option to early TKA.

**Keywords:** BMI, obesity, varus deformity, tibial osteotomy, modular implant, bone ingrowth, lattice, finite element model

#### **INTRODUCTION**

Valgus tibial osteotomy (VTO) offers an alternative to total knee arthroplasty (TKA) for patients with varus knee deformity due to medial compartment cartilage degeneration, trauma, or osteoarthritis [1,2]. In the morbidly obese patient (BMI > 40) with a likelihood of co-morbidity, the increased incidence of surgical complications associated with TKA has generated interest in VTO as an alternative treatment, particularly in the younger obese patient [2,3,4]. However, the current procedures for VTO in non-obese patients (BMI < 30) are poorly suited for patients with BMI > 40 because of the extreme stresses generated on an implant designed for this type of deformity correction [5,6,7]. Commonly, the VTO requires a plate and/or screws placed across the medial wedge opening to stabilize the site and shunt the load around the osteotomy while the grafted or un-grafted bone heals. This paper describes a novel, multi-component, osseo-integrative implant that can be implanted through a minimal incision, then assembled within the



osteotomy space, thereby reducing the risk of wound infection associated with the obese patient. Further, by filling the osteotomy with this multi-component implant, fixed by bone ingrowth, early full weight-bearing may be achieved to facilitate the recovery of morbidly obese patients. If warranted, this implant also accommodates a future conversion to TKA without need for device removal.

## METHODS

Figure 1A shows the geometric model of an implanted VTO used as the basis for the analyses reported in this paper. It consists of a proximal tibia, cortical and cancellous bone regions found via CT/DICOM images (Osirix, Pixmeo Bernex, SUI), an 11° medial-to-lateral opening-wedge osteotomy, a medial conformal bone plate and screws (modified Tomofix plate, Depuy-Synthes, West Chesterfield, PA), and a wedge-shaped titanium alloy multi-component, osseo-integrative implant. Figure 1B and 1C show rendered images of the assembled and disassembled 4-component implant. When assembled, the interlocking surfaces mitigate component migration. This embodiment is made of Ti-6Al-4V alloy. Note that the assembled implant has a 25 mm diameter intramedullary opening for conversion to TKA if warranted, without the need to remove the implant. Components were fabricated using 3-D laser sintering, a 3-D printing technique that allows the superior and inferior surfaces to be comprised of a lattice structure printed as a continuation of the bulk material.

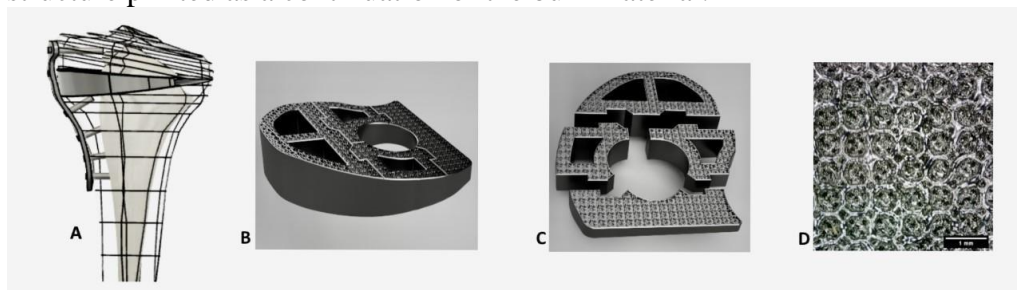


Figure 1: A) Implant and plate placed at osteotomy site. B) Multi-component implant geometry with lattice surface rendering. C) Disassembled view of implant. D) Micrograph of the lattice with average surface pore size of 550  $\mu\text{m}$ .

Figure 1D is a micrograph of the lattice structure for fixation by bone ingrowth. Four scaled lattices differing in size, but not geometry, were evaluated in a sliding resistance compression-spin test whereby the torque required to initiate sliding was measured. This parameter characterizes the initial stability of assembled components. The coarsest lattice was used for the implant, and had a 550  $\mu\text{m}$  surface pore size, with an internal pore size of 150  $\mu\text{m}$ , acceptable for bone ingrowth.

The results show comparisons of finite element analyses (Fusion 360, Autodesk, San Rafael, CA) of three models. First, the VTO as used clinically, specifically the opening medial wedge osteotomy bridged with a T-plate. Second was osteotomy filled with the multi-component implant, but with no medial plate. Lastly, the VTO using both multi-component implant and T-plate. The plate, separate screws, and implant were modeled as Ti-6Al-4V (Modulus = 113.9 GPa, Poisson's Ratio = 0.35). The material properties of cortical bone were assumed isotropic; Modulus = 17 GPa, Poisson's Ratio = 0.33. Cancellous bone was assumed isotropic, Modulus = 350 MPa, Poisson's Ratio = 0.25. Cortical and cancellous bone regions were simplified from CT image results. All structures were modelled with linear tetrahedral elements. Models were axially loaded with a total of 2600 N, distributed 50/50 on the medial and lateral plateau surfaces, and

the tibia fully fixed distally. This simple loading was chosen to represent single-leg loading during slow walking, estimated to 2x body weight for a 6 ft, 300-lb, BMI = 41 individual. Contact between screw/plate, screw/bone, bone/bone, and implant/bone was assigned a bonded boundary condition and interfaces between implant components were assigned a separation boundary condition. All contact assumptions can be modified for further analyses.

## RESULTS

To illustrate the effects of the multi-component implant, Figure 2 A-C shows the Mises stress distribution on a representative mid-frontal section. Figure 2A of the plate-only model displays a heatmap scale magnitude approximately four times that for models including the implant. Table 1 gives specific values at relevant nodes. The tabulated maximum stresses for models including the implant are not in the Figure 2 plane, but are located elsewhere at regions of implant-cortical bone contact.

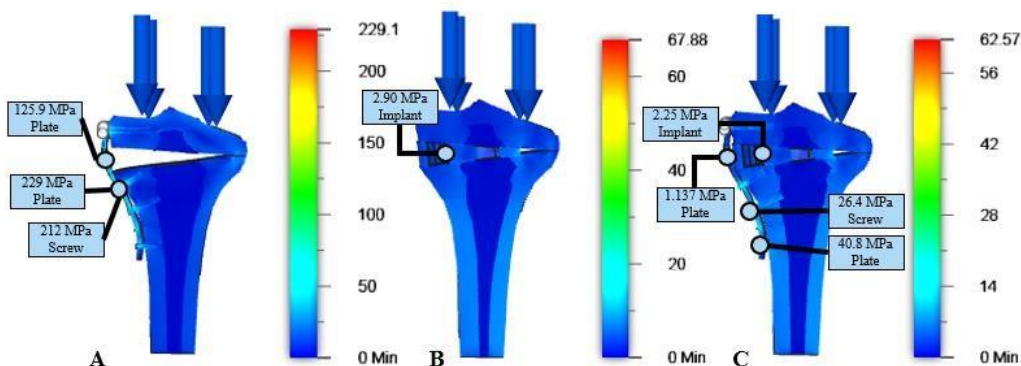


Figure 2: Mises stress distributions at mid-frontal plane for models: A) Plate-only; B) Implant-only; C) Plate and Implant. Stress magnitudes and locations are indicated by box and line and appear in Table 1 for comparison. Maximum stresses for models containing the implant are located elsewhere at regions of implant-cortical bone contact.

The stresses found for the Plate-only model are generally an order of magnitude greater than models with the implant *in situ*. Also, Plate-only values are comparable in magnitude to the fatigue strength of titanium alloy. This is exemplified comparing Figure 2A and 2C where the Plate-only stress was 125.9 MPa compared to 1.137 MPa at the corresponding location in the Plate and Implant model.

TABLE 1: COMPARISON OF MISES STRESS AT SPECIFIED LOCATIONS

Model	Maximum Stress in Plate (MPa)	Maximum Stress in Screws (MPa)	Maximum Stress in Implant (MPa)	Generic Stress in Bulk Implant (MPa)
Plate only	229	212	N/A	N/A
Implant only	N/A	N/A	67.9	2.90
Plate and Implant	40.8	26.4	62.6	2.25

Though less pronounced, the maximum stress in the plate and screw, 229 MPa and 212 MPa, respectively, for the Plate-only model decreased to 40.8 MPa and 26.4 MPa for the model of the Plate and Implant. The stress found at a typical location within the bulk implant, 2.25 MPa and 2.90 MPa, with and without the plate, respectively, correspond to

a design factor of approximately 100 with respect to estimated fatigue strength. The maximum stress in the implant 62.6 MPa with plate and 67.9 MPa without plate, occur at a point of contact between the implant and the medial cortical bone, suggesting the importance of cortical coverage, particularly related to potential issues of ingrowth fixation, bone remodeling, and wear. Observe that the addition of a plate reduces implant stress approximately 10%.

#### DISCUSSION

These results are best appreciated in clinical context. As expected, a typical valgus tibial osteotomy stabilized with a medial T-plate and screws was shown to be inadequate to support the excessive loads associated with morbidly obese patients. However, an implant used to fill the osteotomy space greatly decreases the stress within the T-plate and screws to approximately 15% to 20% of that for the T-plate alone. Furthermore, the nominal stresses in the implant approach physiologic levels, indicating that a high factor of safety exists with this implant design used for BMI>40 patients, even without the presence of the T-plate. Also as expected, the addition of a coarse lattice for osseointegration also provides the greatest resistance to sliding and will produce the least relative motion to achieve early bone ingrowth. Importantly, the models did not indicate adverse stresses at the component interlocking surfaces, which supports the premise that a multi-component implant can be inserted through a minimal incision and be assembled *in situ*, thereby reducing the risk of surgical complications in this patient population. This study, however, has not addressed many potentially significant issues, such as bending or torsional loading, effect of screw loosening, and the use of the T-plate as a compression plate to further restrain the implant components during the initial phases of osseointegration. Studies are underway to further model these considerations, as well as to conduct experimental verification of computational results.

#### CONCLUSIONS

It was demonstrated that a standard, plated valgus tibial osteotomy is likely to fail under the extreme loading conditions associated with morbidly obese patients, but that a multi-component, osseointegrative implant that fills the osteotomy space reduces the Mises stress levels to near-physiologic levels. These observations provide strong support for correction of a varus tibial deformity using an interposed multi-component implant in patients with BMI>40, an implant that may also reduce the surgical complications associated with obesity. The potential advantages of this procedure should also be considered desirable for osteotomy in high-use younger patients (BMI<40).

#### ACKNOWLEDGMENTS

Grateful thanks to Kyle E. Cleveland, who provided the graphic rendering of the implant with the lattice surface.

#### DISCLOSURE

All authors received compensation as design consultants to VKI, LLC; U.R. Pontius, CEO

Patent USPO# 10842632 issued to Uwe R. Pontius, MD, PhD(ME), FAAOS

#### REFERENCES

- Ü. Tuhanioglu, H. U. Oğur, F. Seyfettinoğlu, H. Çiçek, and A. Gültekin, "High Tibial Osteotomy in Obese Patients: Is Successful Surgery Enough for a Good Outcome?," *Journal of Clinical Orthopaedics and Trauma*, Oct-2019.
- S. Preston, J. Howard, D. Naudie, L. Somerville, and J. McAuley, "Total Knee Arthroplasty After High Tibial Osteotomy: No Differences Between Medial and Lateral Osteotomy Approaches," *Clinical Orthopaedics and Related Research*, Jan-2014. [3] X. Chen, Z. Yang, H. Li, S. Zhu, Y. Wang, and W. Qian, "Higher Risk of Revision in Total Knee Arthroplasty After High Tibial Osteotomy: A Systematic Review and Updated Meta-Analysis," *BMC Musculoskeletal Disorders*, 06-Mar-2020.
- L. Boyce, A. Prasad, M. Barrett, S. Dawson-Bowling, S. Millington, S. A. Hanna, and P. Achan, "The Outcomes of Total Knee Arthroplasty in Morbidly Obese Patients: a Systematic Review of the Literature," *Archives of Orthopaedic and Trauma Surgery*, Apr-2019.
- S. J. Song, D. K. Bae, K. I. Kim, and C. H. Lee, "Conversion Total Knee Arthroplasty after Failed High Tibial Osteotomy," *Knee Surgery & Related Research*, Jun-2016.
- M. Herbst, M.-D. Ahrend, L. Grünwald, C. Fischer, S. Schröter, and C. Ihle, "Overweight Patients Benefit from High Tibial Osteotomy to the Same Extent as Patients with Normal Weights but Show Inferior Mid-term Results," *Knee Surgery, Sports Traumatology, Arthroscopy*, 11-Feb-2021.
- C.-A. Luo, S.-Y. Hua, S.-C. Lin, C.-M. Chen, and C.-S. Tseng, "Stress and Stability Comparison Between Different Systems for High Tibial Osteotomies," *BMC Musculoskeletal Disorders*, 25-Mar-2013.

## APPENDIX C: PHOTOS OF PLA IMPLANT SURFACES DURING FIXTURE DESIGN

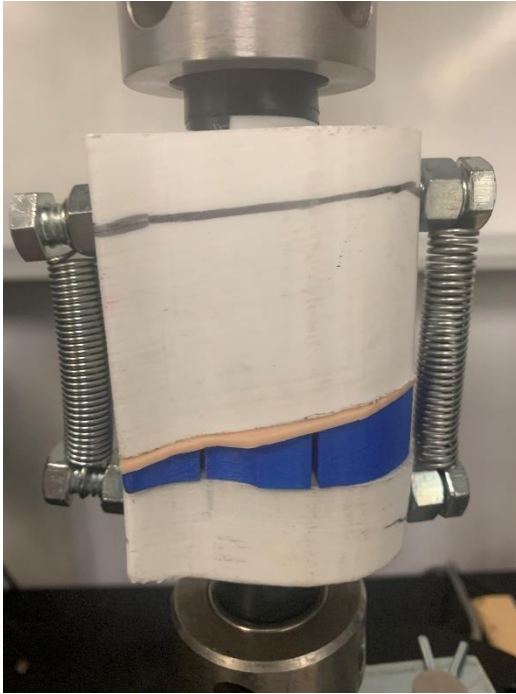


Figure 26 Dry wear fixture with PLA implant

### PLA Pre-Test Images

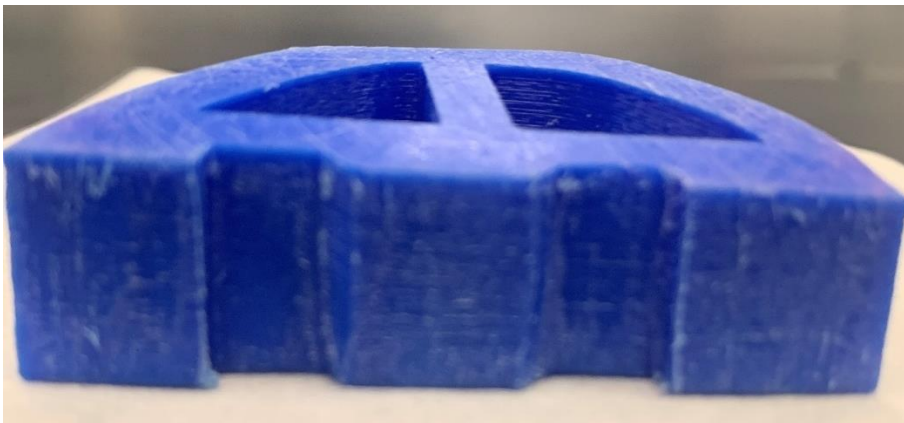


Figure 27 Medial



Figure 28 Lateral



Figure 29 Anterior Interface with Medial

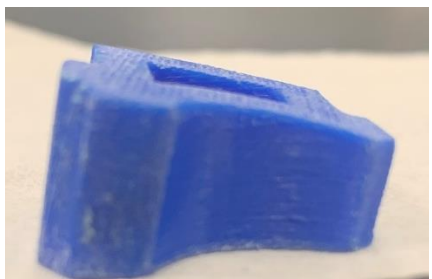


Figure 30 Anterior Interface with Posterior

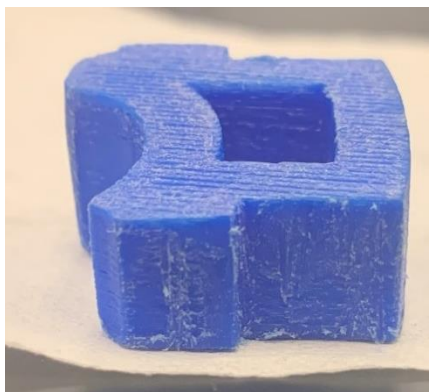


Figure 31 Anterior Interface with Lateral

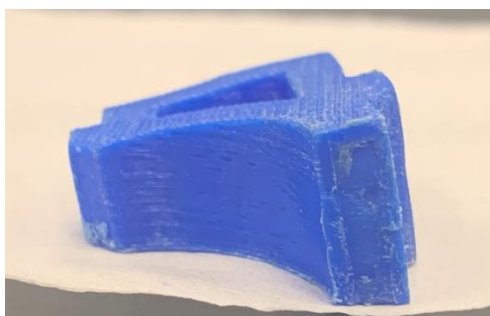


Figure 32 Posterior Interface with Anterior



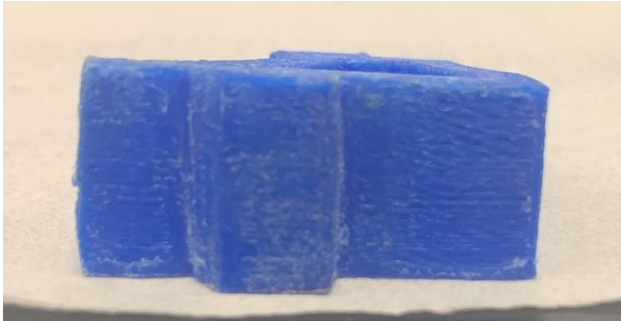


Figure 33 Posterior Interface with Medial

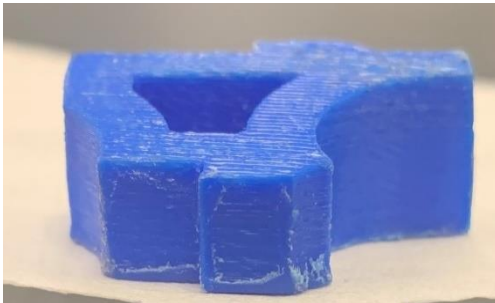


Figure 34 Posterior Interface with Lateral

### PLA Post 10,000 Loading Cycles

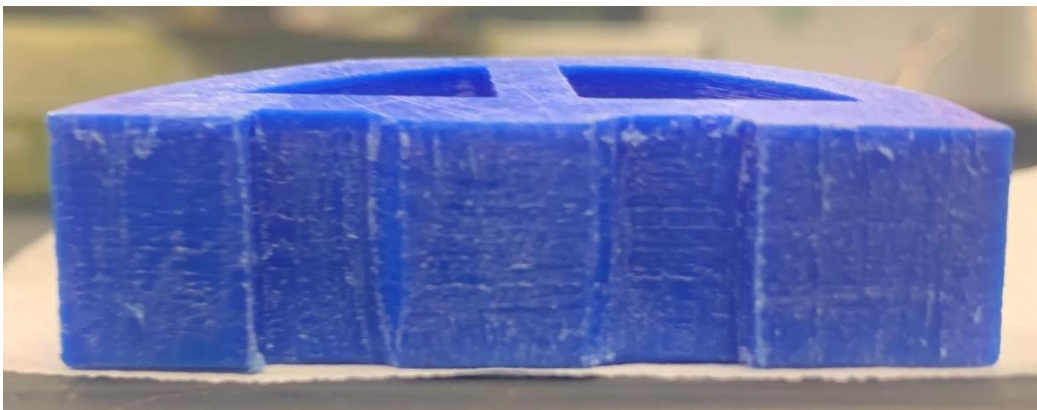


Figure 35 Medial



Figure 36 Lateral



Figure 37 Anterior Interface with Medial

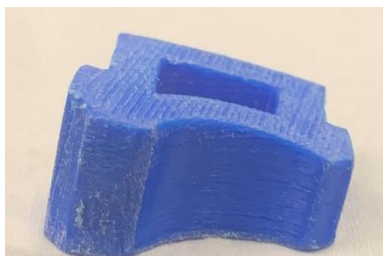


Figure 38 Anterior Interface with Posterior



Figure 39 Anterior Interface with Lateral

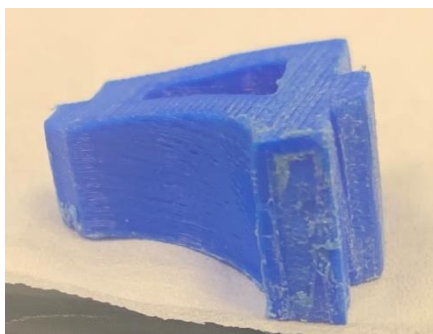


Figure 40 Posterior Interface with Anterior



Figure 41 Posterior Interface with Medial



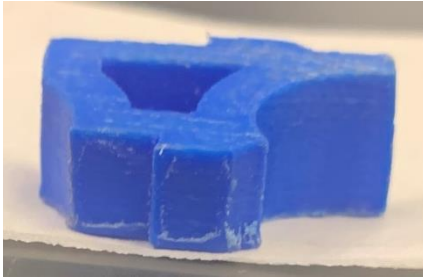


Figure 42 Posterior Interface with Lateral

PLA Post 10,000 Loading Cycles

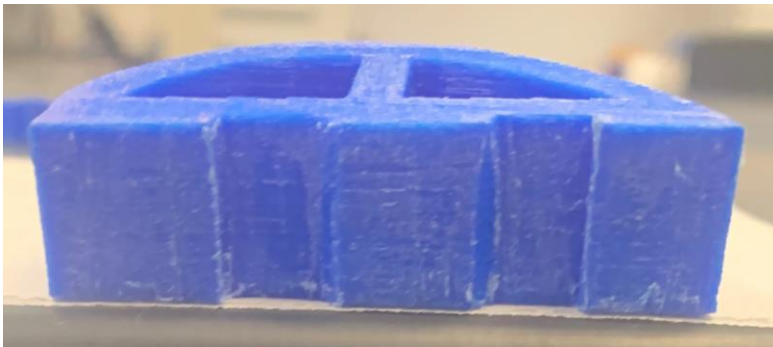


Figure 43 Medial



Figure 44 Lateral

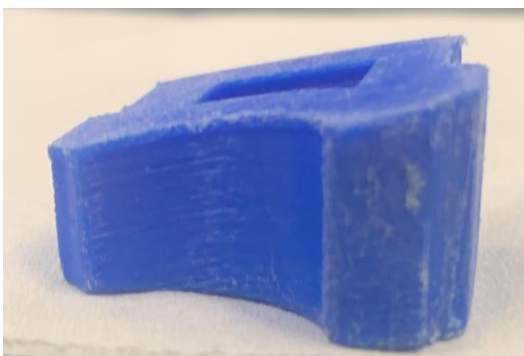


Figure 45 Anterior Interface with Posterior

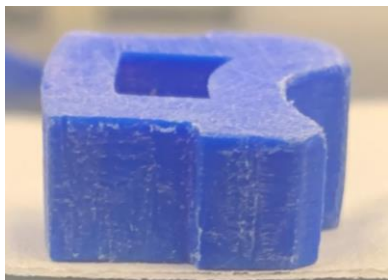


Figure 46 Anterior Interface with Lateral

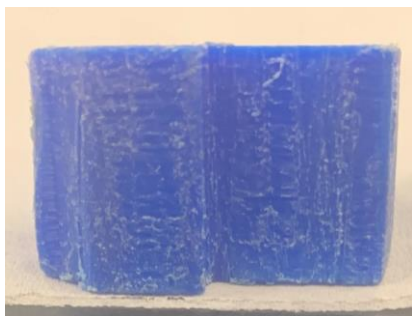


Figure 47 Anterior Interface with Medial

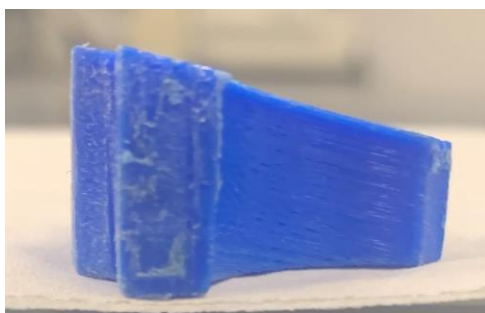


Figure 48 Posterior Interface with Anterior

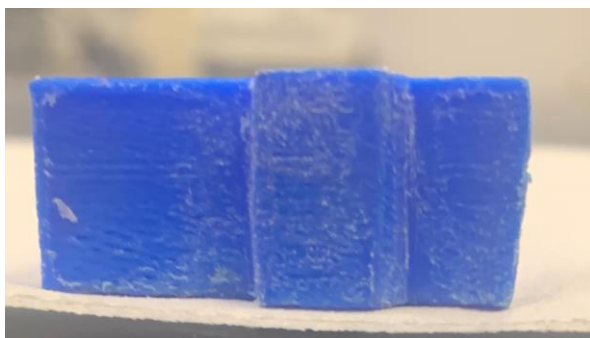
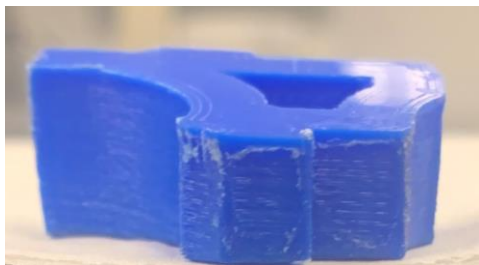


Figure 49 Posterior Interface with Medial



*Figure 50* Posterior Interface with Lateral

### APPENDIX D: PHOTOS OF STAINLESS-STEEL IMPLANT SURFACES

#### Pretest Stainless-Steel Images

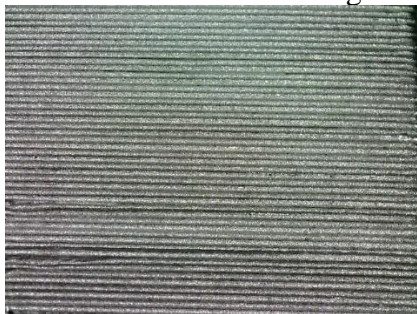


Figure 51A

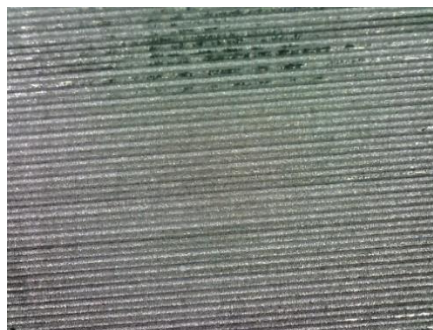


Figure 52AA

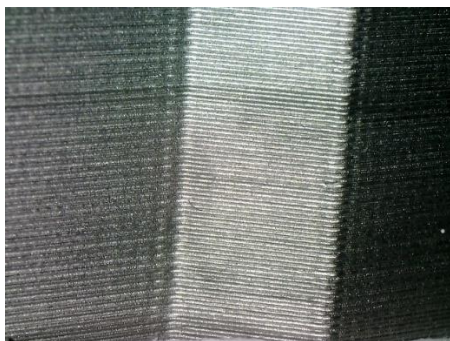


Figure 53AB

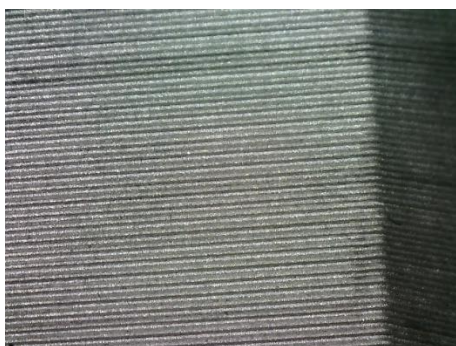


Figure 54AC

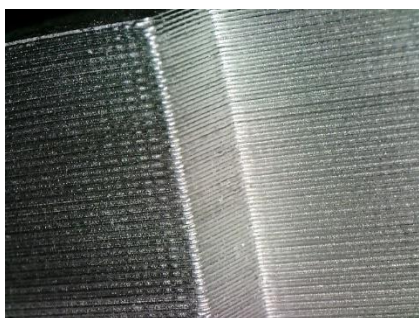


Figure 55AD



Figure 56AE

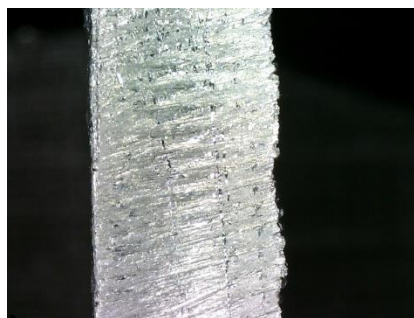


Figure 57AF



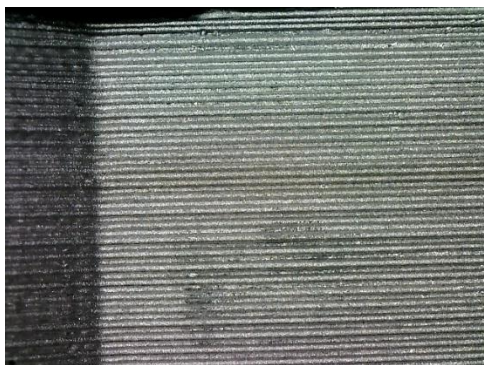


Figure 58AG

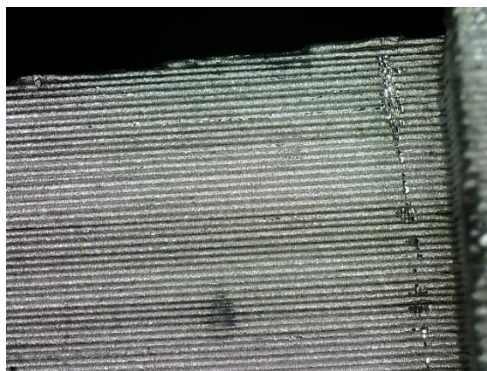


Figure 62AK

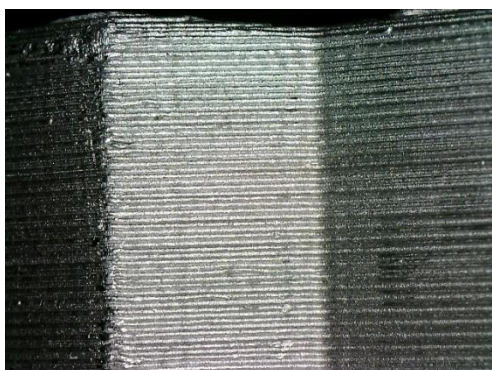


Figure 59AH

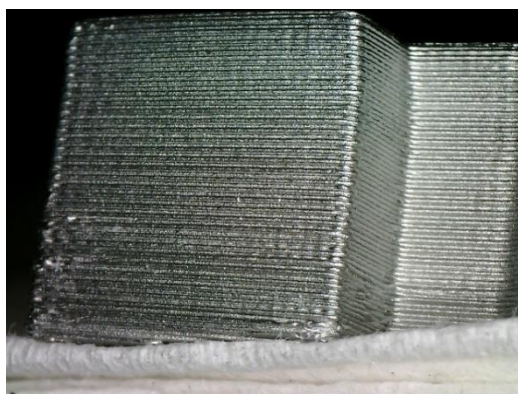


Figure 63B

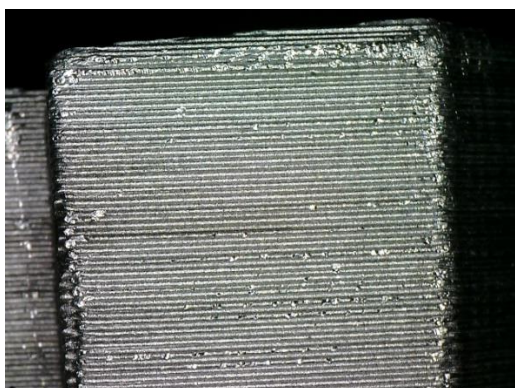


Figure 60AI

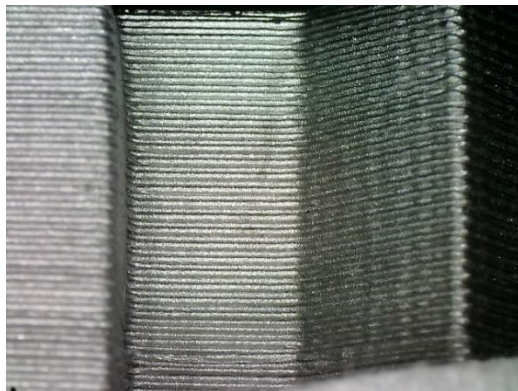


Figure 64C

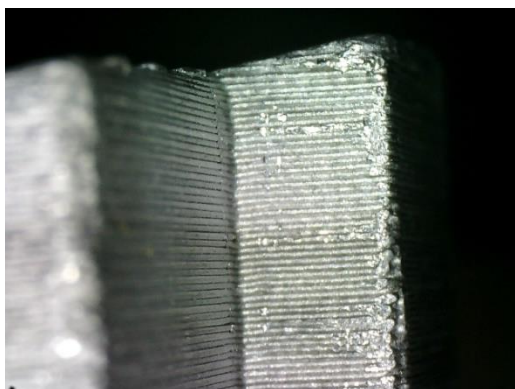


Figure 61AJ



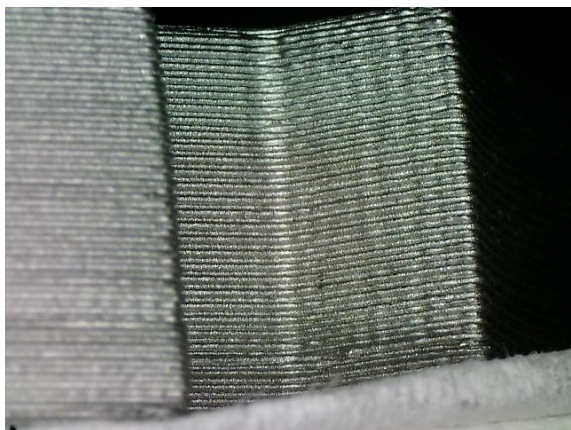


Figure 65D

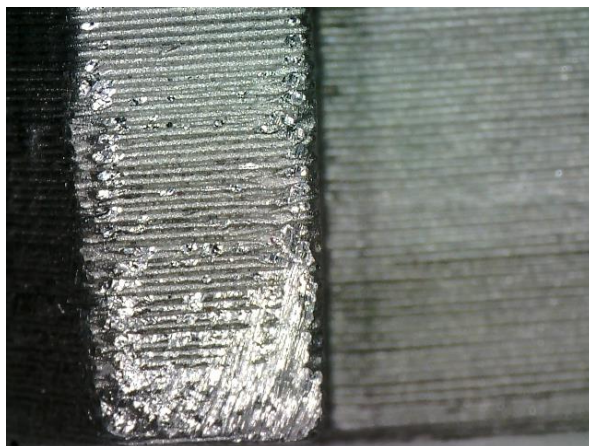


Figure 68G



Figure 66E

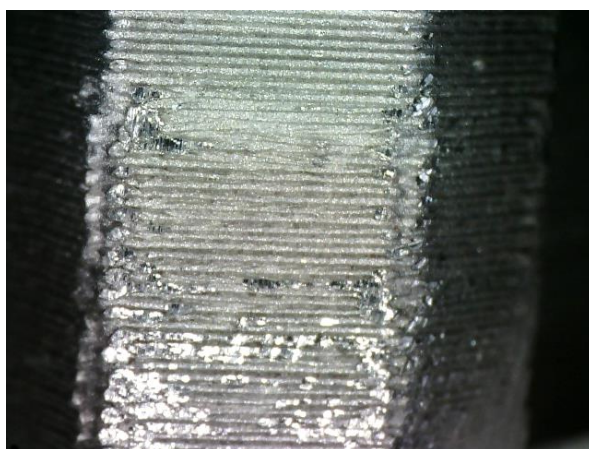


Figure 69H

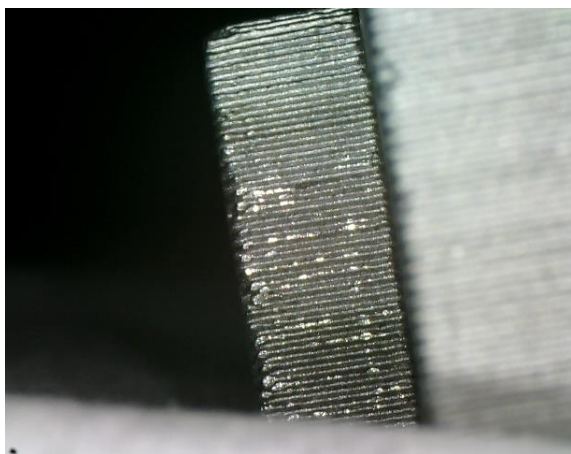


Figure 67F

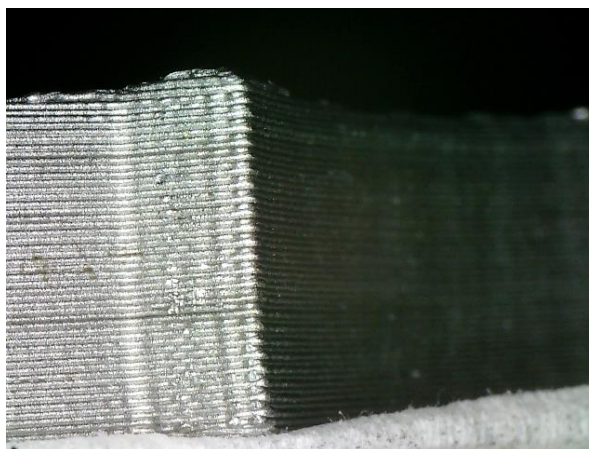


Figure 70I



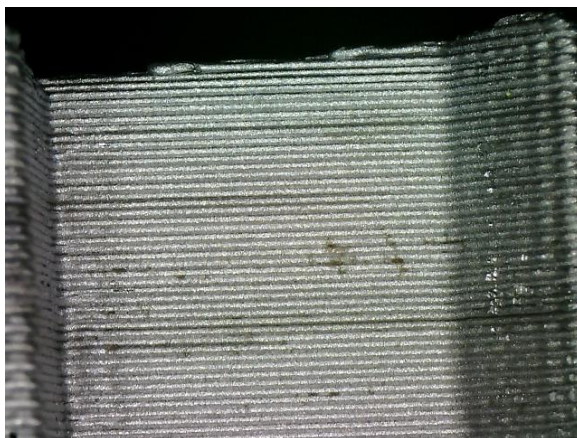


Figure 71J

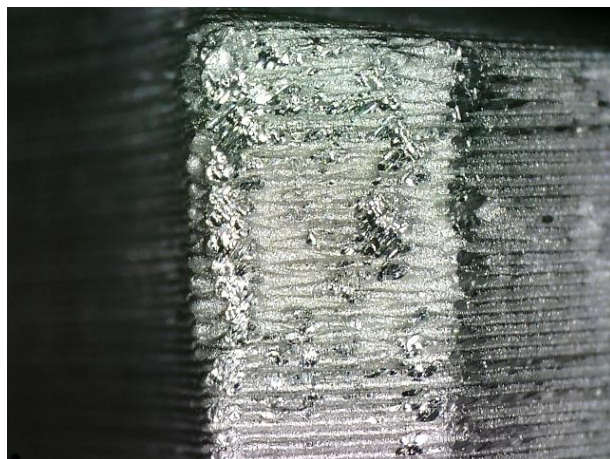


Figure 74M

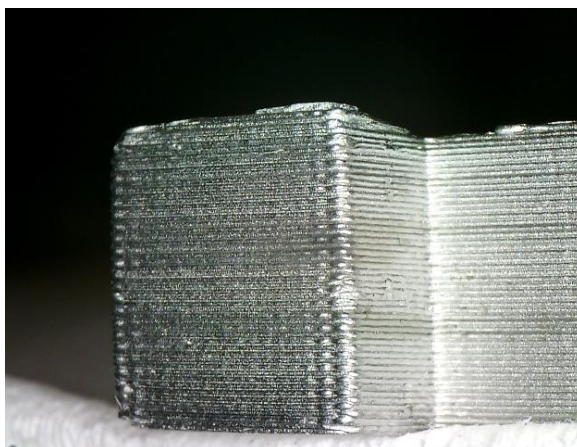


Figure 72K

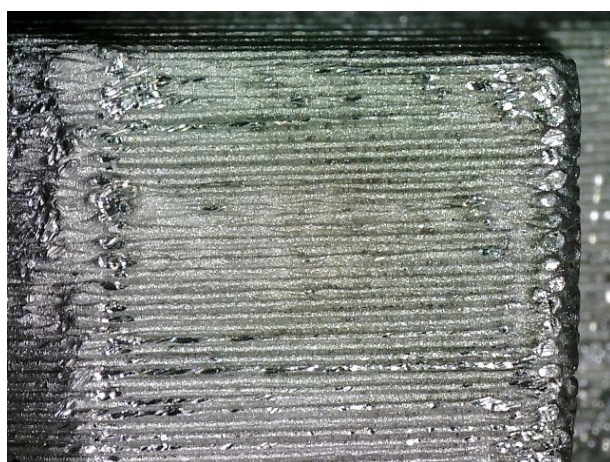


Figure 75N



Figure 73L

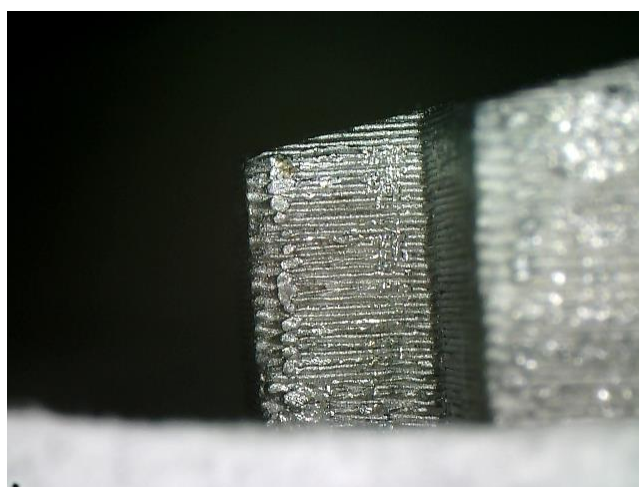


Figure 76O



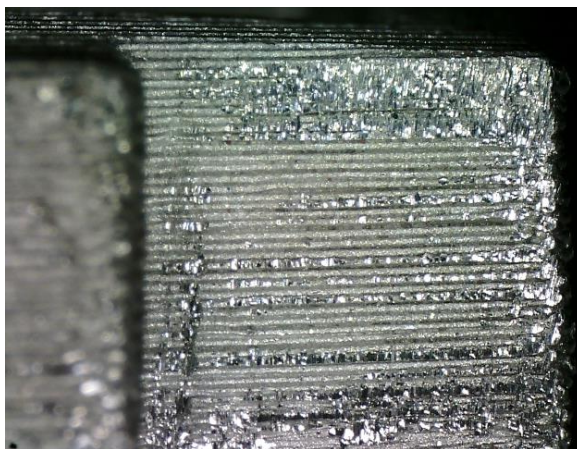


Figure 77P



Figure 80S

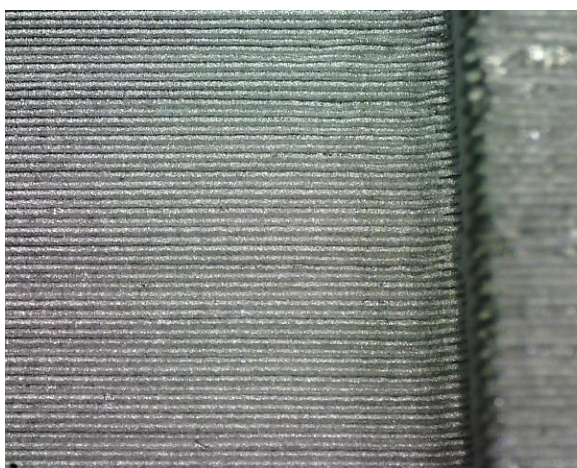


Figure 78Q

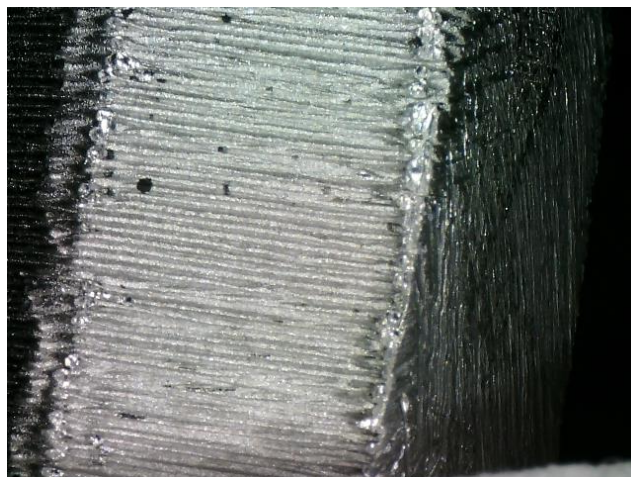


Figure 81TU

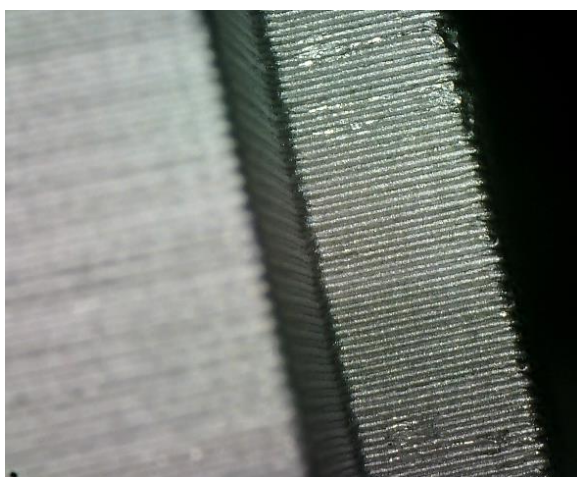


Figure 79R

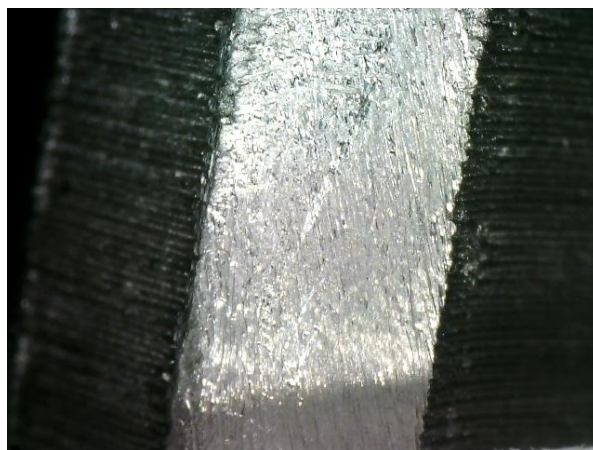


Figure 82V



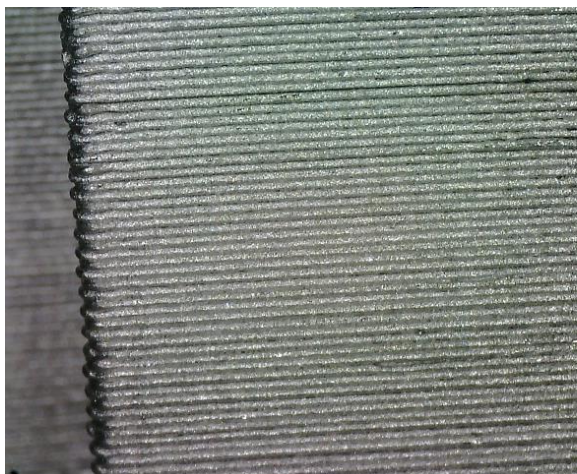


Figure 83W

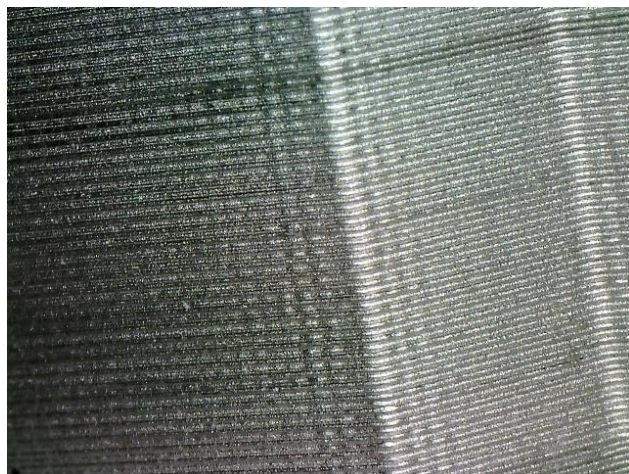


Figure 86Z

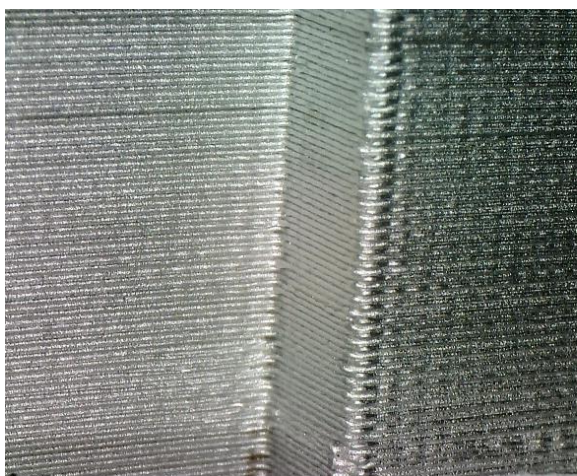


Figure 84X



Figure 85Y



Post 10,000 Cyclic Loading Cycles



Figure 87A



Figure 90AC



Figure 88AA

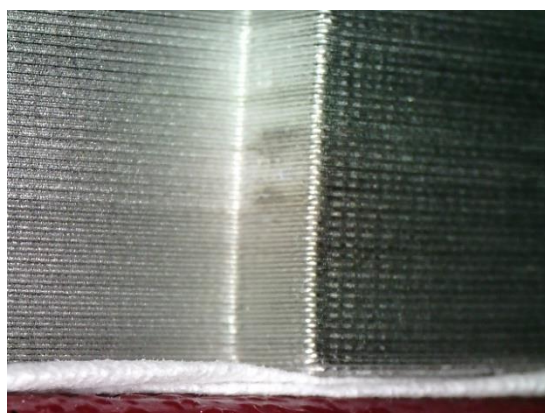


Figure 91AD

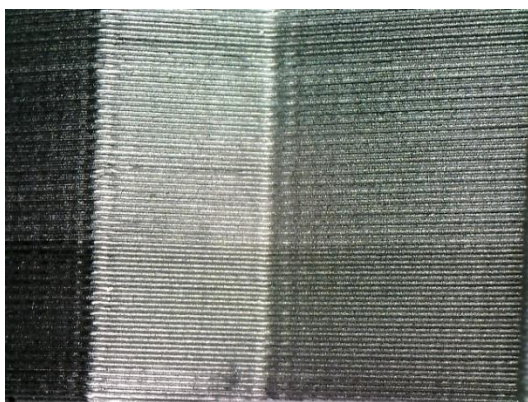


Figure 89AB



Figure 92AE



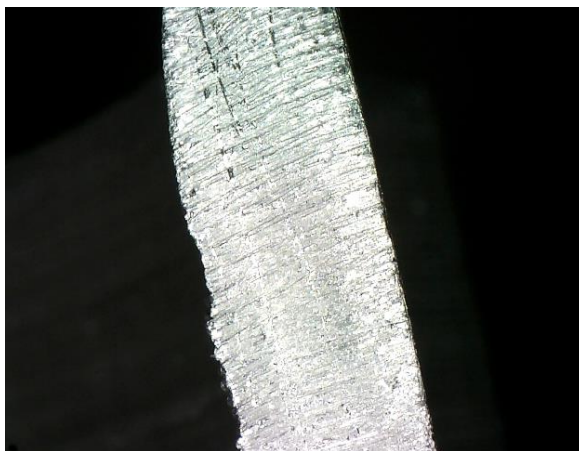


Figure 93AF

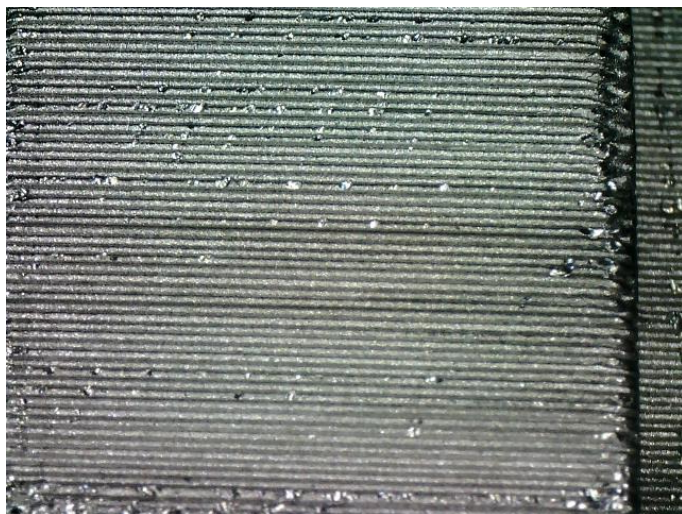


Figure 96AI

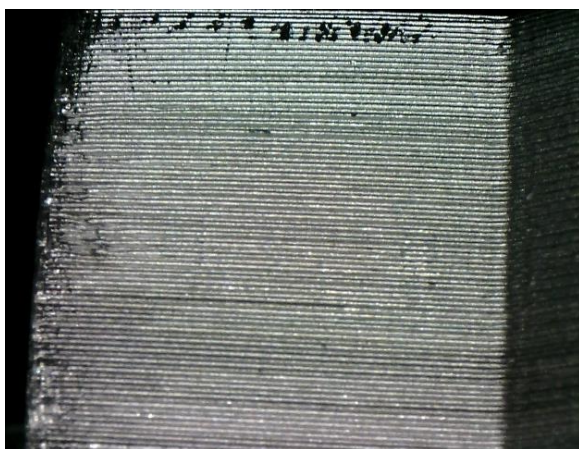


Figure 94AG

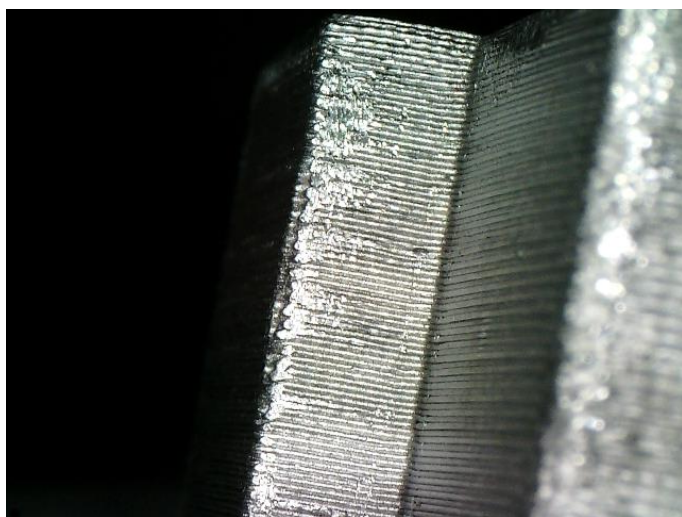


Figure 97AJ

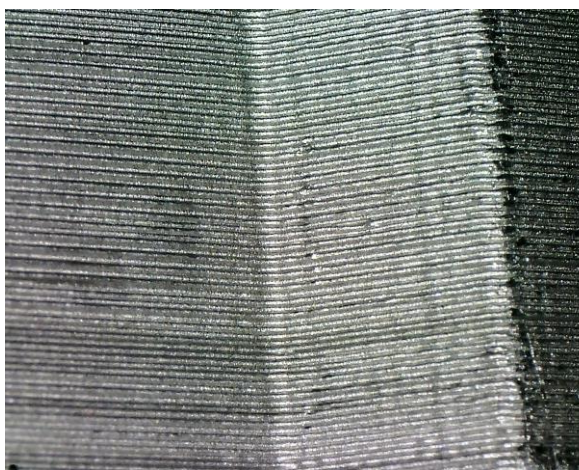


Figure 95AH

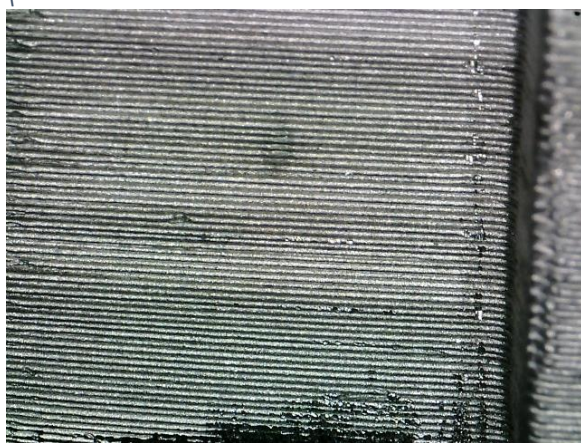


Figure 98AK



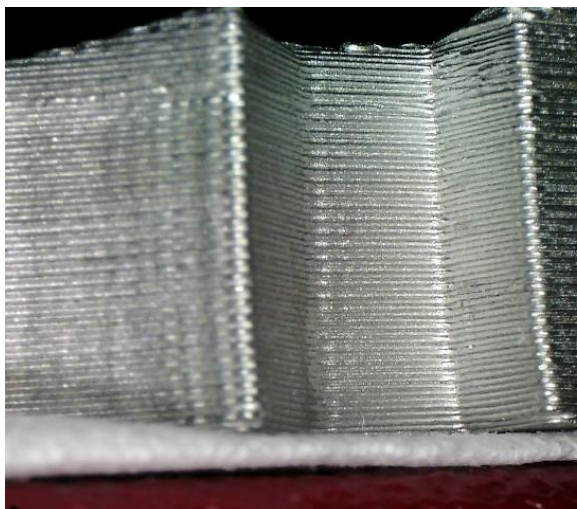


Figure 99B

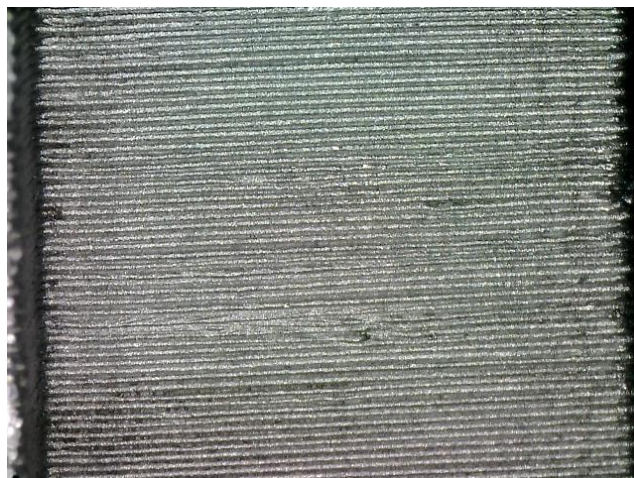


Figure 102E

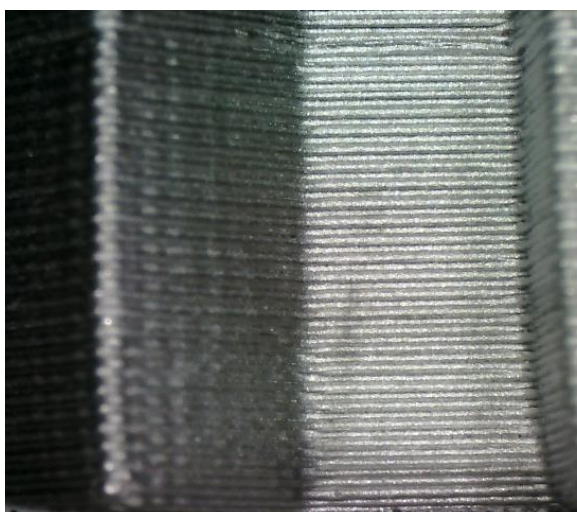


Figure 100C

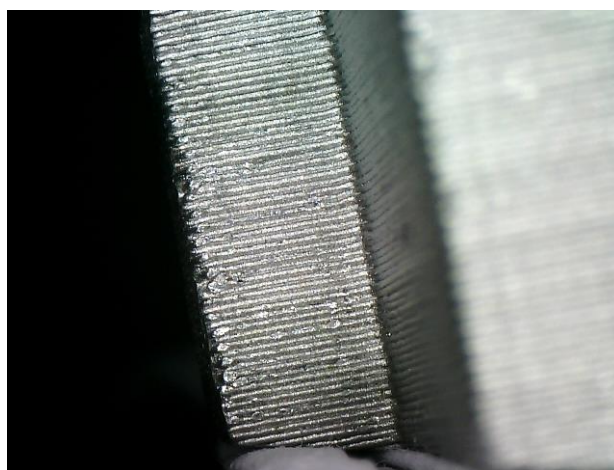


Figure 103F

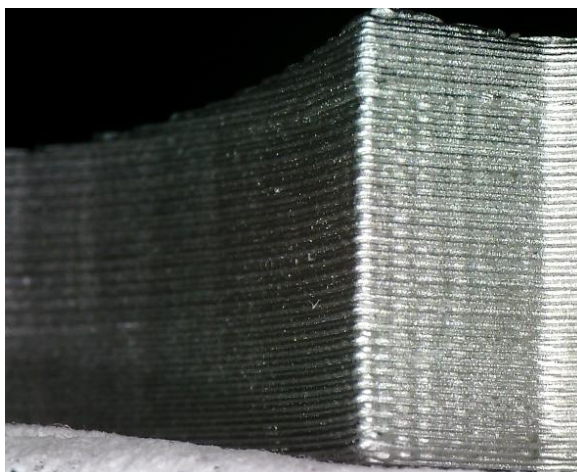


Figure 101D

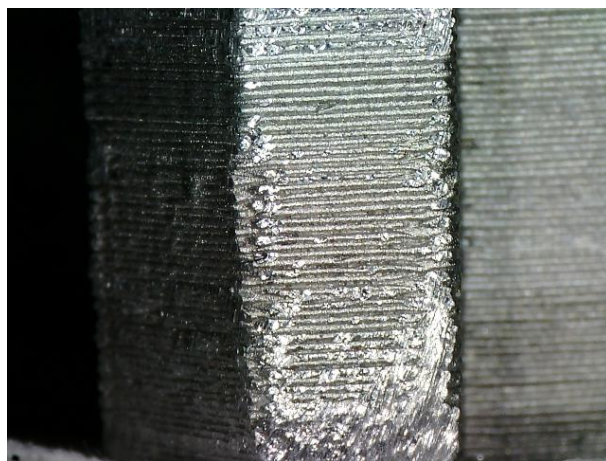


Figure 104G



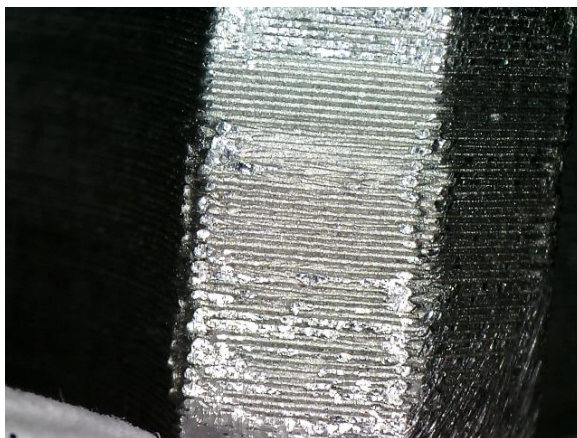


Figure 105H

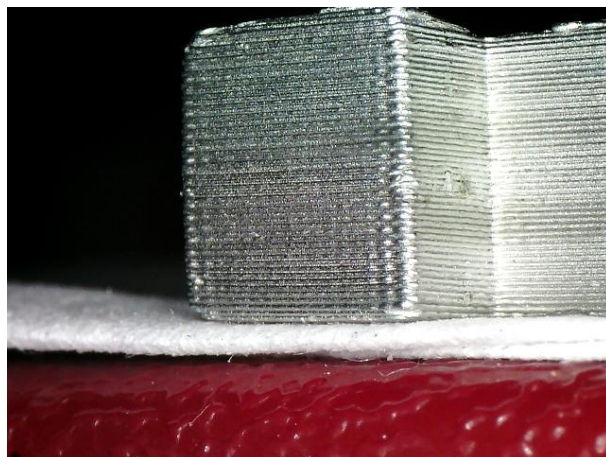


Figure 108K

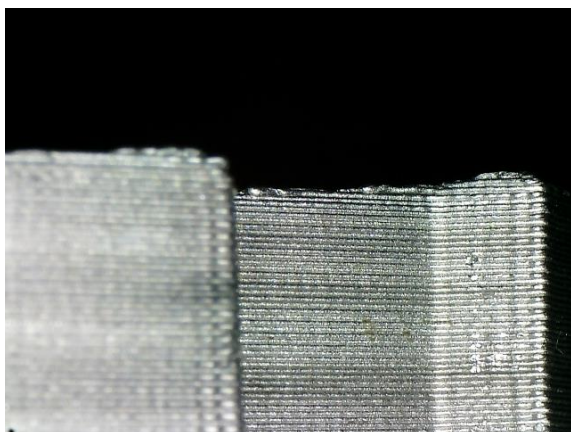


Figure 106I

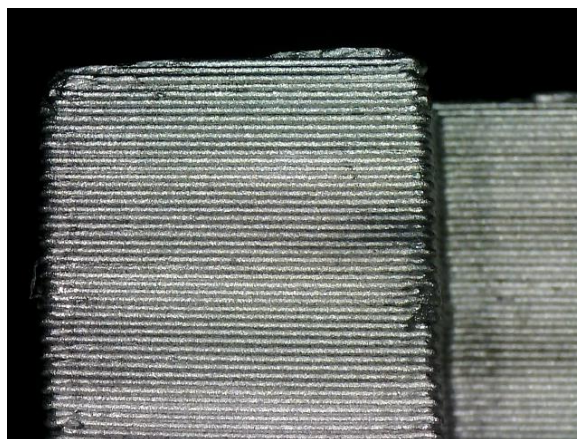


Figure 109L

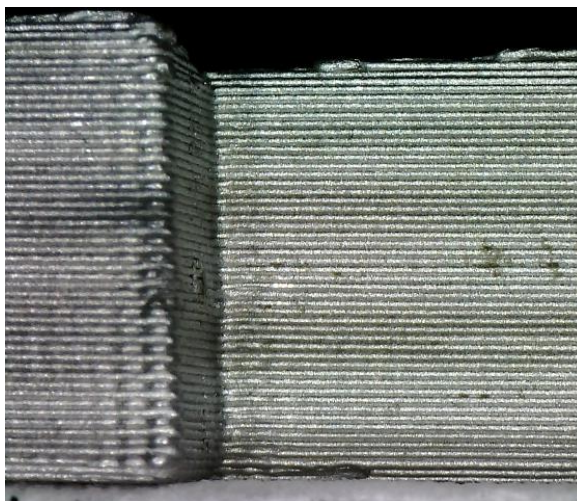


Figure 107J

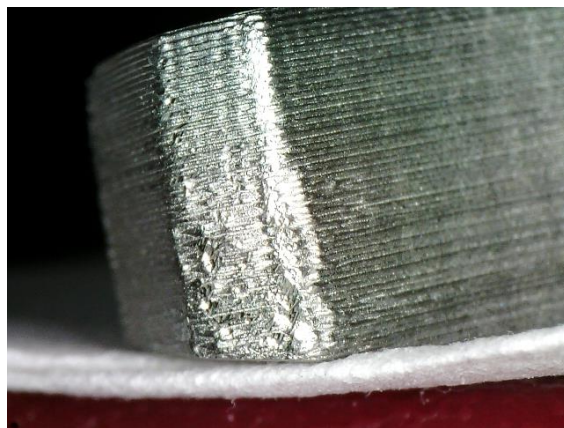


Figure 110M



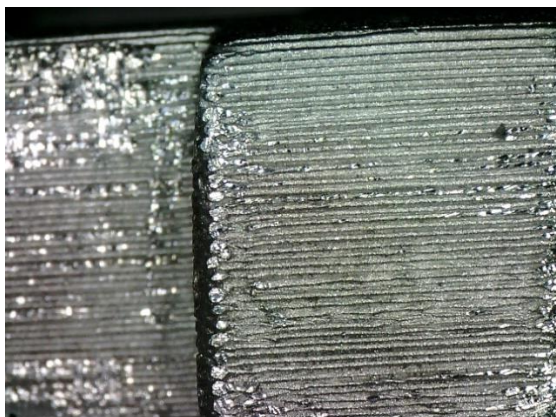


Figure 111N

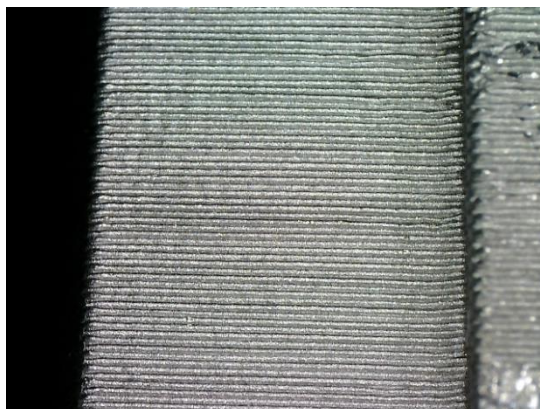


Figure 114Q

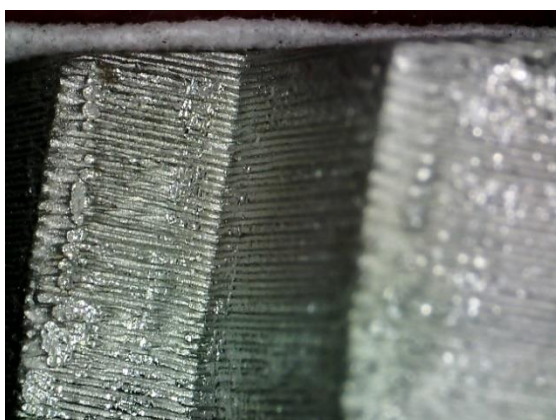


Figure 112O

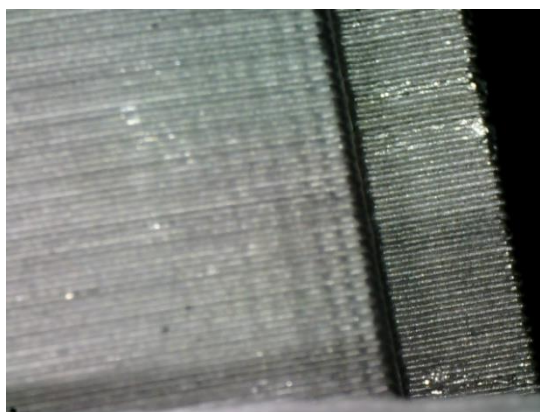


Figure 115R

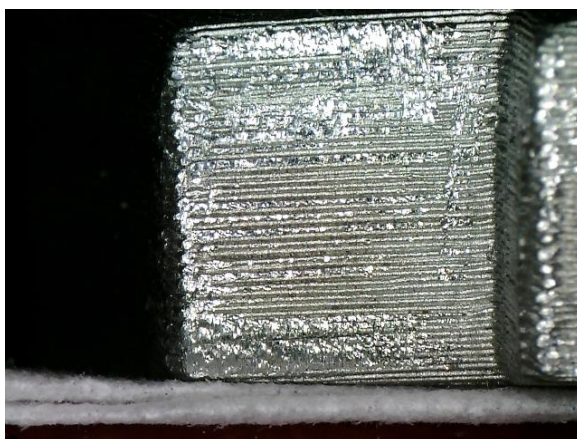


Figure 113P

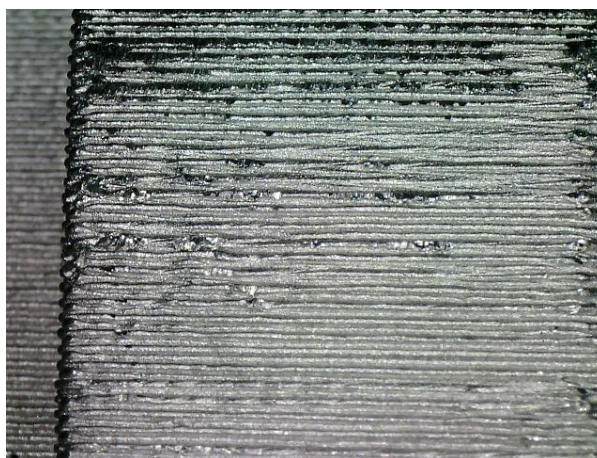


Figure 116S



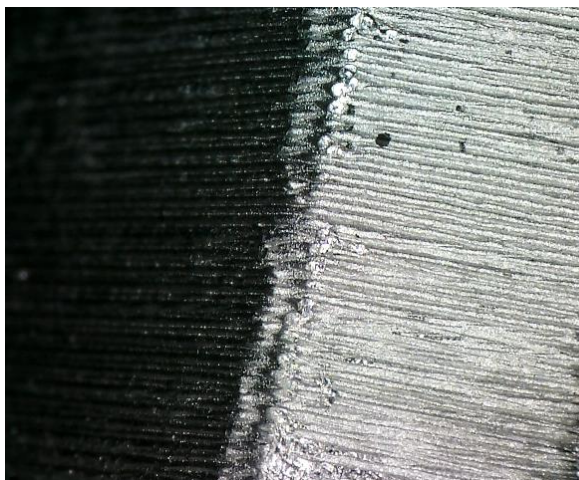


Figure 117TU

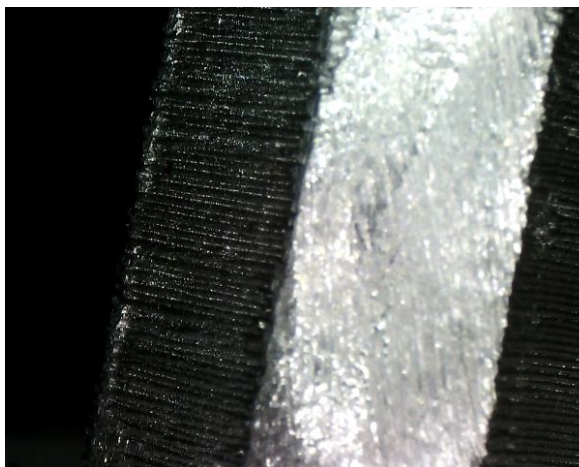


Figure 118V

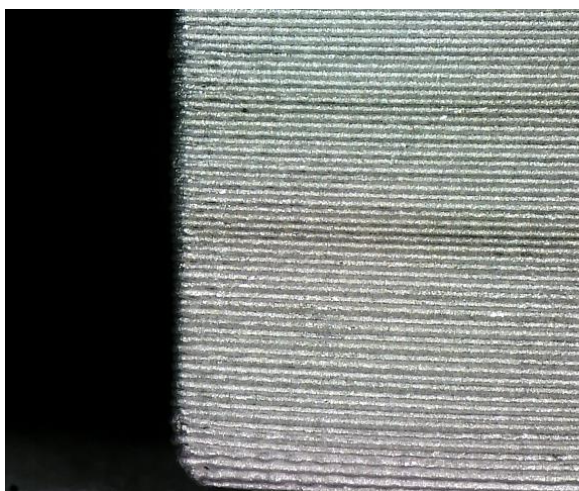


Figure 119W

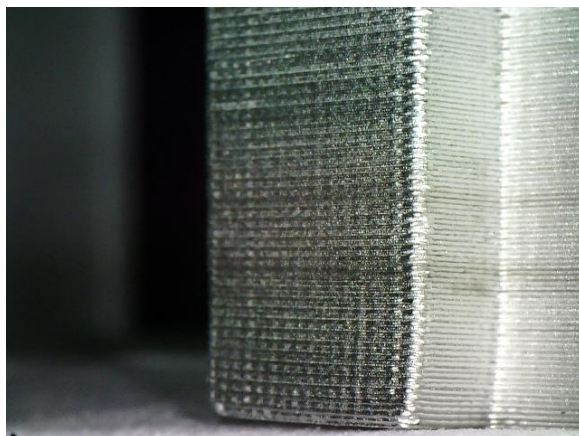


Figure 120X



Figure 121Y



Figure 122Z



Post 50,000 Loading Cycles



Figure 123A



Figure 126AC

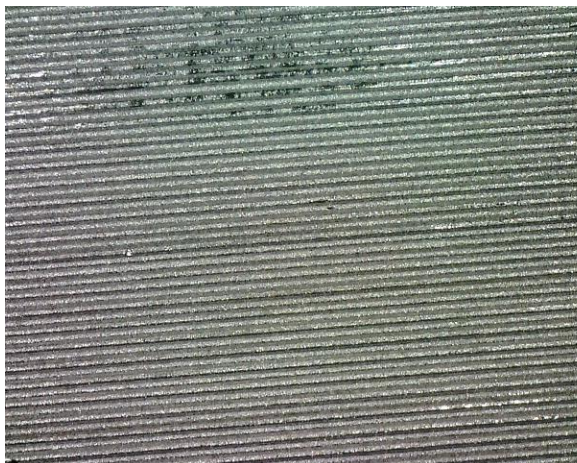


Figure 124AA

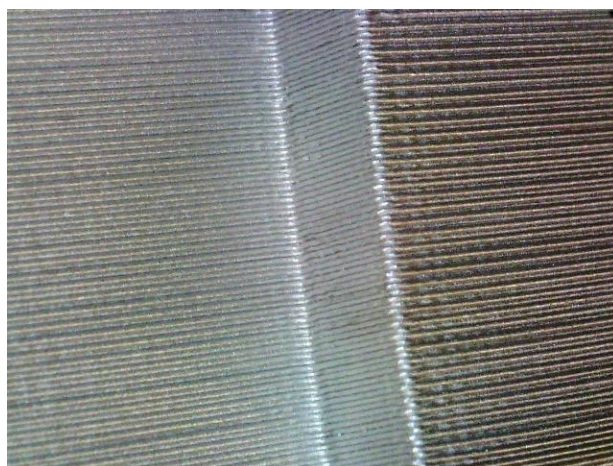


Figure 127AD



Figure 125AB



Figure 128AE



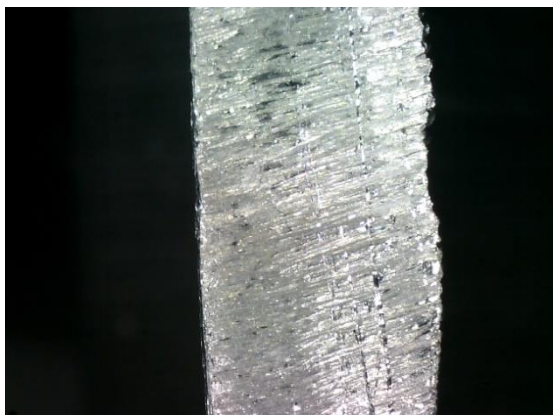


Figure 129AF

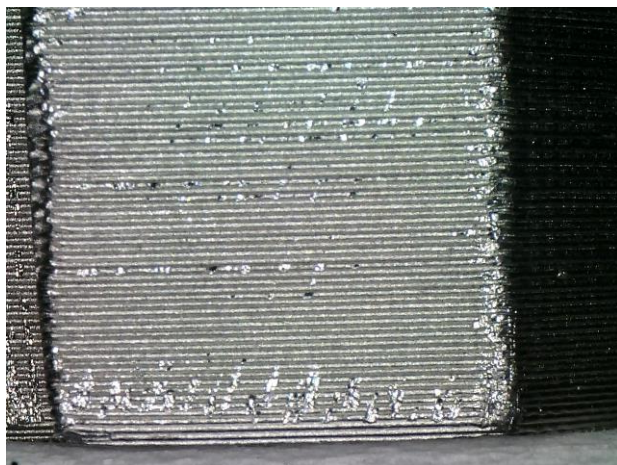


Figure 132AI

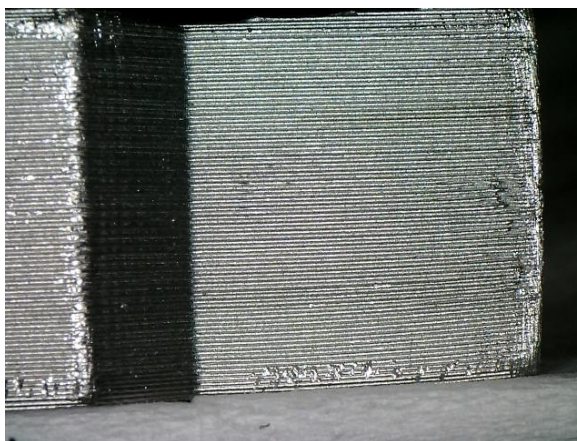


Figure 130AG

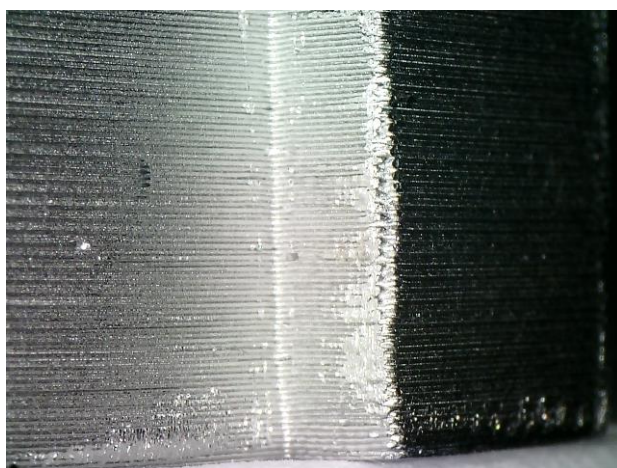


Figure 133AI

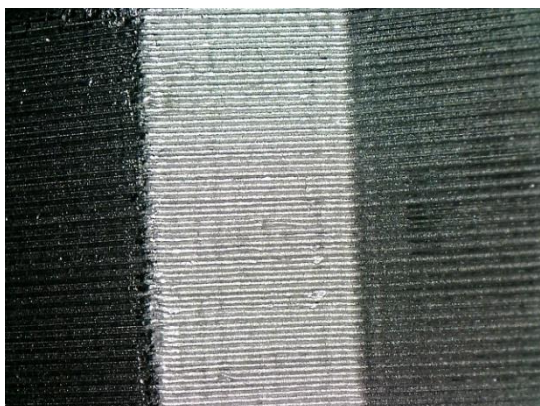


Figure 131AH

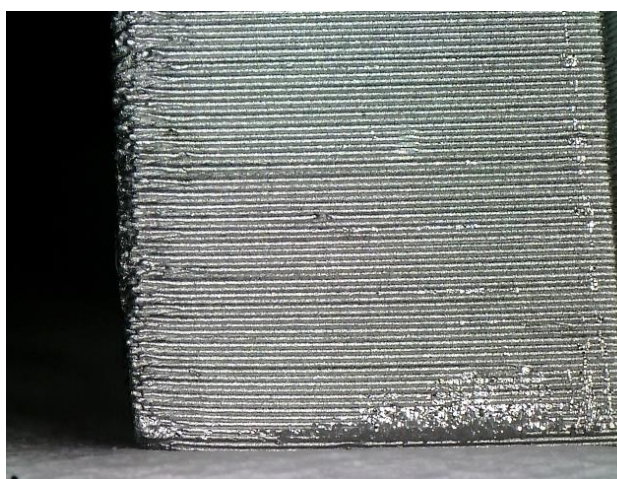


Figure 134AK



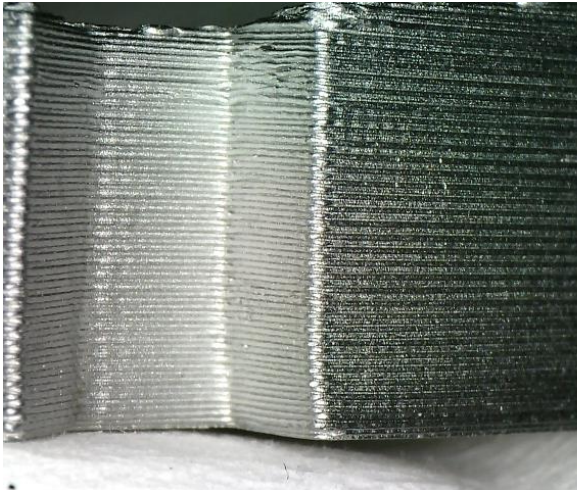


Figure 135B

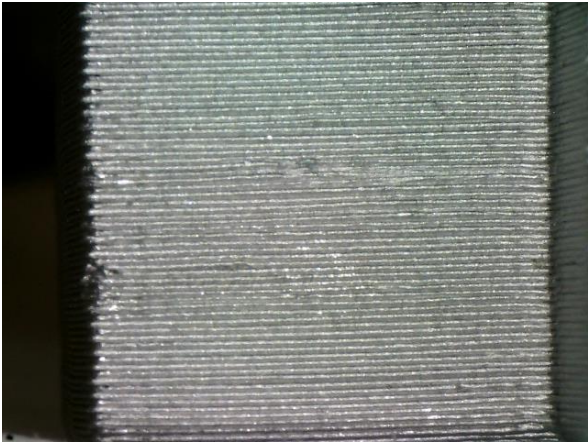


Figure 138E

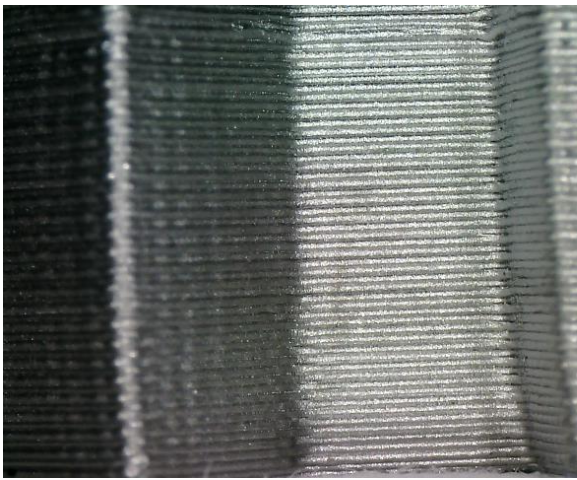


Figure 136C

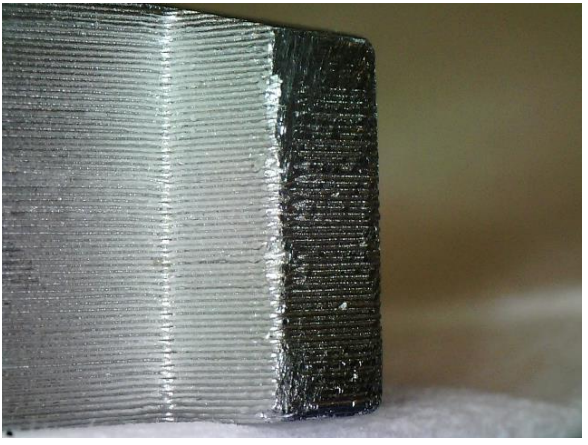


Figure 139F

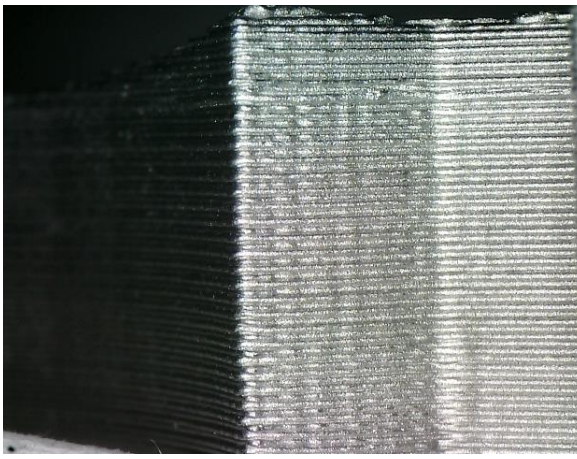


Figure 137D

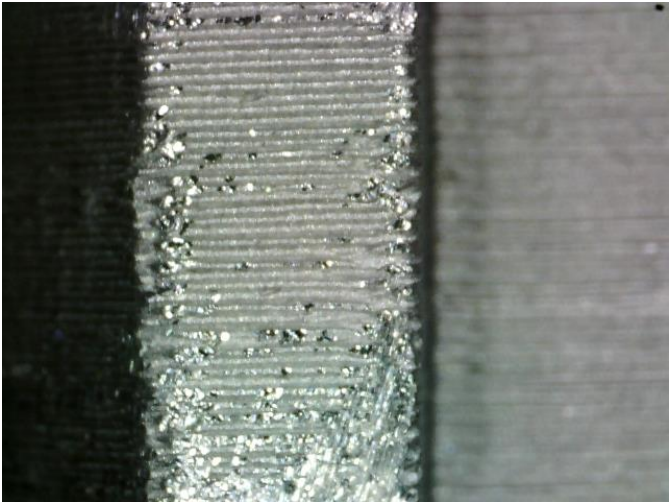


Figure 140G





Figure 141H

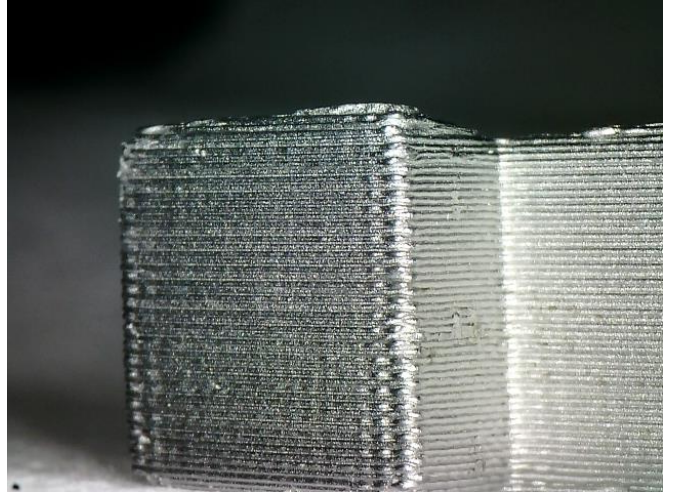


Figure 144K

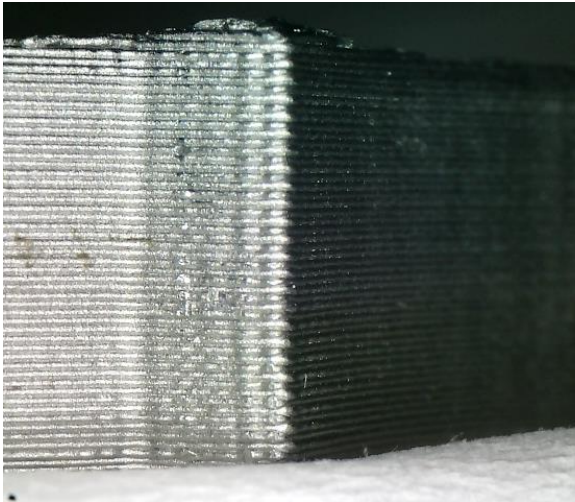


Figure 142I



Figure 145L

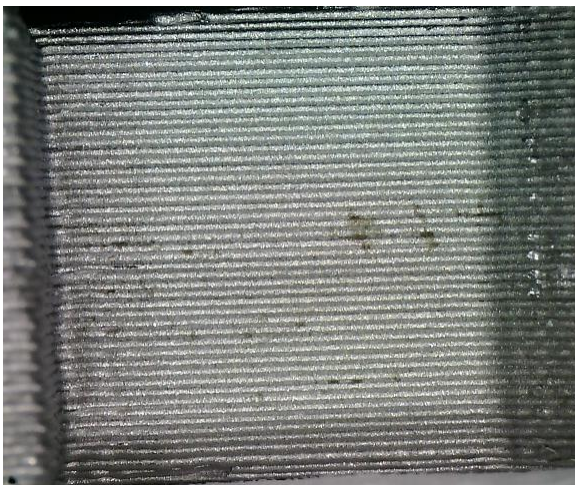


Figure 143J

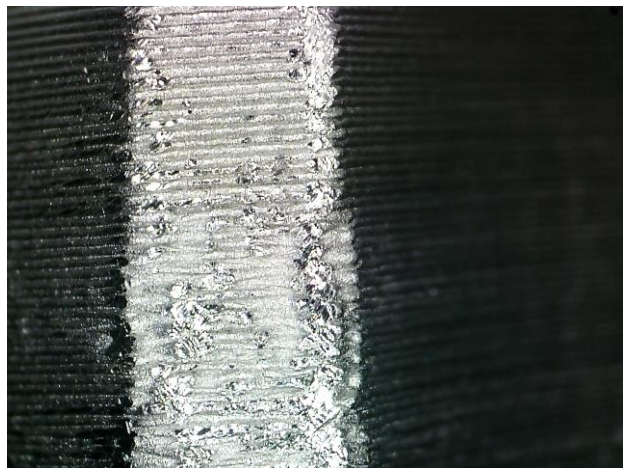


Figure 146M



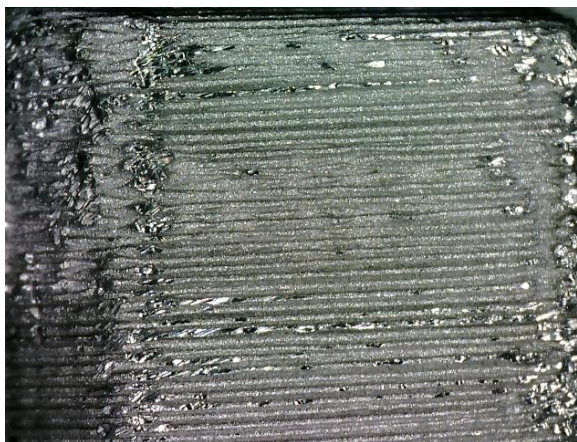


Figure 147N



Figure 150Q

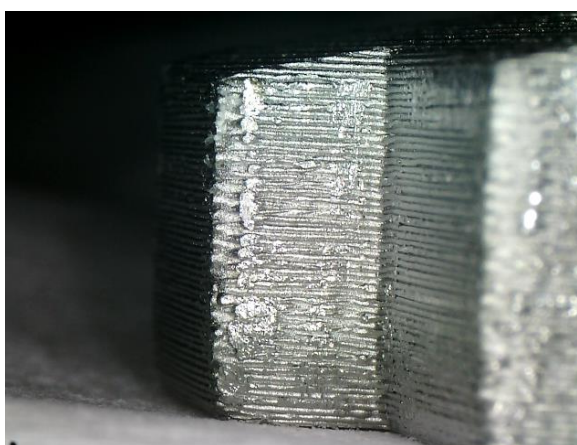


Figure 148O

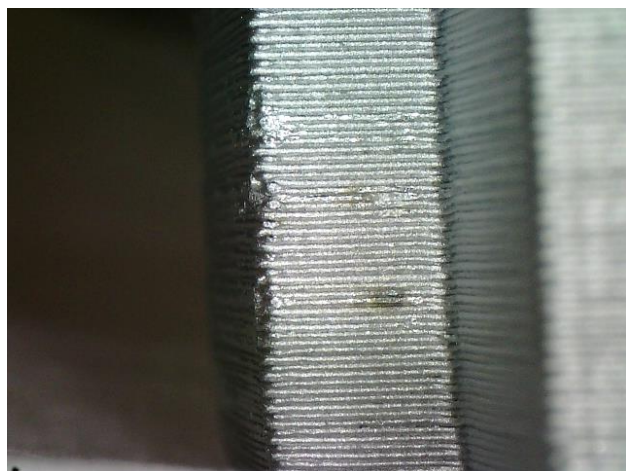


Figure 151R

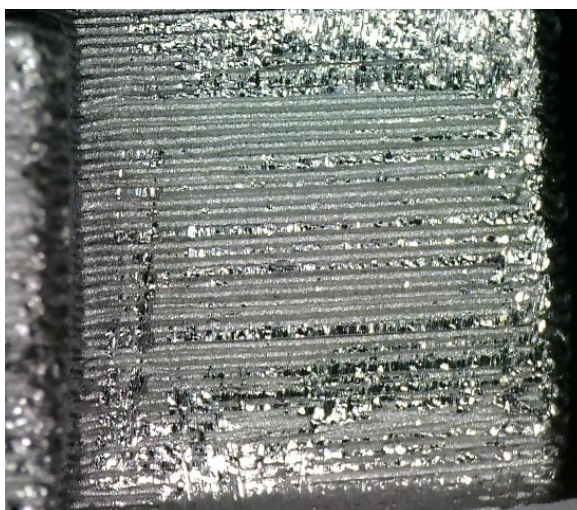


Figure 149P

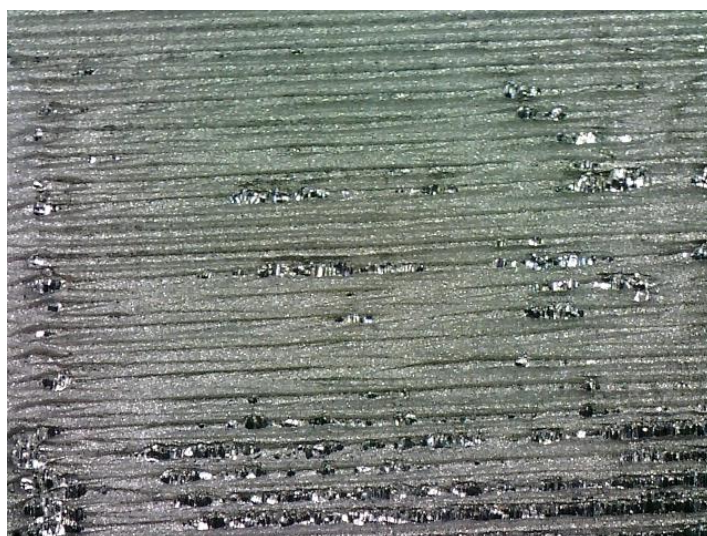


Figure 152S



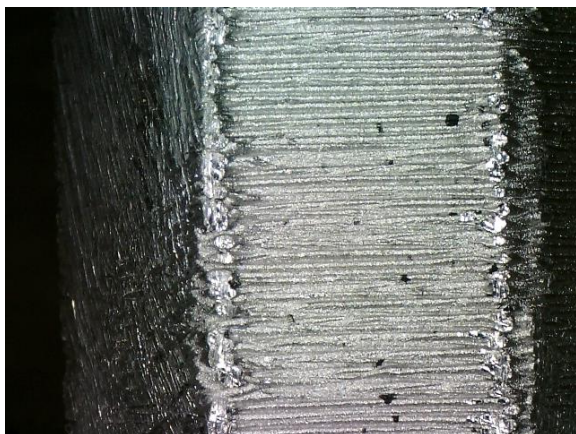


Figure 153TU

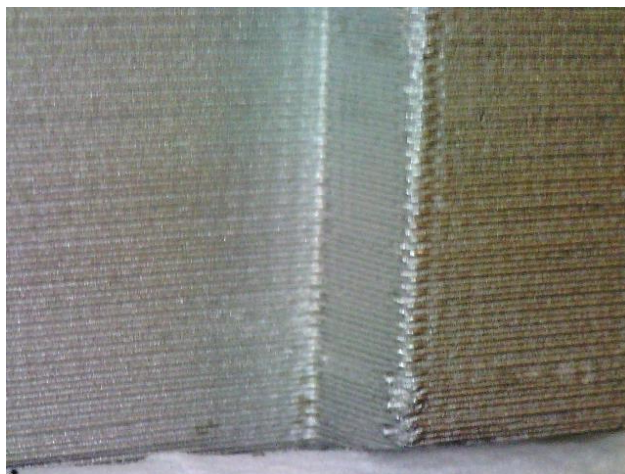


Figure 156X

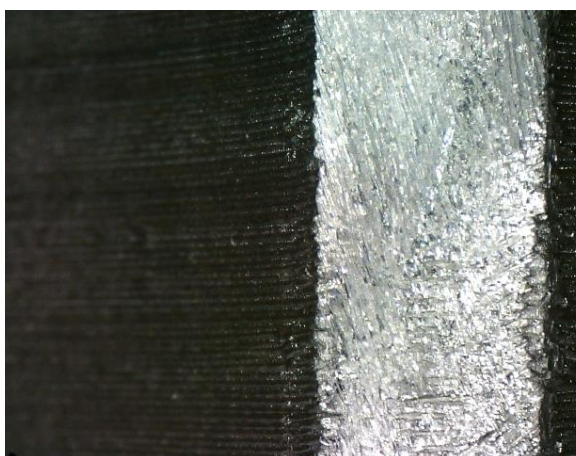


Figure 154V

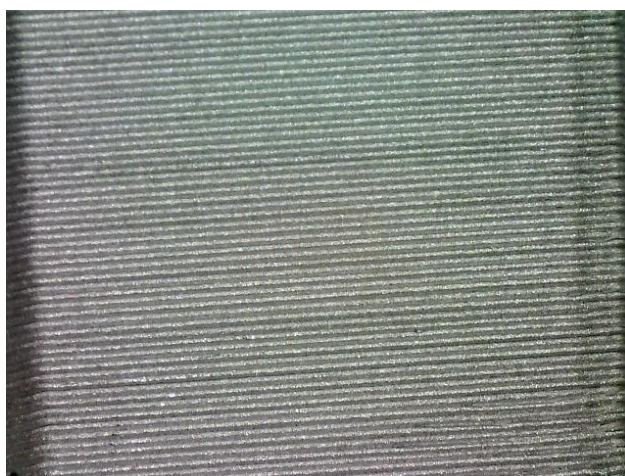


Figure 157Y

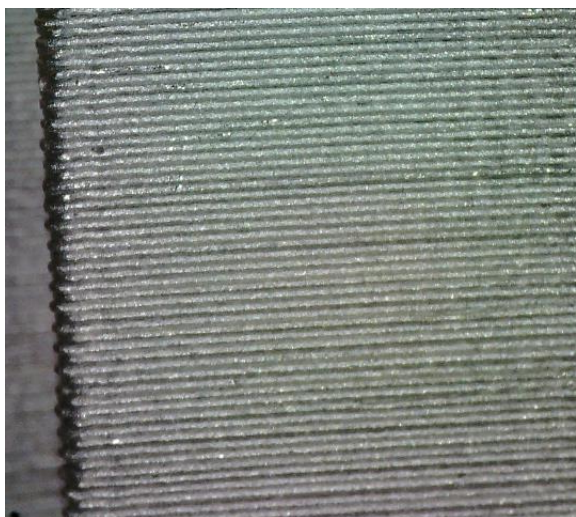


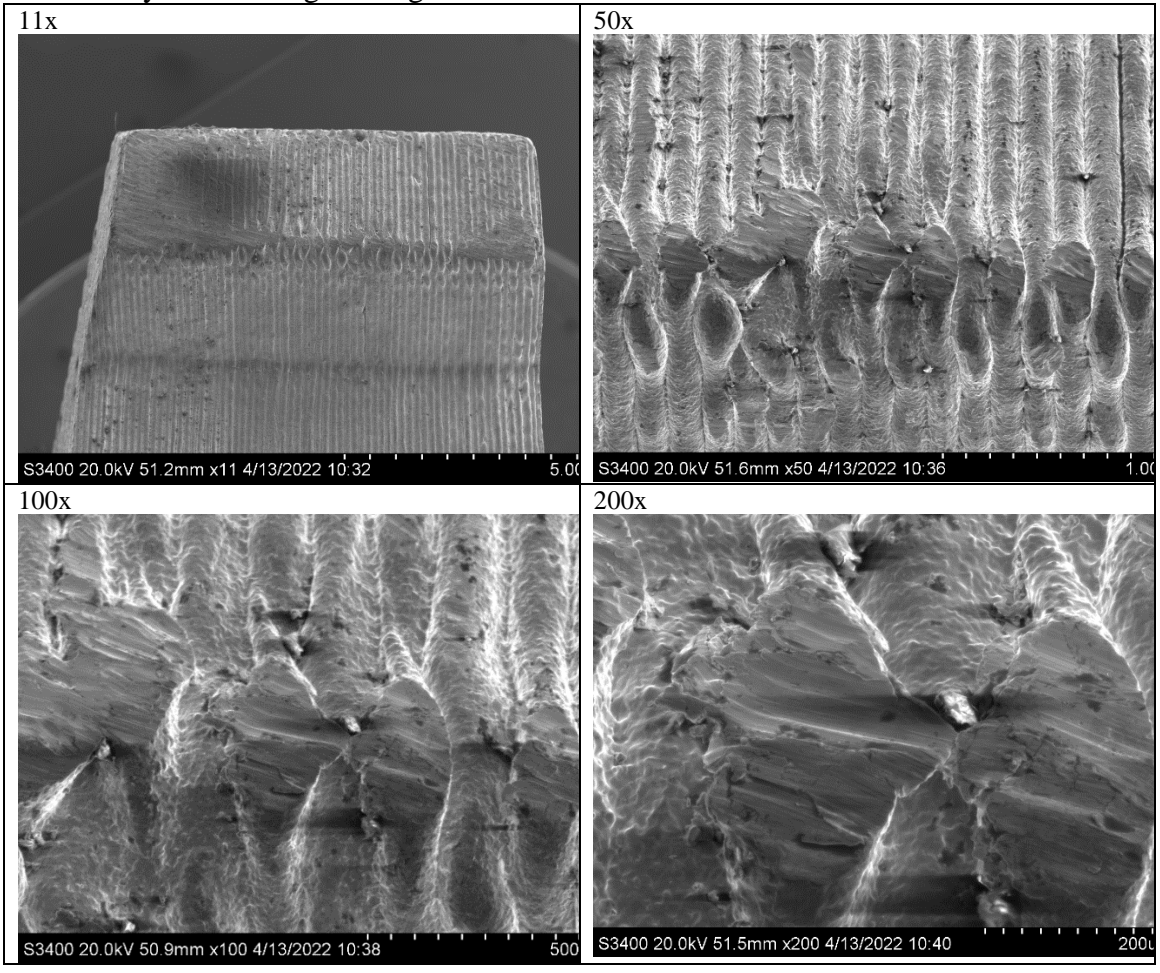
Figure 155W



Figure 158Z

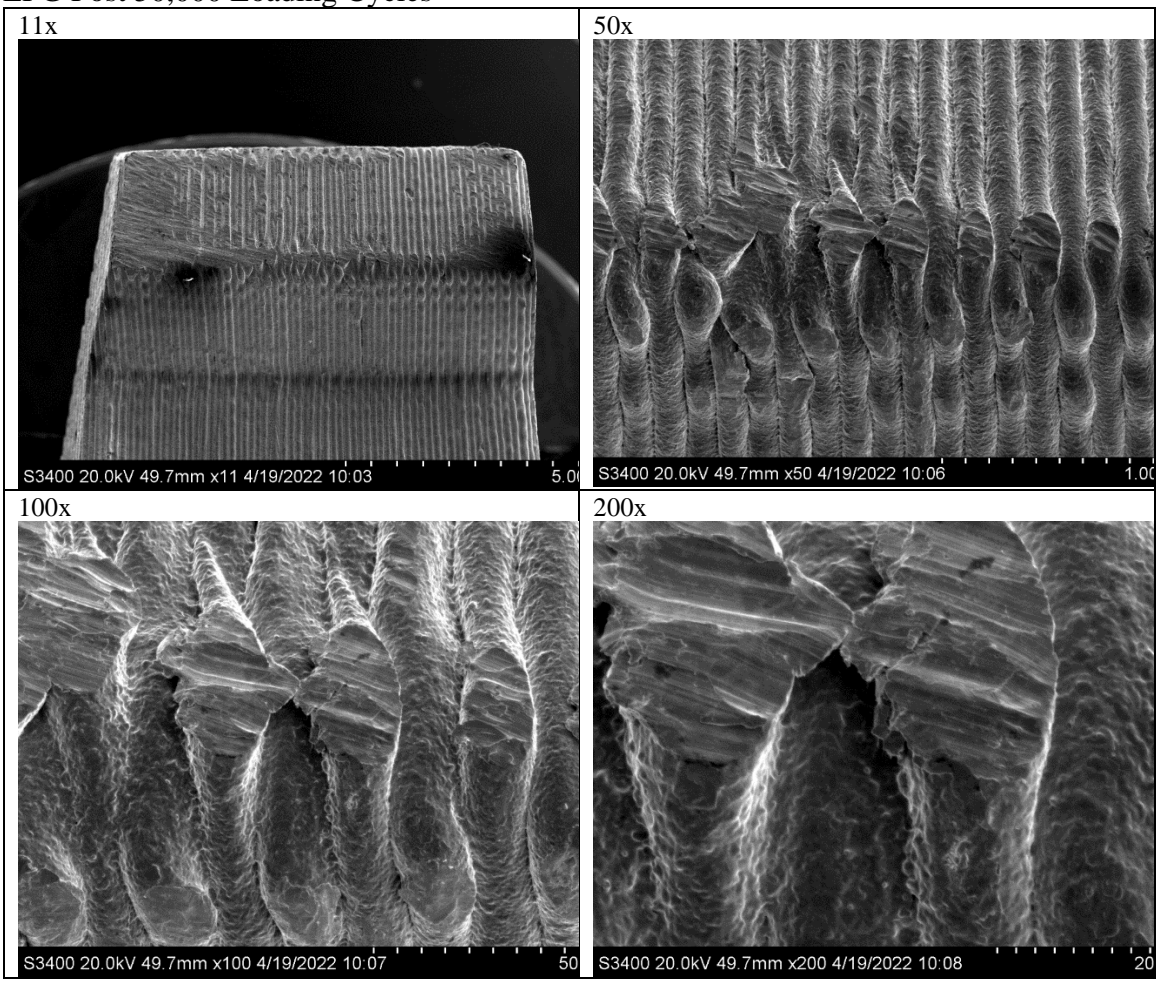
### APPENDIX E: SEM IMAGES OF STAINLESS-STEEL IMPLANT SURFACES

EFG Pre Cyclic Loading Testing

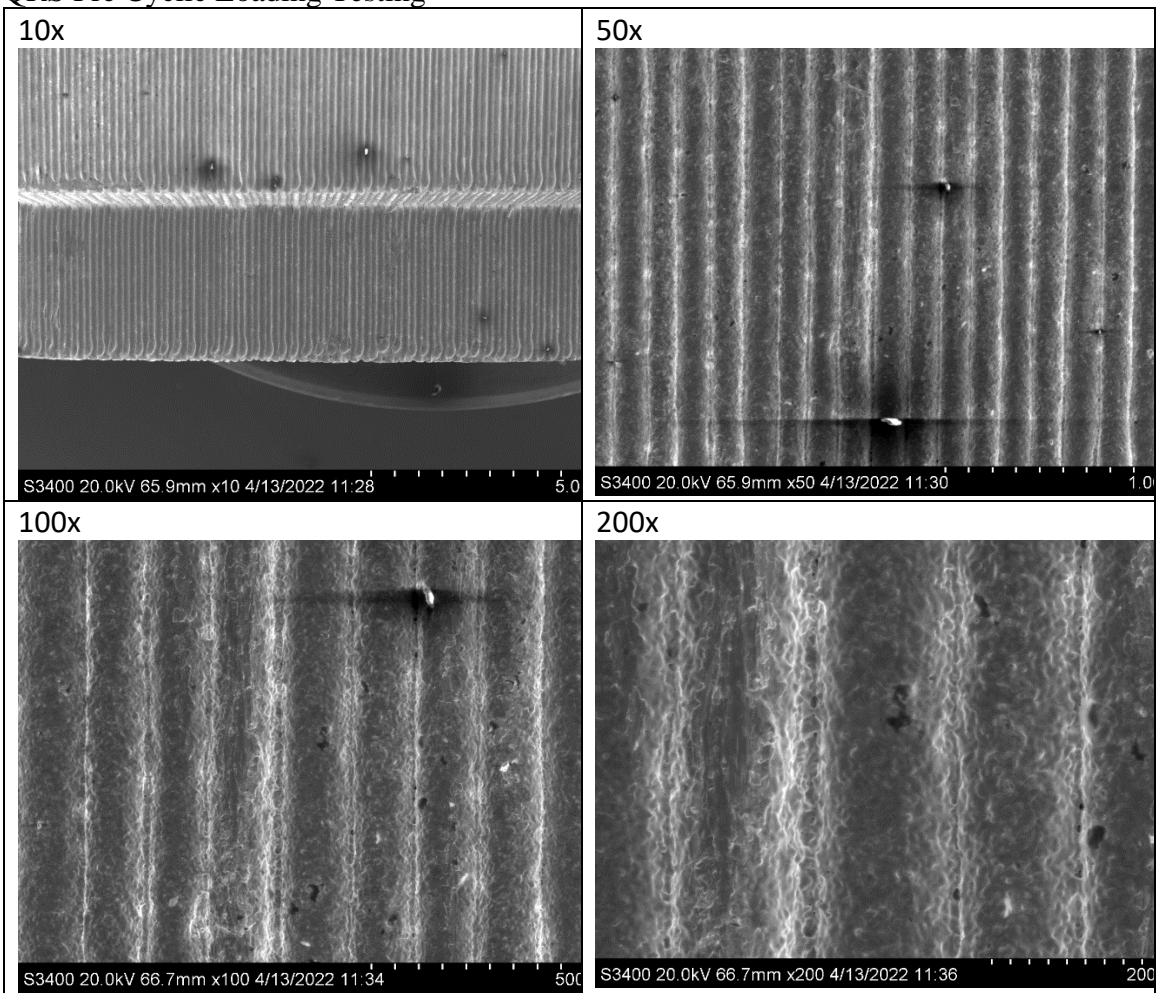




EFG Post 50,000 Loading Cycles

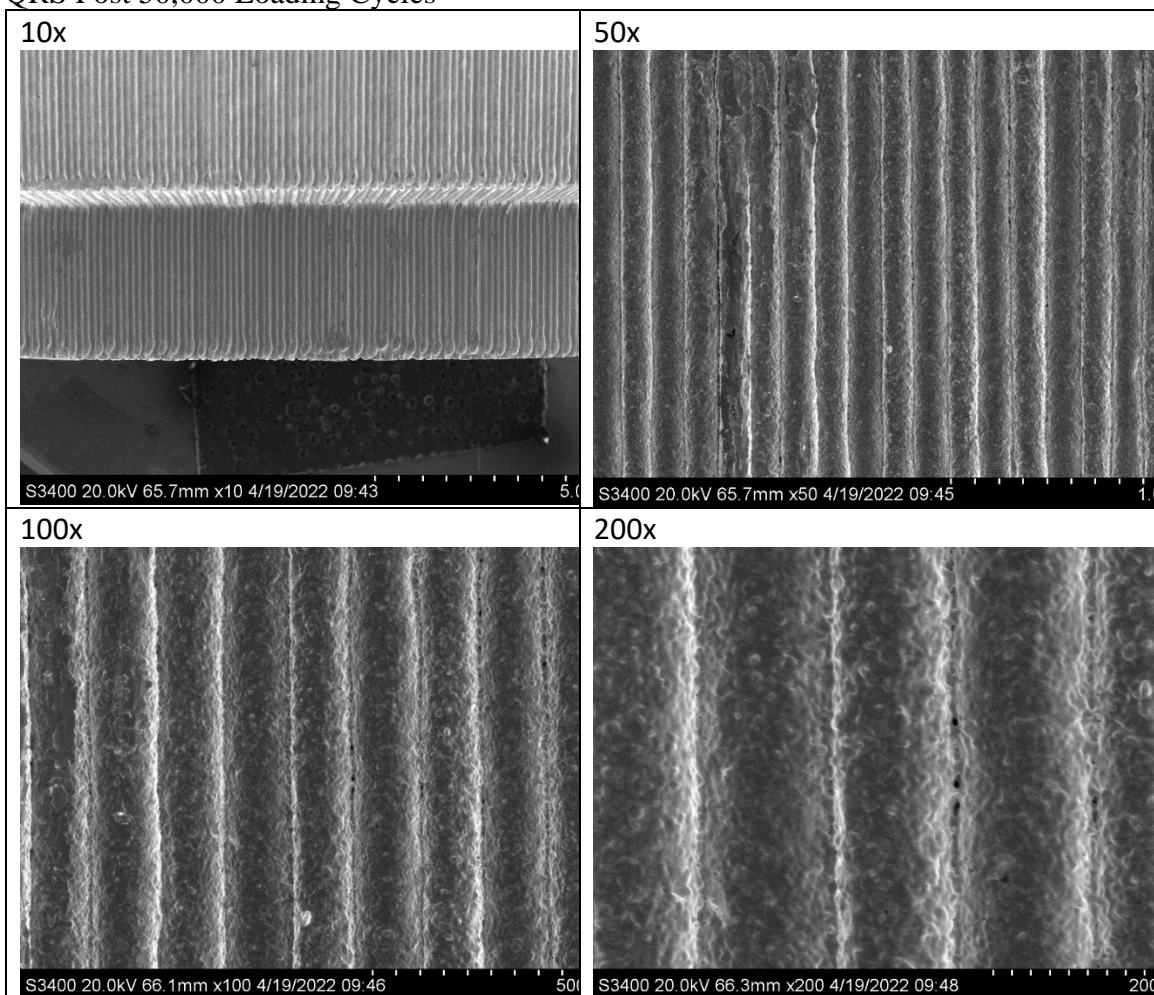


QRS Pre Cyclic Loading Testing

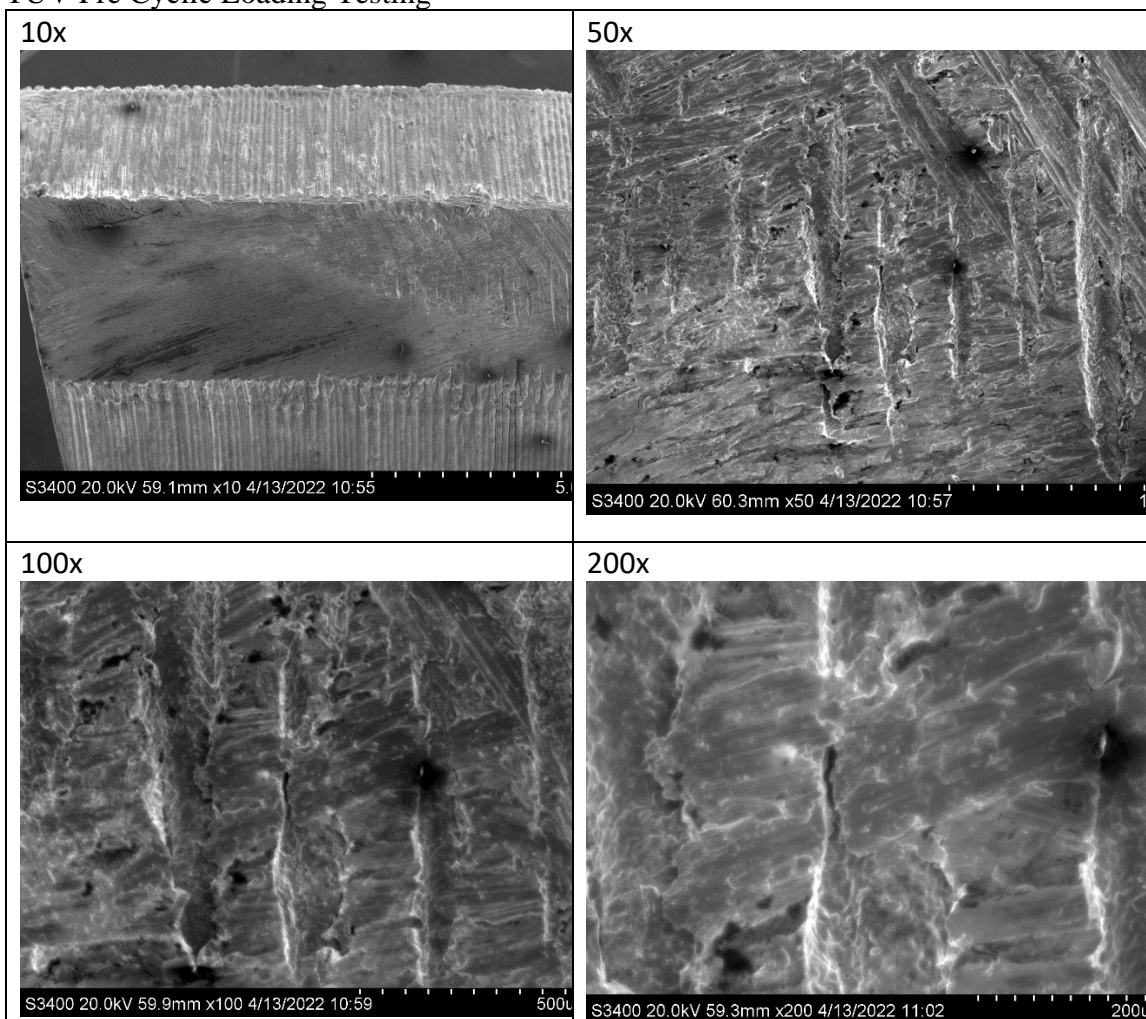




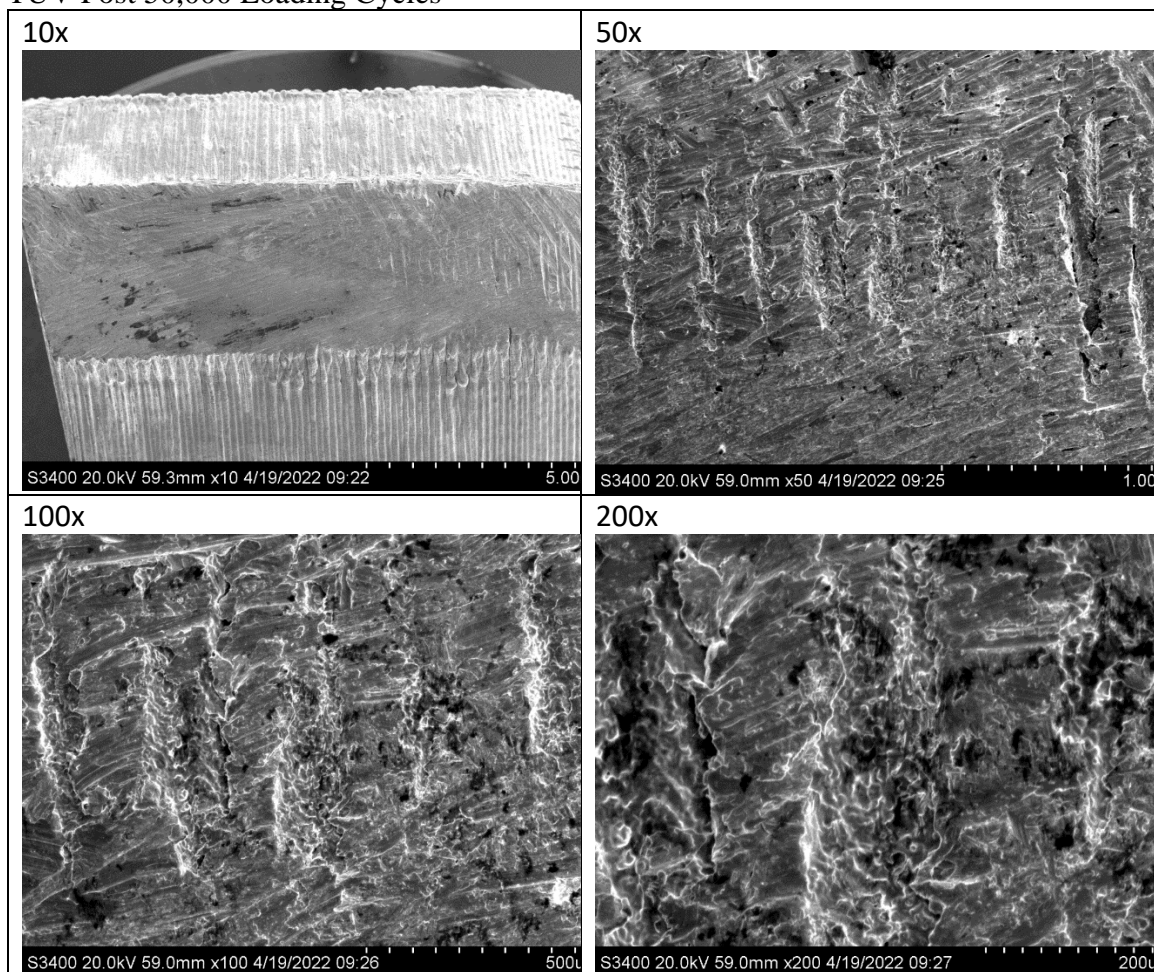
### QRS Post 50,000 Loading Cycles



### TUV Pre Cyclic Loading Testing



TUV Post 50,000 Loading Cycles



**APPENDIX F: RAW DATA FROM IMPLANT COMPONENT WEIGHTS AND WELL SAMPLE WEIGHTS IN GRAMS**

	pre testing 1	pre testing 2	pre testing 2	post 50,00	post 50,00	post 50,00
medial	77.7553	77.7548	77.7553	77.7502	77.7502	77.7502
lateral	25.80146	25.80177	25.80154	25.80076	25.80065	25.80064
anterior	22.60573	22.60585	22.60578	22.60528	22.60528	22.60527
posterior	22.23556	22.23577	22.23595	22.23442	22.23441	22.2343

Well Number	50 ul Sample After 10,000 Load			50 ul Sample After 50,000 Load		
	weight 1	weight 2	weight 3	weight 1	weight 2	weight 3
1						
2				0.04715	0.05591	0.04863
3				0.04894	0.04927	
4				0.04915	0.04952	0.04849
5				0.04866	0.0488	0.04817
6	0.04837	0.04872	0.0488	0.04894	0.04819	0.04978
7	0.0496	0.04897	0.04865	0.04909	0.04882	0.04886
8	0.0497			0.04855	0.04806	0.04894
9				0.04899	0.0478	0.04884
10				0.04917	0.04887	0.04872
11	0.0485	0.04785	0.04797	0.04883	0.0489	0.0485
12				0.0471	0.0511	0.04805
13				0.04878	0.049	0.0488
14				0.04877	0.05021	0.05016
15				0.0493	0.0547	0.04895
16				0.04859	0.0488	0.04898
17				0.04929	0.04929	0.05016
18	0.0483			0.0493	0.04909	0.04905
19				0.04891	0.04867	0.04792
20	0.04838	0.04882	0.0486	0.04891	0.04867	0.04873
21				0.04801	0.04925	0.0491
22						
23	0.04851	0.05116	0.04898	0.0492	0.04905	0.04901
24	0.05115	0.05149	0.05045	0.04878	0.04995	0.04895
25	0.04872	0.04861	0.04854	0.04897	0.05062	0.04879
26						
27				0.0489	0.04926	0.04905
28				0.05399	0.04935	0.05077
29				0.05227	0.04934	0.05312
30	0.04876	0.04879	0.04894	0.04868	0.04881	0.04881
31	0.04759	0.04831		0.05229	0.04945	0.0485
32				0.05324	0.04886	0.04934
33				0.04885	0.04867	0.04868
34	0.04887	0.04842		0.04895	0.04882	0.04878
35	0.04905	0.04741	0.04848	0.04948	0.04823	0.04895
36				0.04975	0.0495	0.04861
di water	0.049	0.0484	0.04866	0.04835	0.0488	0.0488
basin	0.04883	0.04892	0.04917			

**APPENDIX G: COMPUTATIONAL MODEL CONVERGENCE TEST FOR  
MESH SIZE OF IMPLANT**

Seed Size (mm)	Number of elements	Number of nodes	Strain	Von Mises Stress (MPa)
1.5	7284	10084	0.515441801	1.88416
1	23698	29731	0.517160585	1.883
0.75	55010	65475	0.518052682	1.8909

**APPENDIX H: LINK TO ABAQUS MODEL**

Link to ABAQUS Model: <https://tulane.box.com/s/qn4j3bbnwto9912of8h4q4kjb26hkgml>

### LIST OF REFERENCES

- Obesity and Total Joint Arthroplasty. (2013). *The Journal of Arthroplasty*, 28(5), 714-721. <https://doi.org/10.1016/j.arth.2013.02.011>
- Aglietti, P., Rinonapoli, E., Stringa, G., & Taviani, A. (1983). Tibial osteotomy for the varus osteoarthritic knee. *Clin Orthop Relat Res*(176), 239-251.
- Anderson, J. M., Rodriguez, A., & Chang, D. T. (2008). Foreign body reaction to biomaterials. *Seminars in immunology*, 20(2), 86-100. <https://doi.org/10.1016/j.smim.2007.11.004>
- Blau, P. J. (2013). Asperities. In Q. J. Wang & Y.-W. Chung (Eds.), *Encyclopedia of Tribology* (pp. 118-120). Springer US. [https://doi.org/10.1007/978-0-387-92897-5\\_167](https://doi.org/10.1007/978-0-387-92897-5_167)
- Bliddal, H., Leeds, A. R., & Christensen, R. (2014). Osteoarthritis, obesity and weight loss: evidence, hypotheses and horizons – a scoping review. *Obesity Reviews*, 15(7), 578-586. <https://doi.org/10.1111/obr.12173>
- Boyce, L., Prasad, A., Barrett, M., Dawson-Bowling, S., Millington, S., Hanna, S. A., & Achan, P. (2019). The outcomes of total knee arthroplasty in morbidly obese patients: a systematic review of the literature. *Archives of Orthopaedic and Trauma Surgery*, 139(4), 553-560. <https://doi.org/10.1007/s00402-019-03127-5>
- Bradley, B. M., Griffiths, S. N., Stewart, K. J., Higgins, G. A., Hockings, M., & Isaac, D. L. (2014). The Effect of Obesity and Increasing Age on Operative Time and Length of Stay in Primary Hip and Knee Arthroplasty. *The Journal of Arthroplasty*, 29(10), 1906-1910. <https://doi.org/10.1016/j.arth.2014.06.002>
- Brinkman, J. M., Lobenhoffer, P., Agneskirchner, J. D., Staubli, A. E., Wymenga, A. B., & Van Heerwaarden, R. J. (2008). Osteotomies around the knee. *The Journal of Bone and Joint Surgery. British volume*, 90-B(12), 1548-1557. <https://doi.org/10.1302/0301-620x.90b12.21198>
- Chae, D. J., Shetty, G. M., Wang, K. H., Montalban Jr, A. S. C., Kim, J. I., & Wook Nha, K. (2011). Early complications of medial opening wedge high tibial osteotomy using autologous tricortical iliac bone graft and T-plate fixation. *The Knee*, 18(4), 278-284. <https://doi.org/10.1016/j.knee.2010.05.009>
- Deshmukh, R. G., Hayes, J. H., & Pinder, I. M. (2002). Does body weight influence outcome after total knee arthroplasty? A 1-year analysis. *The Journal of Arthroplasty*, 17(3), 315-319. <https://doi.org/10.1054/arth.2002.30776>



- Elson, D. W., Dawson, M., Wilson, C., Risebury, M., & Wilson, A. (2015). The UK Knee Osteotomy Registry (UKKOR). *Knee*, 22(1), 1-3.  
<https://doi.org/10.1016/j.knee.2014.10.004>
- Epstein, A. M., Read, J. L., & Hoefler, M. (1987). The relation of body weight to length of stay and charges for hospital services for patients undergoing elective surgery: a study of two procedures. *American Journal of Public Health*, 77(8), 993-997.  
<https://doi.org/10.2105/ajph.77.8.993>
- Ethier, C. R., & Simmons, C. A. (2007). *Introductory Biomechanics: From Cells to Organisms*. Cambridge University Press. <https://doi.org/DOI:10.1017/CBO9780511809217>
- Felson, D. T. (1988). EPIDEMIOLOGY OF HIP AND KNEE OSTEOARTHRITIS. *Epidemiologic Reviews*, 10(1), 1-28.  
<https://doi.org/10.1093/oxfordjournals.epirev.a036019>
- Flandry, F., & Hommel, G. (2011). Normal Anatomy and Biomechanics of the Knee. *Sports Medicine and Arthroscopy Review*, 19(2), 82-92.  
<https://doi.org/10.1097/JSA.0b013e318210c0aa>
- Jeon, Y. S., Ahn, C. H., & Kim, M.-K. (2017). Comparison of HTO with articular cartilage surgery and UKA in unicompartmental OA. *Journal of Orthopaedic Surgery*, 25(1), 230949901668409. <https://doi.org/10.1177/2309499016684092>
- Jones, G. G., Clarke, S., Jaere, M., & Cobb, J. P. (2019). Failed high tibial osteotomy: A joint preserving alternative to total knee arthroplasty. *Orthopaedics & Traumatology: Surgery & Research*, 105(1), 85-88.  
<https://doi.org/https://doi.org/10.1016/j.otsr.2018.11.004>
- King, L. K., March, L., & Anandacoomarasamy, A. (2013). Obesity & osteoarthritis. *The Indian journal of medical research*, 138(2), 185-193.  
<https://pubmed.ncbi.nlm.nih.gov/24056594>  
<https://www.ncbi.nlm.nih.gov/pmc/articles/PMC3788203/>
- King, L. K., March, L., & Anandacoomarasamy, A. (2013). Obesity & osteoarthritis. *The Indian journal of medical research*, 138(2), 185-193.  
<https://pubmed.ncbi.nlm.nih.gov/24056594>  
<https://www.ncbi.nlm.nih.gov/pmc/articles/PMC3788203/>
- Kopeliovich, D. (2017, July 28). *Materials engineering*. main\_page [SubsTech]. Retrieved May 2, 2022, from <http://www.substech.com/>
- Kremers, H. M., Visscher, S. L., Kremers, W. K., Naessens, J. M., & Lewallen, D. G. (2014). The Effect of Obesity on Direct Medical Costs in Total Knee Arthroplasty. *JBJS*, 96(9).

[https://journals.lww.com/jbjsjournal/Fulltext/2014/05070/The\\_Effect\\_of\\_Obesity\\_on\\_Direct\\_Medical\\_Costs\\_in.3.aspx](https://journals.lww.com/jbjsjournal/Fulltext/2014/05070/The_Effect_of_Obesity_on_Direct_Medical_Costs_in.3.aspx)

- Lawrence, R. C., Felson, D. T., Helmick, C. G., Arnold, L. M., Choi, H., Deyo, R. A., Gabriel, S., Hirsch, R., Hochberg, M. C., Hunder, G. G., Jordan, J. M., Katz, J. N., Kremers, H. M., & Wolfe, F. (2008). Estimates of the prevalence of arthritis and other rheumatic conditions in the United States: Part II. *Arthritis & Rheumatism*, 58(1), 26-35. <https://doi.org/10.1002/art.23176>
- Liu, X., Chen, Z., Gao, Y., Zhang, J., & Jin, Z. (2019). High Tibial Osteotomy: Review of Techniques and Biomechanics. *Journal of healthcare engineering*, 2019, 8363128-8363128. <https://doi.org/10.1155/2019/8363128>
- Luo, C.-A., Hua, S.-Y., Lin, S.-C., Chen, C.-M., & Tseng, C.-S. (2013). Stress and stability comparison between different systems for high tibial osteotomies. *BMC Musculoskeletal Disorders*, 14(1), 110. <https://doi.org/10.1186/1471-2474-14-110>
- McElroy, M. J., Pivec, R., Issa, K., Harwin, S. F., & Mont, M. A. (2013). The Effects of Obesity and Morbid Obesity on Outcomes in TKA. *J Knee Surg*, 26(02), 083-088.
- Michael, J. W. P., Schlüter-Brust, K. U., & Eysel, P. (2010). The Epidemiology, Etiology, Diagnosis, and Treatment of Osteoarthritis of the Knee. *Deutsches Ärzteblatt international*. <https://doi.org/10.3238/arztebl.2010.0152>
- Miettinen, J. A., Salonen, R. J., Ylitalo, K., Niemelä, M., Kervinen, K., Säily, M., Koistinen, P., Savolainen, E.-R., Mäkikallio, T. H., Huikuri, H. V., & Lehenkari, P. (2012). The effect of bone marrow microenvironment on the functional properties of the therapeutic bone marrow-derived cells in patients with acute myocardial infarction. *Journal of translational medicine*, 10, 66-66. <https://doi.org/10.1186/1479-5876-10-66>
- Milošev, I., Levašič, V., Vidmar, J., Kovač, S., & Trebše, R. (2017). pH and metal concentration of synovial fluid of osteoarthritic joints and joints with metal replacements. *J Biomed Mater Res B Appl Biomater*, 105(8), 2507-2515. <https://doi.org/10.1002/jbm.b.33793>
- Moreland, J. R., Bassett, L. W., & Hunker, G. J. (1987). Radiographic analysis of the axial alignment of the lower extremity. *JBJS*, 69(5). [https://journals.lww.com/jbjsjournal/Fulltext/1987/69050/Radiographic\\_analysis\\_of\\_the\\_axial\\_alignment\\_of.16.aspx](https://journals.lww.com/jbjsjournal/Fulltext/1987/69050/Radiographic_analysis_of_the_axial_alignment_of.16.aspx)
- Nishimura, K., Tanabe, T., Kimura, M., Harasawa, A., Karita, K., & Matsushita, T. (2005). Measurement of articular cartilage volumes in the normal knee by magnetic resonance imaging: can cartilage volumes be estimated from physical characteristics? *Journal of Orthopaedic Science*, 10(3), 246-252. <https://doi.org/https://doi.org/10.1007/s00776-005-0889-5>

- Oliveira, C. A., Candelária, I. S., Oliveira, P. B., Figueiredo, A., & Caseiro-Alves, F. (2014). Metallosis: A diagnosis not only in patients with metal-on-metal prostheses. *European journal of radiology open*, 2, 3-6. <https://doi.org/10.1016/j.ejro.2014.11.001>
- Osti, M., Gohm, A., Schlick, B., & Benedetto, K. P. (2015). Complication rate following high tibial open-wedge osteotomy with spacer plates for incipient osteoarthritis of the knee with varus malalignment. *Knee Surg Sports Traumatol Arthrosc*, 23(7), 1943-1948. <https://doi.org/10.1007/s00167-013-2757-8>
- Pabinger, C., Berghold, A., Boehler, N., & Labek, G. (2013). Revision rates after knee replacement. Cumulative results from worldwide clinical studies versus joint registers. *Osteoarthritis and Cartilage*, 21(2), 263-268. <https://doi.org/10.1016/j.joca.2012.11.014>
- Reeuwijk, K. G., De Rooij, M., Van Dijk, G. M., Veenhof, C., Steultjens, M. P., & Dekker, J. (2010). Osteoarthritis of the hip or knee: which coexisting disorders are disabling? *Clinical Rheumatology*, 29(7), 739-747. <https://doi.org/10.1007/s10067-010-1392-8>
- Resnic, F. S., & Normand, S.-L. T. (2012). Postmarketing Surveillance of Medical Devices — Filling in the Gaps. *New England Journal of Medicine*, 366(10), 875-877. <https://doi.org/10.1056/nejmp1114865>
- Riddle, D. L., Singh, J. A., Harmsen, W. S., Schleck, C. D., & Lewallen, D. G. (2013). Clinically Important Body Weight Gain Following Knee Arthroplasty: A Five-Year Comparative Cohort Study. *Arthritis Care & Research*, 65(5), 669-677. <https://doi.org/10.1002/acr.21880>
- Ritter, M. A., Davis, K. E., Meding, J. B., Pierson, J. L., Berend, M. E., & Malinzak, R. A. (2011). The Effect of Alignment and BMI on Failure of Total Knee Replacement. *JBJS*, 93(17). [https://journals.lww.com/jbjsjournal/Fulltext/2011/09070/The\\_Effect\\_of\\_Alignm ent\\_and\\_BMI\\_on\\_Failure\\_of.4.aspx](https://journals.lww.com/jbjsjournal/Fulltext/2011/09070/The_Effect_of_Alignm ent_and_BMI_on_Failure_of.4.aspx)
- Roche, M., Law, T., Rosas, S., Rush, A., & Kurowicki, J. (2018). Effect of Obesity on Total Knee Arthroplasty Costs and Revision Rate. *The Journal of Knee Surgery*, 31(01), 038-042. <https://doi.org/10.1055/s-0037-1608933>
- Santoso, M. B., & Wu, L. (2017). Unicompartmental knee arthroplasty, is it superior to high tibial osteotomy in treating unicompartmental osteoarthritis? A meta-analysis and systemic review. *Journal of Orthopaedic Surgery and Research*, 12(1). <https://doi.org/10.1186/s13018-017-0552-9>
- Santoso, M. B., & Wu, L. (2017). Unicompartmental knee arthroplasty, is it superior to high tibial osteotomy in treating unicompartmental osteoarthritis? A meta-analysis and systemic review. *Journal of Orthopaedic Surgery and Research*, 12(1). <https://doi.org/10.1186/s13018-017-0552-9>

- Singh, J. A., Yu, S., Chen, L., & Cleveland, J. D. (2019). Rates of Total Joint Replacement in the United States: Future Projections to 2020–2040 Using the National Inpatient Sample. *The Journal of Rheumatology*, *46*(9), 1134-1140. <https://doi.org/10.3899/jrheum.170990>
- Sophia Fox, A. J., Bedi, A., & Rodeo, S. A. (2009). The Basic Science of Articular Cartilage: Structure, Composition, and Function. *Sports Health: A Multidisciplinary Approach*, *1*(6), 461-468. <https://doi.org/10.1177/1941738109350438>
- Spitaels, D., Mamouris, P., Vaes, B., Smeets, M., Luyten, F., Hermens, R., & Vankrunkelsven, P. (2020). Epidemiology of knee osteoarthritis in general practice: a registry-based study. *BMJ Open*, *10*(1), e031734. <https://doi.org/10.1136/bmjopen-2019-031734>
- Stoffel, K., Stachowiak, G., & Kuster, M. (2004). Open wedge high tibial osteotomy: biomechanical investigation of the modified Arthrex Osteotomy Plate (Puddu Plate) and the TomoFix Plate. *Clinical Biomechanics*, *19*(9), 944-950. <https://doi.org/https://doi.org/10.1016/j.clinbiomech.2004.06.007>
- Sun, H., Zhou, L., Li, F., & Duan, J. (2017). Comparison between Closing-Wedge and Opening-Wedge High Tibial Osteotomy in Patients with Medial Knee Osteoarthritis: A Systematic Review and Meta-analysis. *J Knee Surg*, *30*(02), 158-165.
- Swiatkowska, I., Martin, N., & Hart, A. J. (2019). Blood titanium level as a biomarker of orthopaedic implant wear. *J Trace Elem Med Biol*, *53*, 120-128. <https://doi.org/10.1016/j.jtemb.2019.02.013>
- Thienpont, E., & Parvizi, J. (2016). A New Classification for the Varus Knee. *The Journal of Arthroplasty*, *31*(10), 2156-2160. <https://doi.org/10.1016/j.arth.2016.03.034>
- Vermes, C., Roebuck, K. A., Chandrasekaran, R., Dobai, J. G., Jacobs, J. J., & Glant, T. T. (2000). Particulate Wear Debris Activates Protein Tyrosine Kinases and Nuclear Factor  $\kappa$ B, Which Down-Regulates Type I Collagen Synthesis in Human Osteoblasts. *Journal of Bone and Mineral Research*, *15*(9), 1756-1765. <https://doi.org/10.1359/jbmr.2000.15.9.1756>
- Ward, D. T., Metz, L. N., Horst, P. K., Kim, H. T., & Kuo, A. C. (2015). Complications of Morbid Obesity in Total Joint Arthroplasty: Risk Stratification Based on BMI. *The Journal of Arthroplasty*, *30*(9), 42-46. <https://doi.org/10.1016/j.arth.2015.03.045>
- Wendelboe, A. M., Hegmann, K. T., Biggs, J. J., Cox, C. M., Portmann, A. J., Gildea, J. H., Gren, L. H., & Lyon, J. L. (2003). Relationships between body mass indices and surgical replacements of knee and hip joints. *American Journal of Preventive Medicine*, *25*(4), 290-295. [https://doi.org/10.1016/s0749-3797\(03\)00218-6](https://doi.org/10.1016/s0749-3797(03)00218-6)

- Wier LM (Thomson Reuters), P. A. T. R., Maeda J (Thomson Reuters), Stranges E (Thomson , & Reuters), R. K. T. R., Jagadish P (AHRQ), Collins Sharp B (AHRQ), Elixhauser A (AHRQ). (2011). HCUP Facts and Figures: Statistics on Hospital-based Care in the United States, 2009. Rockville, MD: Agency for Healthcare Research and Quality. [http://www.hcup-us.ahrq.gov/reports/factsandfigures/2009/pdfs/FF\\_2009\\_section3.pdf](http://www.hcup-us.ahrq.gov/reports/factsandfigures/2009/pdfs/FF_2009_section3.pdf)
- Woo, S. L.-Y., & Buckwalter, J. A. (1988). Injury and repair of the musculoskeletal soft tissues. Savannah, Georgia, June 18-20, 1987. *Journal of Orthopaedic Research*, 6(6), 907-931. <https://doi.org/10.1002/jor.1100060615>
- Woodacre, T., Ricketts, M., Evans, J. T., Pavlou, G., Schranz, P., Hockings, M., & Toms, A. (2016). Complications associated with opening wedge high tibial osteotomy — A review of the literature and of 15years of experience. *The Knee*, 23(2), 276-282. <https://doi.org/https://doi.org/10.1016/j.knee.2015.09.018>
- Wright, J. M., Crockett, H. C., Slawski, D. P., Madsen, M. W., & Windsor, R. E. (2005). High Tibial Osteotomy. *JAAOS - Journal of the American Academy of Orthopaedic Surgeons*, 13(4), 279-289. [https://journals.lww.com/jaaos/Fulltext/2005/07000/High\\_Tibial\\_Osteotomy.7.aspx](https://journals.lww.com/jaaos/Fulltext/2005/07000/High_Tibial_Osteotomy.7.aspx)
- Yew, A., Jagatia, M., Ensaff, H., & Jin, Z. M. (2003). Analysis of contact mechanics in McKee-farrar metal-on-metal hip implants. *Proc Inst Mech Eng H*, 217(5), 333-340. <https://doi.org/10.1177/095441190321700501>
- Zhang, L., Haddouti, E.-M., Welle, K., Burger, C., Wirtz, D. C., Schildberg, F. A., & Kabir, K. (2020). The Effects of Biomaterial Implant Wear Debris on Osteoblasts. *Frontiers in cell and developmental biology*, 8, 352-352. <https://doi.org/10.3389/fcell.2020.00352>
- Zhang, Y., & Jordan, J. M. (2010). Epidemiology of Osteoarthritis. *Clinics in Geriatric Medicine*, 26(3), 355-369. <https://doi.org/10.1016/j.cger.2010.03.001>



## **BIOGRAPHY**

Madeline Tallman is from Wilmington, DE. She graduated from Tulane University with a Bachelor of Science in Engineering in Biomedical Engineering in December 2021. Madeline developed an interest in creating testing devices for orthopedic devices through her undergraduate research and was excited to apply those skills and knowledge to her master's thesis project. After graduating from Tulane with a Master of Science in Biomedical Engineering in May 2022, she will move to Flagstaff, Arizona to work for W.L. Gore & Associates as a quality engineer for medical devices.